UNIVERSITY OF WARMIA AND MAZURY IN OLSZTYN

Technical Sciences

19(4) 2016

PUBLISHER UWM

OLSZTYN 2016

The Technical Sciences is indexed and abstracted in BazTech (http://baztech.icm.edu.pl) and in IC Journal Master List (http://journals.indexcopernicus.com)

The Journal is available in electronic form on the web sites
http://www.uwm.edu.pl/techsci (subpage Issues)
http://wydawnictwo.uwm.edu.pl (subpage Czytelnia)

The electronic edition is the primary version of the Journal

PL ISSN 1505-4675
e-ISNN 2083-4527

Address
ul. Jana Heweliusza 14
10-718 Olsztyn-Kortowo, Poland
tel.: +48 89 523 36 61
fax: +48 89 523 34 38
e-mail: wydawca@uwm.edu.pl

Ark. wyd. 9,85, ark. druk. 8,0, nakład 85 egz.
Druk – Zakład Poligraficzny UWM w Olsztynie
zam. nr 64

Contents

Technical Sciences, 2016, 19(4), 295–312

Quarterly peer-reviewed scientific journal
ISSN 1505-4675
e-ISSN 2083-4527
TECHNICAL SCIENCES
Homepage: www.uwm.edu.pl/techsci/

THE EFFECT OF DRYING AND LONG-TERM STORAGE ON COLOUR AND CAROTENOIDS CONTENT OF GIANT PUMPKIN (CUCURBITA MAXIMA)

Mariusz Sojak, Małgorzata Jaros, Monika Janaszek-Mańkowska, Jędrzej Trajer, Szymon Głowacki, Arkadiusz Ratajski

Department of Fundamental Engineering
Warsaw University of Life Sciences

Received 30 August 2016, accepted 26 October 2016, available online 26 October 2016.

Key words: Chemical composition, Clustering, Colour, Drying, Factor analysis, Pumpkin.

Abstract

The objective of this study was to characterise the quality of giant pumpkin dried in different conditions as well as to determine the best combination(s) of drying conditions, based on colour and chemical composition of dried material. Samples of three pumpkin cultivars (Amazonka, Justynka-957 and Ambar) were dried at five different temperatures (40°C, 50°C, 60°C, 70°C, 80°C) using three different drying methods (forced convection in tunnel dryer, natural convection in chamber dryer and hybrid drying which combined a tunnel drying and fluidized-bed drying). It has been shown that variability of samples resulted primarily from the redness, yellowness, lutein and β-carotene. Samples were scored based on the range of responses identified by factor analysis in order to find an optimal combination of cultivar, temperature and drying method. The three subsequent highest scores were obtained for samples of Ambar cultivar, dried using hybrid drying at 40, 60 and 80°C respectively.

Symbols:

L – colour lightness [–]
a – colour redness [–]
b – colour yellowness [–]
DM – dry matter [$g \cdot g^{-1}$]
TS – total sugars [$g \cdot g^{-1}$]
RS – reducing sugars [$g \cdot g^{-1}$]
LU – lutein [$mg \cdot g^{-1}$]

Correspondence: Mariusz Sojak, Katedra Podstaw Inżynierii, Szkoła Główna Gospodarstwa Wiejskiego, ul. Nowoursynowska 164, 02-787 Warszawa, phone: 22 59 346 16, e-mail: mariusz_sojak@sggw.pl

LY – lycopene [mg · g^{-1}]
BC – β-carotene [mg · g^{-1}]
B – pumpkin cultivar Ambar
Z – pumpkin cultivar Amazonka
J – pumpkin cultivar Justynka
F – forced convection in a tunnel dryer
N – natural convection in a chamber dryer
H – hybrid drying
C×D – interaction of cultivar and drying method
T – drying temperature [°C]
C – cultivar
D – drying method
RSQ – R-squared index [–]

Introduction

Consumption of pumpkin has increased all over the world in the last few years. Research proved that pumpkin has health benefits and can significantly contribute to the uptake of pro-vitamin A, especially lutein which is responsible for specific physiological functions (MURKOVIC et al. 2002, GUINÉ et al. 2011). Studies conducted by MURILLO et al. (2010) revealed that pumpkin possesses higher concentration of lutein compared to cabbage, carrot (twenty-fold higher), potato or tomato – the vegetables vastly recommended as the richest sources of lutein. Research report that pumpkin-rich diet has pharmacological activity and could reduce blood glucose (XIONG, CAO 2001, ZHANG et al. 2002, ZHANG, YAO 2002, CAI et al. 2003). The protein-bound polysaccharides in pumpkin have potential use as an anti-diabetic agent, because of ability to improve tolerance of glucose by reducing the blood glucose levels and increasing the levels of serum tolerance of glucose (ADAMS et al. 2011, CARVALHO DE et al. 2012). Pumpkin polysaccharides display therapeutic potential, which may be useful in prevention and treatment of diabetic complications, such as decreased myocardial compliance (ARONSON 2003), arteriosclerosis (THOMAS et al. 2005), peripheral neuropathy (WADA, YAGIHASHI 2005), cataracts (ROBINSON et al. 1983), retinopathy (ROBINSON et al. 1989), neuropathy (YOUNG et al. 1983) and kidney lesion (BURG 1995, WANG et al. 2012). Pumpkin is also a rich source of fibre and β-carotene – an immediate precursor of vitamin A. Fibre addition to foods is an alternative to compensate for the existent deficiency in the diet. Nowadays, the recommended dietary fibre intake is 25–30 grams a day. Total fibre content in pumpkin pulp is up to 0.784 ± 0.008 g · g^{-1}. Pumpkin contains also many water soluble components belonging to the cytoplasmic medium like globular proteins, mono-, di- and oligosaccharides, amino-acids, salts and organic acids (PLA et al. 2007). The fresh pumpkin contains 0.09÷0.1 mg · g^{-1} of vitamin C and 0.013–0.0106 mg · g^{-1} of vitamin E (TERAZOWA et al. 2001, MURKOVIC et al.

2002, KUNACHOWICZ et al. 2005). Pumpkin fruit is also a valuable source of other vitamins, like B6, K, thiamine and riboflavin as well as minerals, e.g., potassium, phosphorus, magnesium, iron and selenium (USDA 2004, NAWIRSKA et al. 2009, RAKCEJEVA et al. 2011).

As a seasonal crop fresh pumpkins are very sensitive to microbial spoilage even if stored at refrigerated conditions, thus they require processing, e.g. freezing or drying (GUINÉ et al. 2001, DOYMAZ 2007). Fresh, unprocessed pumpkin should be stored at temperature between 10 and 13°C and at relative air humidity between 50% and 70% (KITINOJA, KADER 2002). Approximate storage life is only 2÷3 months. When stored in low temperature, unfavourable physiological processes occur resulting in chill damage. For this reason drying seems to be the most reasonable method for pumpkin preservation. Dried pumpkin can be treated as final or semi-final product which may enrich basic foods in nutrients important for people (SOJAK, GŁOWACKI 2010). Convective drying is the most common method of food preservation for the reason of being the most efficient and the least expensive (PEREZ, SCHMALKO 2007). Therefore, using other drying technologies is not economically justified (except for scientific purposes). However, properly selected drying method may increase the quality of the final product (DIAMANTE, MUNRO 1993, ERTEKIN, YALDIZ 2004, LEWICKI 2006, SOJAK, GŁOWACKI 2010).

Heat processing of plant materials generally results in the loss of biologically active compounds (DIVYA et al. 2012). Also colour degradation or discolouration occur frequently as the effect of temperature or different drying treatments and is related mainly to pigment degradation, enzymatic or oxidative browning and Maillard reactions (DU 2009, WANG et al. 2011). As regards pumpkin CIE*Lab* colour parameters as well as chroma (C) and hue angle (h) are commonly used to monitor the quality of material dried in different conditions. Colour lightness (L) is reported as the most sensitive to changes of drying temperature, drying technique and drying pretreatments and also related to carbohydrates content (ALIBAS 2007, NAWIRSKA et al. 2009) and the occurrence of non-enzymatic browning reactions (GLIEMO et al. 2009). Chromaticity parameters a and h are regarded as temperature dependent and darkening indicators (FALADE, SHOGAOLU 2010). NAWIRSKA et al. (2009) reported that parameters a, b and L should gain high values to obtain the best colour of dried pumpkin slices. It was proved that pumpkin exposure to heat and oxygen leads to α- and β-carotene degradation followed by increase of *cis* isomers resulting in loss of yellowness (less observed as fading) (FALADE, SHOGAOLU 2010, LAGO-VANZELA et al. 2013). Nonetheless, colour changes resulting from dehydration are also cultivar dependent (KONOPACKA et al. 2010).

In this study convective drying of pumpkin was realised at different temperatures in a chamber dryer, tunnel dryer and fluidized bed dryer.

The objective of this study was to characterise the quality of giant pumpkin dried in different conditions as well as to determine the best combination(s) of cultivar and drying conditions, based on colour and chemical composition of dried material.

Materials and methods

Sample preparation and drying experiments

Sample material was taken from parenchyma of three giant pumpkin (*Cucurbita maxima* Duch.) cultivars: Amazonka (Z), Justynka-957 (J) and Ambar (B). Pumpkins were grown on the experimental field owned by the Department of Genetics, Breeding and Biotechnology at the Faculty of Horticulture, Biotechnology and Landscape Architecture, Warsaw University of Life Sciences-SGGW. Each cultivar was represented by ten (10) plants taken randomly from the experimental field. Parenchyma samples taken from the top (sunny) part of the fruit were washed, peeled, purified from seeds and cut into 10 mm cubes using industrial slicer. The samples for further studies were prepared according to the method described by MURKOVIC et al. (2002).

Samples were dried at five different temperatures (40°C, 50°C, 60°C, 70°C and 80°C) using three different drying methods (forced convection in a tunnel dryer (F), natural convection in a chamber dryer (N) and hybrid method (H), which consisted of (F) in the first phase and fluidized-bed drying in the second phase). Dried material was stored approximately five years under uncontrolled conditions in airtight dark containers, at mean temperature of 21.5±3.5°C and mean relative humidity of 50%±10% (ZANONI et al. 2007, DIVYA et al. 2012).

Sample characteristics

After five years of storage 37 of 45 samples were suitable for further analysis. Dried material was pulverised and analysed for dry matter content – DM (PN-R-04013: 1988), total sugars – TS and reducing sugars – RS according to the Luff-Schoorl method (FORTUNA et al. 2003), lutein – LU, lycopene – LY and β-carotene – BC using HPLC method. Colour of each sample was extracted from digital images and expressed as CIE*Lab* colour space coordinates. Pulverised samples were placed in dishes made from light scattering material. Colour images of samples were acquired using Canon flatbed scanner, model CanoScan 5600F. The device was equipped with 6-line colour CCD sensor, fluorescent lamp and the 48-bit input/output interface (16 bits for each RGB channel). Images of resolution of 300 dpi were acquired to sRGB

colour space. During scanning process all tools for automatic image enhancement had been disabled.

Mean brightness of Red, Green and Blue channel were extracted from each sample image and then linearly transformed to CIE*XYZ* colour space relative to D65 reference white. Nonlinear transformation of CIE*XYZ* to CIE*Lab* coordinates was done relative to illuminant D65 and observer 10°, according to CIE standard using 94.81, 100, 107.32 values as reference whites for X, Y and Z coordinates respectively (CIE 2004). Pumpkin colour was then characterised by three parameters: L – lightness (100 for white and 0 for black), a – colour redness or greenness ($-a$: green, $+a$: red), b – colour blueness or yellowness ($-b$: blue, $+b$: yellow).

Data analysis

Unbalanced ANOVA for three-way factorial design with incomplete evaluation of interactions in terms of temperature was realised to characterise variability of samples (Tab. 1). Multiple comparison procedure was realised using Tukey-Kramer test. The main effects of cultivar, drying method and temperature were studied. Since there was no replications for drying temperatures only interaction of cultivar and drying method (C×D) was considered.

Table 1

Unbalanced three-way factorial design

40°C	50°C	60°C	70°C	80°C
BH		BH		BH
BN		BN		BN
BF	BF	BF	BF	BF
JH	JH	JH	JH	
JN	JN		JN	JN
JF	JF	JF	JF	JF
ZH	ZH	ZH	ZH	ZH
ZN	ZN	ZN	ZN	ZN
	ZF		ZF	ZF

Exploratory factor analysis (EFA) with varimax orthogonal rotation was applied to determine features that most explained variability of samples. On this basis features with the highest discriminant ability were selected as responses to 37 combinations of pumpkin cultivar (C), drying temperature (T) and drying method (D). Number of valid factors was determined upon Keiser criterion (eigenvalue criterion).

To investigate similarities of dried material as well as to rank the drying treatments cluster analyses were applied using Ward's minimum-variance procedure. An optimal number of clusters was determined on the basis of R^2 (RSQ) index (SARLE 1983).

Based on the full set of variables samples were divided into optimal number of clusters. Then, one-way ANOVA and Tukey-Kramer multiple comparison procedure were used to characterise each cluster on the optimal level of hierarchy.

Additionally, to obtain the best CTD combination(s), cluster analyses were performed using each response $r = (1, 2, ..., n)$ derived from EFA as a predictor. Based on the range of mean responses in each cluster, a normalised value s (score) between 0 and 1 was allocated to each cluster member. The higher rank represented more desirable response. Then, a scoring method was chosen to determine the best combination of CTD which maximised total score. For multiple responses, partial scores were combined into total score (S). Hence, the total score for each treatment was calculated according to NADIAN et al. (2016) using the following equation:

$$S = \left(\prod_{r=1}^{n} S_r\right)^{n^{-1}} \tag{1}$$

All analyses except cluster analyses were performed in STATISTICA 12 (StatSoft Inc., Tulsa, OK, USA). Cluster analyses were carried using SAS 9.4 (SAS Institute Inc., Cary, NC, USA).

Results and discussion

Three-way unbalanced ANOVA was performed to study the effects of cultivar and drying treatment on colour and basic chemical composition of samples. Tables 2, 3, 4 and 5 present means, standard deviations and homogeneous groups only for significant effects.

The effect of temperature

The effect of temperature was negligible for most characteristics except for reducing sugars and colour lightness (Tab. 2). Significant differences in RS were observed only between samples dried at 40°C and 80°C whereas samples dried at other temperatures formed three superimposed homogeneous groups. Colour lightness decreased while temperature increased but only samples dried at 80°C were significantly darker compared to samples dried at lower temperatures. These results confirm the conclusions on the sensitivity of L parameter to drying temperature reported by ALIBAS (2007) as well as the connection of high lightness values and high carbohydrates content reported by NAWIRSKA et al. (2009). Darkening of samples dried at high temperatures is in agreement with other results reported for pumpkin (ROONGRUANGSRI,

BRONLUND 2016) and may occur as the effect of Maillard reaction, responsible for nonenzymatic browning (SEVERINI et al. 2005) as well as from high concentration of colorants (in this case carotenoids) which was suggested by LEWICKI and DUSZCZYK (1998) as the effect of water removal and its substitution by air as well as surface deformation (shrinkage) during convective drying.

Table 2

Three-way ANOVA results: the effect of temperature*

Variable	Statistic	T [°C]				
		40	50	60	70	80
RS	Mean	0.18^{a}	0.16^{ab}	0.15^{abc}	0.14^{bc}	0.13^{c}
	SD	0.02	0.02	0.02	0.02	0.03
L	Mean	71.47^{a}	70.21^{a}	70.49^{a}	68.19^{a}	63.23^{b}
	SD	4.29	4.66	3.12	3.43	5.22

Means with the same letter do not differ significantly at $\alpha = 0.01$.

The effect of cultivar

Studied cultivars differed significantly in dry matter and carotenoids content (Tab. 3). Cultivar Ambar characterised with the highest DM while no significant differences were observed for the other two cultivars. Ambar and Amazonka contained significantly more lutein than Justynka. Moreover, Ambar was the richest in lycopene and β-carotene and as regards these substances each cultivar differed significantly from the others. Lycopene content in dried Ambar samples was almost five times higher than in Justynka and nine times higher than in Amazonka samples. Pumpkin cultivar affected also colour lightness and yellowness. The darkest but the most yellow colour was characteristic for Amazonka samples which differed significantly from the lightest samples of Justynka and the least yellow samples of Ambar. One may observed some relationship between yellowness and lycopene content. Cultivars with high content of lycopene were less yellow but characterised with higher L which is rather obvious considering that lycopene is a red colorant. The differences in total carotenoids content between cultivars Ambar and Amazonka dehydrated by convective drying at 60°C (1.32 and 4.86 mg · g^{-1} respectively) are in agreement with results obtained by NAWIRSKA et al. (2009). Nonetheless, cultivar Ambar dried at 80°C characterised with total carotenoids content of 1.86 mg · g^{-1} which was over two times higher comparing to carotenoids content observed for Amazonka cultivar (0.76 mg · g^{-1}). Since the drying experiment was unbalanced, the significance of C×T interaction could not be tested but results obtained for 80°C may be explained (to some extent) by the cultivar ability to retain carotenoids in high drying temperatures. From the other hand, the difference in total carotenoids content observed between

Ambar samples dried at 60 and 80°C (even if not significant) may result from the ease of extraction of these substances which might be protected or combined with other products at lower temperatures and released (available) at higher temperatures. Similar conclusions were proposed by LAGO-VANZELA et al. (2013).

Table 3

Three-way ANOVA results: the effect of cultivar*

C	Statistic	DM	LU	LY	BC	*L*	*b*
B	mean	0.94^{a}	1.28^{a}	0.18^{a}	0.50^{a}	69.44^{a}	27.06^{b}
	SD	0.02	1.29	0.12	0.38	2.96	3.94
J	mean	0.92^{b}	0.57^{b}	0.05^{b}	0.22^{c}	71.57^{a}	34.15^{ab}
	SD	0.01	0.51	0.03	0.06	4.24	11.76
Z	mean	0.92^{b}	1.04^{a}	0.03^{b}	0.36^{b}	65.04^{b}	42.79^{a}
	SD	0.01	0.29	0.01	0.17	5.23	17.91

Means with the same letter do not differ significantly at $\alpha = 0.01$.

The effect of drying method

Significant effects of drying method were observed in case of lutein, β-carotene and colour lightness (Tab. 4). Samples subjected to hybrid drying were significantly more rich in carotenoids compared to samples undergone drying in a tunnel or chamber dryer. Moreover, samples subjected to natural convection contained least carotenoids and were significantly lighter than the others. This suggests that natural convection favoured the loss of carotenoids (in this case lutein and β-carotene) which involves also differences in colour. Similar dependency between colour lightness and drying method was reported by HENRIQUES et al. (2012). Hot-air drying is considered to be the most destructive drying method in terms of carotenoids retention and product discoloration since carotenoids rapidly lose their activity when heated in the presence of oxygen, especially at higher temperatures (LEŠKOVÁ et al. 2006,

Table 4

Three-way ANOVA results: the effect of drying method*

D	Statistic	LU	BC	*L*
F	mean	0.73^{b}	0.31^{b}	67.72^{b}
	SD	0.44	0.14	4.81
N	mean	0.56^{b}	0.28^{b}	71.24^{a}
	SD	0.57	0.14	4.40
H	mean	1.52^{a}	0.47^{a}	67.05^{b}
	SD	1.04	0.38	5.28

Means with the same letter do not differ significantly at $\alpha = 0.01$.

WANG et al. 2011). Research results reported by other authors indicates that the loss of carotenoids activity may be avoided by using hot-air drying in low temperatures (ROONGRUANGSRI, BRONLUND 2016), freeze-drying which eliminates high temperature and oxygen from drying process (NAWIRSKA et al. 2009, DIRIM, ÇALIŞKAN 2012) or starch coatings (LAGO-VANZELA et al. 2013) to protect carotenoids from oxidation during convective drying.

The effect of cultivar and drying method interaction

Significant C×D interaction effects were observed in case of dry matter, lutein, β-carotene and yellowness (Fig. 1). Regarding DM significance of C×D interaction occurred mainly due to variation of this parameter in samples obtained by hybrid method. The highest dry matter content was specific for samples dried using natural convection (Fig. 1*a*). *Ambar* samples characterised with the highest content of DM, while the lowest content of DM was specific for Amazonka samples. Slightly lower values of DM were characteristic for samples dried in a tunnel dryer. As regards the hybrid method DM content in Ambar samples dropped significantly while in case of Justynka the same parameter significantly increased.

The content of lutein (Fig. 1*b*) in Ambar and Amazonka samples was also significantly affected by C×D interaction. Lutein content in Ambar samples dried using chamber or tunnel dryer dropped significantly in comparison to samples obtained by hybrid method. In general each cultivar characterised

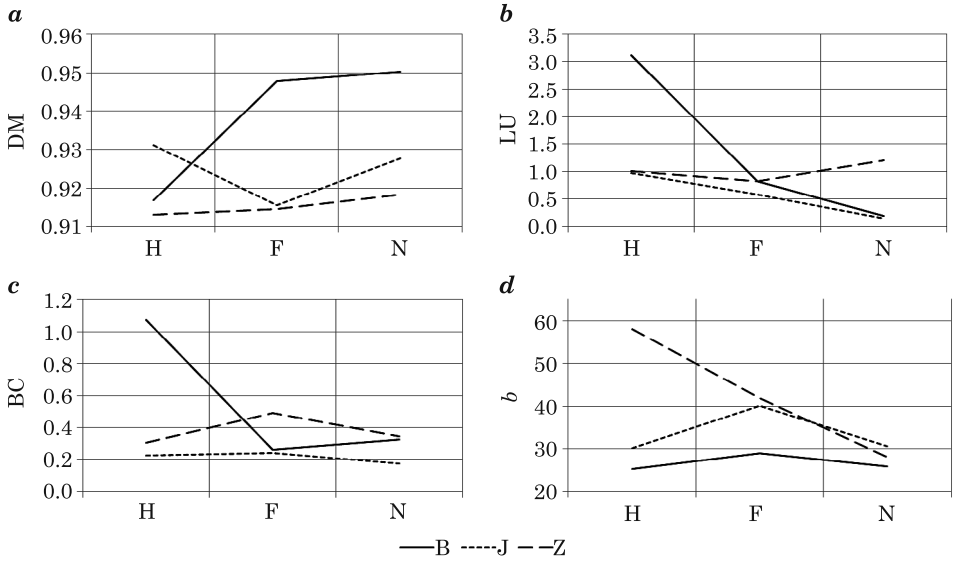

Fig. 1. The effect of C\D interaction on DM (*a*), LU (*b*), BC (*c*) and *b* (*d*)

with the highest, medium and the lowest content of lutein if dried using H, F and N drying method respectively. The exception from this rule was observed for Amazonka samples dried in a chamber dryer. In this case lutein content was higher compared to samples obtained by other drying methods. Concerning β-carotene significantly different reaction to drying method was observed in Ambar samples (Fig. 1*c*). Two other cultivars characterised with the highest content of BC if dried in a tunnel dryer and slightly (but not significantly) lower content of this substance if dried using other methods. In case of Ambar BC content was significantly higher (also compared to other cultivars) in samples obtained by hybrid method than in samples undergone drying in tunnel or chamber dryer.

Regarding yellowness of Justynka and Ambar, the highest values of this parameter were observed in samples dried in a tunnel dryer and slightly lower in case of samples dried using other methods (Fig. 1*d*). Generally, variation in yellowness of Justynka and Ambar samples was not affected by C×D interaction. Yellowness of Amazonka was no exception from this rule as regards samples dried in a tunnel or chamber dryer. However, dried material obtained by hybrid method characterised with significantly higher yellowness than the other samples.

Determination of the best discriminants of samples

Exploratory factor analysis resulted in four factors that met the Kaiser criterion (Fig. 2). First four factors explained variation of samples in almost 80%. Table 5 presents factor pattern for analysed data. The highest contribution to total between-sample variation was observed for the first (26.07%) and the second (22.46%) factor. Variables a and b had the largest loadings on the first factor (0.89 and – 0.95 respectively) whereas the second factor consisted of high positive loadings on BC and LU (0.93 and 0.86 respectively). Therefore factor 1 may be interpreted as a colour measure (redness and yellowness) while factor 2 primarily measures samples' content of carotenoids. Moreover, the first component is a contrast of redness against yellowness with the opposite signs of its factor loading, which means that more red sample is less yellow. Considering variance explained by extracted factors, variables b, a, BC and LU (in this specific order) are the most essential responses for combination of CTD which means that they are the best discriminants of samples. This result is in agreement with previously mentioned reports where carotenoid content is considered as an important parameter for the determination of the final quality of dehydrated pumpkin as it is a determining factor in both colour and nutritional quality of the product (DIRIM, ÇALIŞKAN 2012).

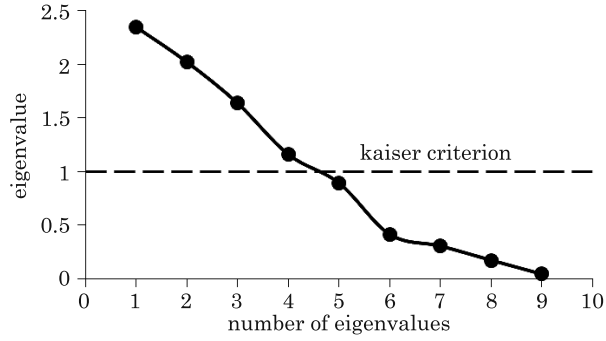

Fig. 2. Scree plot

Table 5

Factor pattern

Variable	Factor 1	Factor 2	Factor 3	Factor 4
DM	0.09	-0.24	-0.15	-0.89
TS	-0.03	0.18	0.60	-0.06
RS	-0.26	0.01	0.82	0.21
LU	0.13	**0.86**	0.01	0.12
LY	0.08	0.51	0.26	-0.70
BC	0.05	**0.93**	0.08	-0.06
L	0.39	-0.41	0.64	-0.24
a	**0.89**	0.15	-0.21	0.09
b	**-0.95**	-0.06	-0.06	0.26
Variance explained	1.94	2.14	1.59	1.49
% of total variance	26.07	22.46	18.19	12.89

Cluster analysis

Clustering procedure was applied to full set of variables to characterise samples' variation. RSQ value of 0.798 indicated three clusters as the optimal level of hierarchy (Fig. 3). Figure 4 displays tree diagram which indicates the

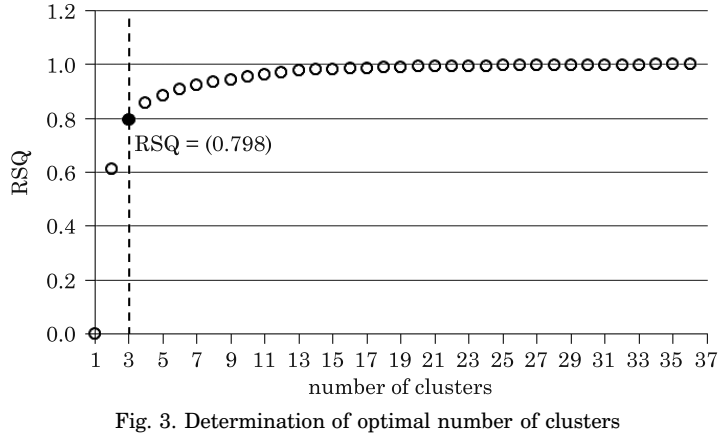

Fig. 3. Determination of optimal number of clusters

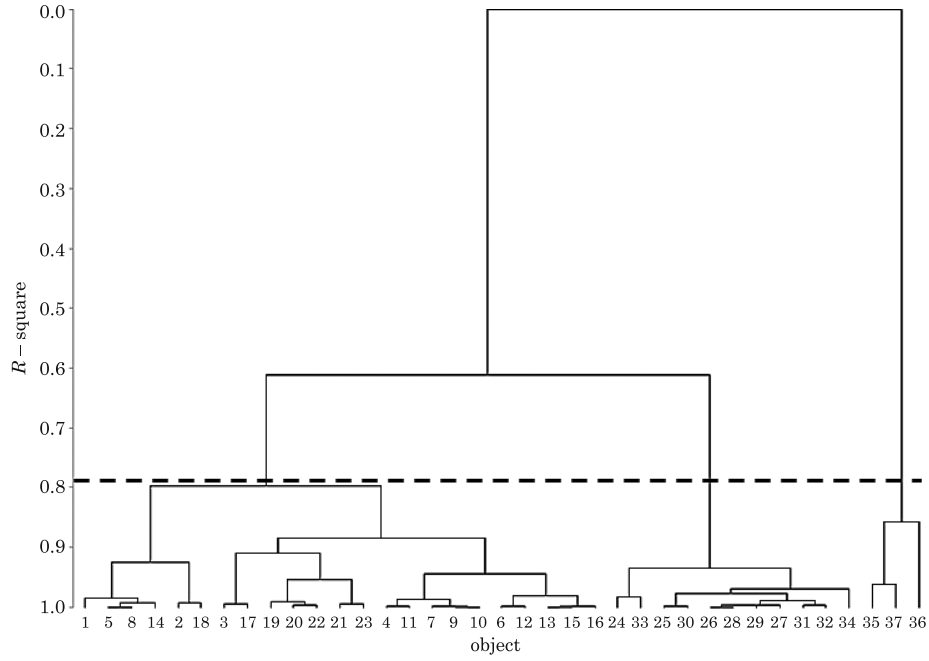

Fig. 4. Tree diagram obtained with respect to all characteristics of samples

cluster membership of each CTD combination in the cluster tree. The cluster name (object number rather than sample label) and RSQ are displayed on the horizontal and vertical axes, respectively. The lowest level of tree diagram consists of leaves being representation of CTD combinations. As the clustering algorithm proceeds leaves are clustered to form branches which are further joined to form root. The RSQ indicates similarity between leaves or branches, thus branches separated by the dashed line consist of leaves with similar characteristics. Plotting the first two factors using cluster membership as an identifier revealed three separate groups of samples (Fig. 5). It clearly proves that the optimal number of clusters has been determined properly, reinforcing the preceding conclusion.

One-way analysis of variance has been performed to evaluate the variability between clusters at the optimal level of hierarchy. Significant differences were observed only in terms of LU, LY, BC, L, a and b variables (Tab. 6). Cluster 2 differed significantly from the others in carotenoids content but differences between the first and the third cluster in terms of these substances were negligible. No significant differences in terms of colour were observed between the first and the second cluster whereas the third cluster characterised with significantly lower lightness and redness as well as significantly higher yellowness than samples within other clusters. Generally one may

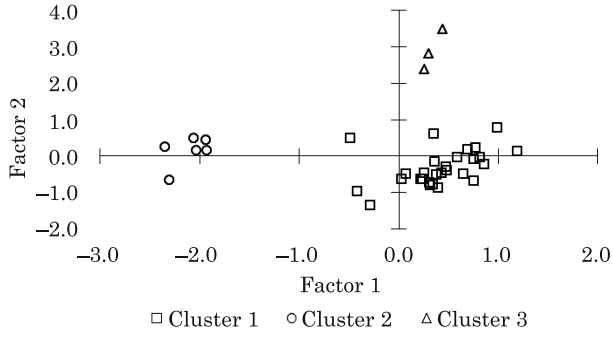

Fig. 5. Cluster membership vs. factor pattern

Table 6

ANOVA results and homogeneous groups for clusters

Cluster	Statistic	LU	LY	BC	*L*	*a*	*b*
1	Mean	0.74^{a}	0.07^{a}	0.28^{a}	70.23^{b}	4.38^{a}	29.64^{a}
	SD	0.50	0.09	0.13	3.98	1.21	4.03
2	Mean	3.12^{b}	0.26^{b}	1.07^{b}	67.93^{ab}	4.26^{a}	25.20^{a}
	SD	0.68	0.02	0.09	2.75	0.42	1.34
3	Mean	0.78^{a}	0.03^{a}	0.34^{a}	61.60^{a}	1.35^{b}	65.40^{b}
	SD	0.41	0.01	0.12	4.62	0.40	3.89

Means with the same letter do not differ significantly at $\alpha = 0.01$.

conclude that the second cluster contains samples rich in carotenoids and of light, red rather than yellow colour. However, the third cluster represented samples significantly less rich in carotenoids and darker, less red and consequently more yellow than samples within the second cluster.

Figure 6 represents the results of cluster analysis for 37 CTD combinations with respect to their impact on *b* (Fig. 6*a*), *a* (Fig. 6*b*), BC (Fig. 6*c*) and LU (Fig. 6*d*). Dashed line indicates the clustering level at which objects within each cluster are the most similar. This specific level of hierarchy was determined in such a way that the RSQ value at each level n (RSQn) was compared with the RSQ value at the previous level n^{-1} (RSQn^{-1}). If (RSQn – RSQn^{-1}) started to be greater than 0, number of clusters n was considered to provide the greatest similarity of objects before they variance starts to grow considerably within each cluster. Levels of hierarchy determined hereby were 13, 8, 13 and 13 for *a*, *b*, BC and LU respectively. Each branch or leave separated by the dashed line, received a partial score (s) between 0 and 1 based on mean values of its responses (*b*, *a*, BC and LU). All partial scores obtained for each CTD combination were calculated by equation (1) and presented as a total score (S) in Table 7.

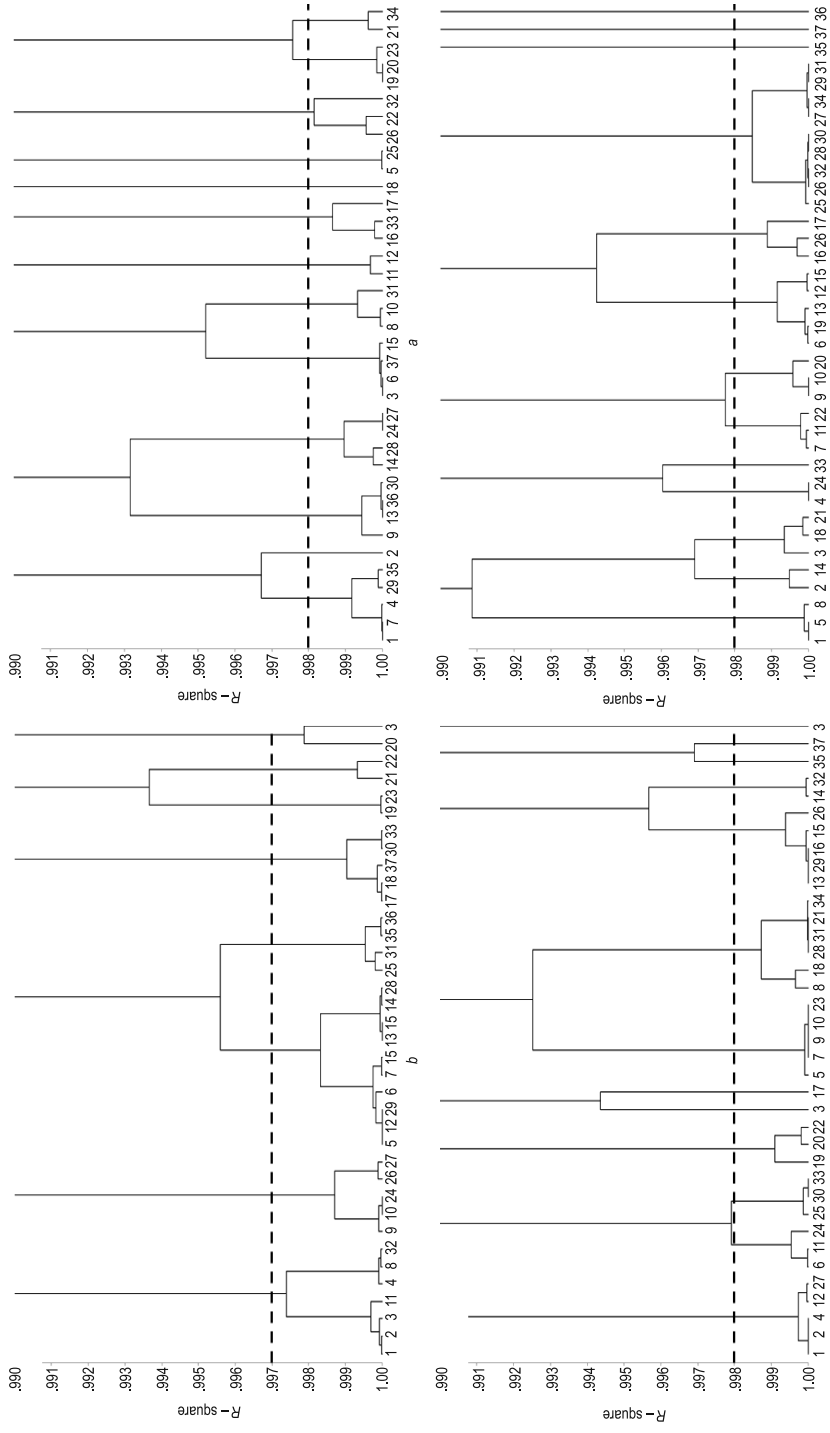

Fig. 6. Tree diagrams obtained with respect to *b* (*a*), *a* (*b*), BC (*c*) and LU (*d*)

Table 7
Scores obtained for CTD combinations based on tree diagrams of *b*, *a*, BC and LU variables

Label	B60F	J40H	Z50F	J50H	Z40N	Z70N	J60H	Z50N	J60F	J70F	Z70F	Z60N	B70F
Object	1	2	3	4	5	6	7	8	9	10	11	12	13
s_b	0.81	0.81	0.81	0.81	0.88	0.88	0.88	0.81	0.73	0.73	0.81	0.88	0.88
s_a	0.47	0.42	0.62	0.47	0.30	0.62	0.47	0.67	0.57	0.67	0.78	0.78	0.57
s_{BC}	0.16	0.16	0.57	0.16	0.08	0.21	0.08	0.12	0.08	0.08	0.21	0.16	0.04
s_{LU}	0.38	0.34	0.31	0.09	0.38	0.21	0.13	0.38	0.16	0.16	0.13	0.21	0.21
Total score (S)	0.39	0.37	0.54	0.28	0.30	0.39	0.25	0.39	0.27	0.28	0.36	0.39	0.26
Label	J70H	B50F	Z60H	Z80N	J80F	Z50H	Z40H	Z80H	Z80F	Z70H	B40F	B60N	J50N
Object	14	15	16	17	18	19	20	21	22	23	24	25	26
s_b	0.88	0.88	0.88	1.00	1.00	0.10	0.00	0.18	0.18	0.10	0.73	0.92	0.73
s_a	0.52	0.62	0.87	0.87	1.00	0.04	0.04	0.00	0.16	0.04	0.52	0.30	0.16
s_{BC}	0.00	0.04	0.04	0.49	0.12	0.31	0.31	0.12	0.31	0.08	0.21	0.24	0.04
s_{LU}	0.34	0.21	0.25	0.25	0.31	0.21	0.16	0.31	0.13	0.25	0.09	0.00	0.00
Total score (S)	0.00	0.27	0.30	0.57	0.44	0.12	0.00	0.00	0.18	0.09	0.29	0.00	0.00
Label	J50F	B40N	J80N	B80N	J70N	J40N	B80F	J40F	**B60H**	**B40H**	**B80H**		
Object	27	28	29	30	31	32	33	34	**35**	**36**	**37**		
s_b	0.73	0.88	0.88	1.00	0.92	0.81	1.00	0.00	**0.92**	**0.92**	**1.00**		
s_a	0.52	0.52	0.47	0.57	0.67	0.16	0.87	0.00	**0.47**	**0.57**	**0.62**		
s_{BC}	0.16	0.12	0.04	0.24	0.12	0.00	0.24	0.12	**0.93**	**0.82**	**1.00**		
s_{LU}	0.00	0.00	0.00	0.00	0.00	0.00	0.04	0.00	**0.83**	**0.62**	**1.00**		
Total score (S)	0.00	0.00	0.00	0.00	0.00	0.00	0.31	0.00	**0.76**	**0.72**	**0.89**		

The highest total score (0.89) was determined for cultivar *Ambar* dried at 80°C using hybrid method (B80H). Two subsequent but lower scores (0.76, 0.72) were obtained for samples of the same cultivar, dried using also hybrid method at 60°C and 40°C respectively (B60H and B40H). All these samples were members of the same, second cluster. These results are partially in agreement with those reported by ROONGRUANGSRI and BRONLUND (2016). The authors proposed 60°C as the optimal temperature of hot-air drying of pumpkin powder since the moisture content and water activity values were within acceptable limits for safe storage.

Conclusions

Results of this study showed that cultivar and drying method considerably affected the quality of dried pumpkin. Dried material obtained by a combination of tunnel drying and fluidized-bed drying characterised with high content of carotenoids despite of slightly weaker colour parameters. In general, this drying method maintained the quality of dried material on a reasonable level.

The highest contribution to the variability of samples had redness, yellowness, β-carotene and lutein content. With respect to colour and selected

chemical components, samples of dried pumpkin were divided into three groups which differed significantly in colour and a total content of carotenoids.

Scoring function allowed to find conditions of hybrid drying which resulted in simultaneous maximisation of lutein, β-carotene, redness and yellowness of dried pumpkin samples. *Ambar* samples dried at 80°C using hybrid method proved to be the best combination of cultivar and drying conditions. Moreover, with respect to colour and chemical composition, the best three combinations were B80H, B60H and B40H, which formed separate cluster. Samples within this cluster were significantly more rich in β-carotene and lutein than the others.

However, further research are necessary to study thoroughly the effect of drying temperature on colour and nutritional value of pumpkin samples subjected to hybrid drying and a long-term storage.

Additional studies should also provide more information on whether lutein, β-carotene, redness and yellowness are sufficient enough to monitor the quality of dried pumpkin and how they change thorough out the drying process considering different drying methods. And finally further studies are necessary to analyse the specificity of fluidised bed drying of convectively pre-dried pumpkin samples in terms of carotenoids and colour retention.

Acknowledgements

The authors are grateful to Dr. Aleksandra Korzeniewska and her team from the Department of Plant Genetics, Breeding, and Biotechnology at the Faculty of Horticulture, Biotechnology and Landscape Architecture, Warsaw University of life sciences – SGGW for providing research material used in this study.

References

Adams G.G., Imran S., Wang S., Mohammad A., Kok S., Gray D.A., Channell G.A., Morris G.A., Harding S.E. 2011. *The hypoglycaemic effect of pumpkins as anti-diabetic and functional medicines*. Food Research International, 44(4): 862–867.

Alibas I. 2007. *Microwave, air and combined microwave-air-drying parameters of pumpkin slices.* LWT – Food Science and Technology, 40(8): 1445–1451.

Aronson D. 2003. *Crosslinking of glycated collagen in the pathogenesis of arterial and myocardial stiffening of aging and diabetes.* Journal of Hypertension, 21: 3–12.

Burg M.B. 1995. *Molecular basis of osmotic regulation*. American Journal of Physiology, 268: 983–996.

Cai T., Li Q., Yan H., Li N. 2003. *Study on the hypoglycemic action of pumpkin seed protein*. Journal of Chinese Institute of Food Science and Technology, 3(1): 7–11.

Carvalho De L.M.J., Gomes P.B., Oliveira Godoy De R.L., Pacheco S., Montedo P.H.F., Carvalhode J.L.V., Nutti M.R., Neves A.C.L., Vieira A.C.R.A., Ramos S.R.R. 2012. *Total*

carotenoid content, α-carotene and β-carotene, of landrace pumpkins (Cucurbita moschata Duch): A preliminary study. Food Research International, 47(2): 337–340.

CIE Technical Report. 2004. *Colorimetry* (3rd edition) CIE Publication 15:2004. Central Bureau, Vienna.

DIAMANTE L.M., MUNRO P.A. 1993. *Mathematical modelling of the thin layer solar drying of sweet potato slices.* Solar Energy, 51: 271–276.

DIRIM S.N., ÇALIŞKAN G. 2012. *Determination of the effect of freeze drying process on the production of pumpkin (Cucurbita Moschata) puree powder and the powder properties.* The Journal of Food, 37(4): 203–210.

DIVYA P., PUTHUSSERI B., NEELWARNE B. 2012. *Carotenoid content, its stability during drying and the antioxidant activity of commercial coriander (Coriandrum sativum L.) varieties.* Food Research International, 45(1): 342–350.

DOYMAZ İ. 2007. *The kinetics of forced convective air-drying of pumpkin slices*. Journal of Food Engineering, 79(1): 243–248.

DU J.H., FU Y.H., WANG N.Y. 2009. *Effects of aqueous chlorine dioxide treatment on browning of fresh-cut lotus root.* LWT – Food Science and Technology, 42(2): 654–659.

ERTEKIN C., YALDIZ O. 2004. *Drying of eggplant and selection of a suitable thin layer drying model.* Journal of Food Engineering, 63: 349–359.

FALADE K.O., SHOGAOLU O.T. 2010. *Effect of pretreatments on air-drying pattern and color of dried pumpkin (cucurbita maxima) slices.* Journal of Food Process Engineering, 33(6): 1129–1147.

FORTUNA T., JUSZCZAK L., SOBOLEWSKA-ZIELIŃSKA J. 2003. *Podstawy analizy żywności*. Wydawnictwo AR w Krakowie.

GLIEMMO M.F., LATORRE M.E., GERSCHENSON L.N., CAMPOS C.A. 2009. *Color stability of pumpkin (Cucurbita moschata, Duchesne ex Poiret) puree during storage at room temperature: Effect of pH, potassium sorbate, ascorbic acid and packaging material.* LWT – Food Science and Technology, 42(1): 196–201.

GUINÉ R.P.F., PINHO S., BARROCA M.J. 2011. *Study of the convective drying of pumpkin (Cucurbita maxima).* Food and Bioproducts Processing, 89(4): 422–428.

HENRIQUES F., GUINÉ R.P.F., BARROCA M.J. 2012. *Influence of Drying Treatment on Physical Properties of Pumpkin.* Croatian Journal of Food Technology, Biotechnology and Nutrition, 7(Special Issue): 53–58.

KITINOJA L., KADER A.A. 2002. *Small-scale postharvest handling practices: A manual for horticultural crops* (4th ed., pp. 133-138). Davis, CA.

KONOPACKA D., SEROCZYNSKA A., KORZENIEWSKA A., JESIONKOWSKA K., NIEMIROWICZ-SZCZYTT K., PIOCHARSKI, W. 2010. *Studies on the usefulness of Cucurbita maxima for the production of ready-to-eat dried vegetable snacks with a high carotenoid content.* LWT – Food Science and Technology, 43(2): 302–309.

KUNACHOWICZ H., NADOLNA I., PRZYGODA B., IWANOWICZ K. 2005. *Tabele składu i wartości odżywczej żywności*. Wydawnictwo Lekarskie PZWL, Warszawa.

LAGO-VANZELA E.S., NASCIMENTO DO, P., FONTES E.A.F., MAURO M.A., KIMURA M. 2013. *Edible coatings from native and modified starches retain carotenoids in pumpkin during drying.* LWT – Food Science and Technology, 50(2): 420–425.

LEŠKOVÁ E., KUBÍKOVÁ J., KOVÁCIKOVÁ E., KOŠICKÁ M., PORUBSKÁ J., HOLČÍKOVÁ K. 2006. *Vitamin losses: Retention during heat treatment and continual changes expressed by mathematical models.* Journal of Food Composition and Analysis, 19(4): 252–276.

LEWICKI P.P. 2006. *Design of hot air drying for better foods.* Trends in Food Science and Technology, 17: 153–163.

LEWICKI P.P., DUSZCZYK E. 1998. *Color change of selected vegetables during convective air drying.* International Journal of Food Properties, 1(3): 263–273.

MURILLO E., MELÉNDEZ-MARTÍNEZ A.J., PORTUGAL F. 2010. *Screening of vegetables and fruits from Panama for rich sources of lutein and zeaxanthin.* Food Chemistry, 122(1): 167–172.

MURKOVIC M., MÜLLEDER U., NEUNTEUFL H. 2002. *Carotenoid content in different varieties of pumpkins.* Journal of Food Composition and Analysis, 15(6): 633–638.

NADIAN M.H., ABBASPOUR-FARD M.H., SADRNIA H., GOLZARIAN M.R., TABASIZADEH M., MARTYNENKO A. 2016. *Improvement of kiwifruit drying using computer vision system (CVS) and ALM clustering method.* Drying Technology, DOI: 10.1080/07373937.2016.1208665.

NAWIRSKA A., FIGIEL A., KUCHARSKA A.Z., SOKÓŁ-ŁĘTOWSKA A., BIESIADA A. 2009. *Drying kinetics and quality parameters of pumpkin slices dehydrated using different methods.* Journal of Food Engineering, 94(1): 14–20.

PEREZ N.E., SCHMALKO M.E. 2007. *Convective drying of pumpkin: influence of pretreatment and drying temperature.* Journal of Food Process Engineering, 32(1): 88–103.

PLA M.F.E., PONCE N.M., STORTZ C.A., GERSCHENSON L.N., ROJAS A.M. 2007. *Composition and functional properties of enriched fiber products obtained from pumpkin (Cucurbita moschata Duchesne ex Poiret).* LWT – Food Science and Technology, 40(7): 1176–1185.

PN-R-04013. 1988. *Analiza chemiczno-rolnicza roślin. Oznaczanie powietrznie suchej i suchej masy*. PKN, Warszawa.

RAKCEJEVA T., GALOBURDA R., CUDE L., STRAUTNIECE E. 2011. *Use of dried pumpkins in wheat bread production.* Procedia Food Science, 1: 441–447.

ROBINSON W.G., KADOR J.P., KINOSHITA J.H. 1983. *Retinal capillaries: Basement membrane thickening by galactosemia prevented with aldose reductase inhibitor.* Science, 221: 1177–1178.

ROBINSON W.G., NAGATA M., LAVER N., HOHMAN T.C., KINOSHITA J.H. 1989. *Diabetic-like retinopathy in rat prevented with an aldose reductase inhibitor.* Investigative Ophthalmology & Visual Science, 30: 2285–2292.

ROONGRUANGSRI W., BRONLUND J.E. 2016. *Effect of air-drying temperature on physico-chemical, powder properties and sorption characteristics of pumpkin powders.* International Food Research Journal, 23(3): 962–972.

SARLE W.S. 1983. *Cubic Clustering Criterion*. SAS Technical Report A-108, SAS Institute Inc., Cary, NC.

SEVERINI C., BAIANO A., DE PILLI T., CARBONE B.F, DEROSSI A. 2005. *Combined treatments of blanching and dehydration: study on potato cubes.* Journal of Food Engineering, 68(3): 289–296.

SOJAK M., GŁOWACKI S. 2010. *Analysis of giant pumpkin (Cucurbita maxima) drying kinetics in various technologies of convective drying.* Journal of Food Engineering, 99: 323–329.

TERAZOWA Y., ITO K., YOSHIDA K. 2001. *Changes in carbohydrate composition in pumpkin (kabocha) during fruit growth.* Journal of the Japanese Society Horticultural Science, 70: 656–658.

THOMAS M.C., BAYNES J.W., THORPE S.R., COOPER M.E. 2005. *The role of AGEs and AGE inhibitors in diabetic cardiovascular disease.* Current Drug Targets, 6: 453–474.

USDA. 2004. *National Nutrient Database for Standard Reference: Nutritional Value of Pumpkin and Winter Squash*. Release 17, Beltsville, MD.

WADA R., YAGIHASHI S. 2005. *Role of advanced glycation end products and their receptors in development of diabetic neuropathy.* Annals of the New York Academy of Science, 1043: 598–604.

WANG S.M., YU D.J., SONG K.B. 2011. *Physicochemical Property of Pumpkin Slices Dehydrated with Red Algae Extract.* Journal of the Korean Society for Applied Biological Chemistry, 54(6): 921–925.

WANG X., ZHANG L.S., DONG L.L. 2012. *Inhibitory effect of polysaccharides from pumpkin on advanced glycation end-products formation and aldose reductase activity.* Food Chemistry, 130(4): 821–825.

XIONG X., CAO J. 2001. *Study of extraction and isolation of effective pumpkin polysaccharide component and its reducing glycemia function.* Chinese Journal Modern Application Pharmacy, 18: 662–664.

YOUNG R.J., EWING D.J., CLARKE B.F. 1983. *A controlled trial of sorbinil, an aldose reductase inhibitor, in chronic painful diabetic neuropathy.* Diabetes, 32: 938–942.

ZHANG Y., WANG L., YAO H. 2002. *Study on the biological effects and extraction of blood glucose lowering active component from pumpkin.* Food and Fermentation Industries, 28(6): 32–35.

ZHANG Y., YAO H. 2002. S*tudy on effect of hypoglycemia of different type pumpkin*. Journal of Chinese Food Science, 23: 118–120.

Technical Sciences, 2016, 19(4), 313–324

Quarterly peer-reviewed scientific journal
ISSN 1505-4675
e-ISSN 2083-4527
TECHNICAL SCIENCES
Homepage: www.uwm.edu.pl/techsci/

EFFECT OF PLASTIC TUNNEL EQUIPMENT ON ITS THERMAL BALANCE COMPONENTS

Sławomir Kurpaska

Faculty of Production and Power Engineering
University of Agriculture in Krakow

Received 21 June 2016, accepted 26 October 2016, available online 2 November 2016.

Key words: plastic tunnel, thermal screen, thermal transmittance coefficient, convert rate of solar radiation.

Abstract

The paper presents results of research conducted in a standard plastic tunnel equipped with thermal screens measuring 144 m^2. During the experiment the thermal screens in the tunnel were either in a folded or unfolded position (both during the radiation weather and at night), whereas vents were closed. Parameters of the ambient climate (the temperature, wind velocity, air humidity and solar radiation intensity) were measured during the experiment, as well as the parameters of the microclimate inside the objects (the temperature and air humidity).Thermal balance including: the change of heat accumulated inside the object, heat gains from the substratum (through radiation and penetration), heat gains from solar radiation and the heat flux loss were formulated for the discussed cases. In result of the analysis the differences of internal temperature were stated for the object with and without thermal screens. It was found that for the identical values of the ambient climate parameters the temperature inside the object without the thermal screen was c.a. 4.0% higher than in the object equipped with the thermal screen. The thermal transmittance value through the object casing was determined and the convert rate of solar radiation to heat causing increase in the internal temperature in the objects both with and without thermal screens.

Introduction

The necessity to reduce fossil fuels consumption, care for the natural environment and striving for minimization of production costs stimulate the users, including also crop producers under plastic to apply the technical

Correspondence: Sławomir Kurpaska, Instytut Inżynierii Rolniczej i Informatyki, Uniwersytet Rolniczy im. Hugona Kołłątaja, ul. Balicka 116B, 30-149 Kraków, phone: 12 662 46 17, e-mail: rtkurpas@cyf-kr.edu.pl

solutions which would lead to decrease in heat consumption. One of the solutions conditioning effective heat consumption is installing thermal screens in horticultural facilities (e.g. in plastic tunnels). The screens are standard equipment of the objects under cover. The issues of modification of such objects construction or the effect of screen installation were addressed by studies conducted in many research centers. For instance, ZHANG et al. (1996) found that installing thermal screens in a greenhouse led to a decrease in total heat consumption on the level of 24÷26%. The Authors' own investigations (KURPASKA 2003) demonstrated that in result of installing in a greenhouse thermal screens and radiator reflector (1 m wide and 4 mm thick polyurethane covered with aluminum foil) the maximum heat saving (at the minimal ambient temperature) was almost 50%. On the other hand, studies by GRABARCZYK (2010) revealed the heat saving between 30 and 42% at the difference between the indoor and outdoor temperature in the range 5÷20 K. SETHI and SHARMA (2008) presented thermal effects obtained in the investigations conducted in greenhouses in various centres, where thermal screens were installed. Depending on the localization and screen type, obtained savings ranged from 20% (Madrid) to 60% (Pennsylvania). KITTAS et al. (2003) analyzed microclimate parameters of the objects with and without thermal screens. They established that the use of thermal screens led to a better levelling of the air temperature around the cultivated plants. Installing the screen caused almost a 15% decrease in heat demand. SILVIA et al. (1991) developed and verified a mathematical model of the sunbeams reaching the interior of a greenhouse quipped with thermal screens. Various radiation fluxes were considered, whereas detailed analysis was conducted on net radiation reaching the substrate surface in the greenhouse. Usability of the model for internal microclimate parameters control was stated. CANAKCI and AKINCI analyzed the costs of various vegetables production in a greenhouses with diverse equipment, including these with and without thermal screens. They established, that under the investigated conditions (the Mediterranean area) heat costs constituted between 19 and 32% of all operational costs for the discussed vegetable species. CELIK and MUNEER (2013) tested the effects of solar radiation conversion (measured by two independent pyranometers: horizontal and parallel with the roof surface) in photovoltaic panels integrated with the greenhouse construction. Generated energy was accumulated in batteries. The forecast was based on SSN in which input variables were reduced to the radiation intensity and incidence angle of the sunbeams. It was found that the final result of the conversion, as compared with the standard models, was characterized by a lower value of estimated intensity reaching the sunlit surface. NAYAK and TIWARI (2008) analyzed the system composed of a laboratory tunnel and photovoltaic panels. The panels

were installed on the roof. Beside the energy issues (annual and daily gain of electrical energy, effectiveness of solar radiation conversion) the authors developed a mathematical model of heat and mass transfer inside the facility. The model included real geometry of the studied object. TEITEL et al. (2009) analyzed the change in the air temperature in a greenhouse with and without thermal screens. They determined also leaves temperature, whereas they made the energy consumption dependent on the difference in temperature between the leaf and the indoor air. They also determined the value of effective thermal transmittance through the object casing and made it dependent on wind velocity. HASSANIEN et al. (2016) made a synthetic review (combined with an economic analysis) of the implemented technical solutions using solar radiation energy in the context of ensuring the required environment conditions in a greenhouse. LAMNATOU and CHEMISANA (2013), ABDEL--GHANY and AL-HELAL (2011) analyzed the effect of diversified greenhouse cover materials on light conditions and light emission (within IR range) inside the facility. ABDEL-GHANY (2011) considered the effect of greenhouse longitudinal axis situation towards geographical directions in order to obtain the maximum insolation during the light deficiency period, recommending the east-west direction for the winter months. VADIEE and MARTIN (2014) found a considerable influence of the cover on heat transfer from inside the object to the environment, concluding that application of double glazing and thermal screens led to diminishing the light accessibility, yet the advantage of this type of cover is obtaining almost 60% savings in heat demand. In result of conducted analysis the authors stated that additional savings in heat consumption may be obtained using a semi-closed greenhouse with a dehumidifier. SANAYE and SARRAFI (2015) conducted the procedure of temperature optimization inside the object (including also controlling the position of shade screens) for the system using solar radiation. SETHI et al. (2013) made a review of technical solutions stimulating a change of the parameters of microclimate inside heated greenhouse facilities. They also discussed the application of foils preventing water vapour condensation and determined the influence of this foil on light accessibility in the range of PAR length. YANO et al. (2014) analyzed in detail a prototype greenhouse where PV cells were applied on a part of the roof. Beside determining the amount of generated energy, they also investigated a change in light accessibility inside the facility.

The review of research works presented above shows unanimously that the problems of environmental conditions inside a greenhouse facility, analysis of thermal issues under the influence of the construction or technical equipment modification are still relevant research problems. Therefore the aim of the paper was an analysis of thermal balance components describing a horticul-

tural facility together with an analysis of the intensity of the change of solar radiation conversion to heat in the objects where thermal screens were installed.

Material and Methods

The investigations were conducted in a tunnel measuring 9×16 m, covered with double skinned PE foil; white foil was placed inside the tunnel on a substratum. During the experiment the thermal screens in the object were either folded or unfolded (both during the radiation weather and at night), whereas the vents were closed.

The temperature was measured during the experiment using PT 1000 meters, relative air humidity by means of HD 4917 meters, wind velocity using a cup anemometer and the intensity of solar radiation by means of LP PYRA 02AV pyranometer. The scheme of the measurement station with marked thermal balance components and measured values were presented in Figure 1.

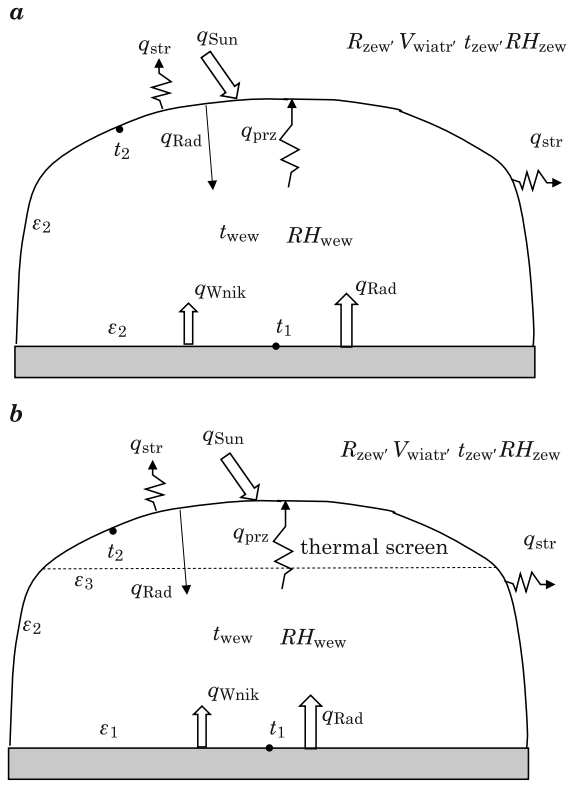

Fig. 1. Scheme of test bench without (*a*) and with (*b*) thermal screens installed inside the tunnel

In the differential time ($d\tau$) the energy balance of analyzed tunnel volume under the conditions of radiation weather may be described as follows:

$$V_p \cdot \rho \cdot c_w \frac{dt_{\text{wew}}}{d\tau} = q_{\text{Sun}} + q_{\text{Rad}} + q_{\text{Wnik}} - q_{\text{str}} \tag{1}$$

whereas after taking into consideration the elementary dependence as:

$$V_p \cdot \rho \cdot c_w \frac{dt_{\text{wew}}}{d\tau} = f \cdot F_{\text{tun}} + R_{\text{zew}} + \varepsilon_{\text{ef}} \cdot \sigma \cdot F_{\text{tun}} \left(\left(\frac{T_1}{100} \right)^4 - \left(\frac{T_2}{100} \right)^4 \right) + \\ + \alpha_{\text{wnik}} \cdot F_{\text{tun}} \cdot (t_1 - t_{\text{wew}}) - U_{\text{osł}} \cdot F_{\text{osł}} \cdot (t_{\text{wew}} - t_{\text{ot}}) \tag{2}$$

Alternative emission (ε_{ef}) of the substratum top layer was computed from the following dependence:

$$\varepsilon_{\text{ef}} = \frac{1}{\frac{1}{\varepsilon_1} + \frac{F_{\text{tun}}}{F_{\text{osł}}} \left(\frac{1}{\varepsilon_2} - 1 \right)} \tag{3}$$

where:
V_p – volume of air [m^3],
ρ – air density [$kg \cdot m^{-3}$],
c_w – sensible heat of the air [$J \cdot kg^{-1} \cdot K^{-1}$],
T_{wew} – temperature inside [K],
q_{Sun} – heat flux transmitted to the interior of the solar radiation [W],
q_{Rad} – heat flux transferred from the substrate surface to the interior [W],
f – conversion of radiation into heat [–],
R_{zew} – the intensity of solar radiation [$W \cdot m^{-2}$]
ε_{ef} – effective emission coefficient [–],
σ – Stefan-Boltzmann constant $\sigma = 5.67$ [$W \cdot m^{-2} \cdot K^{-4}$],
T_1, T_2 – emperature of the surface layer of the substrate (T_1) and shields (T_2) [K],
α_{wnik} – heat transfer coefficient between the air and the top layer of the substrate [$W \cdot m^{-2} \cdot K^{-1}$],
T_{ot} – ambient temperature [K],
$U_{\text{osł}}$ – heat transfer coefficient of the cover [$W \cdot m^{-2} \cdot K^{-1}$],
$F_{\text{osł}}$ – surface shields tunnel [m^2],
F_{tun} – usable area tunnel [m^2],
ε_1, ε_2, ε_3 – emissivity surface tunnel (ε_1), shields (ε_2) and screen heat (ε_3) [–].

When the alternative emission factor for the object with the thermal screen was determined, the final value of the (ε_2) parameter was computed as a weighted average considering the casing and thermal screen area. Heat penetration coefficient (α_{wnik}) was calculated using standard dependencies between criteria of similarity.

The methods presented above show that determining the convert rate of solar radiation (f) is possible when the thermal transmittance value through the casing ($U_{osł}$) has been established at the first stage of research. Therefore, after finding the relationship of this coefficient (U_{ost}) as a function of measured ambient climate parameters, the obtained value was applied for the analysis of the period with radiation weather. The necessary parameters (ambient climate and inside the object) were monitored and saved by a computer system with sampling time equaling 30 s. The temperature of the object casing was computed in accordance with generally used dependencies as 40% of the ambient temperature value and 60% of the temperature inside, whereas the temperature of the substratum top layer was measured by resistance sensor.

Computations of the air parameters (c_w, ρ) were conducted using standard psychrometric dependencies. Quantitative measures of approximation accuracy (compliance) of the parameter computed from the conducted measurements with the values approximated by the model were determined from mean square error (σ) known from the elemental error calculation.

Results and Discussion

The investigations conducted when no plants were cultivated for the following range of variable values (the data refer to both radiation weather and solar radiation decay):

a) tunnel without thermal screen: $-3 \le T_{wew} \le 35.1$ [°C]; $17.1 \le RH_{wew} \le 92$ [%]; $-4.5 \le T_{zew} \le 14.9$ [°C]; $0 \le V_{wiatr} \le 2.0$ [m · s^{-1}]; $0 \le R_{zew} \le 380$ [W · s^{-2}]; $35.9 \le RH_{zew} \le 100$ [%];

b) tunnel with thermal screen: $-3 \le T_{wew} \le 33.8$ [°C]; $22.1 \le RH_{wew} \le 89.6$ [%]; $-2.3 \le T_{zew} \le 15.9$ [°C]; $0 \le V_{wiatr} \le 1.9$ [m · s^{-1}]; $0 \le R_{zew} \le 395$ [W · s^{-2}]; $35.2 \le RH_{zew} \le 100$ [%].

Figure 2 presents the dependence of the temperature inside the objects (with and without thermal screens) as a function of ambient temperature and solar radiation intensity.

The equation found for measured values (t_{wew}), comprising the relationship between this value and independent variables (the form of power model was selected on the basis of the highest value of determination coefficient; the dependency was determined by non-linear estimation using quasi-Newton

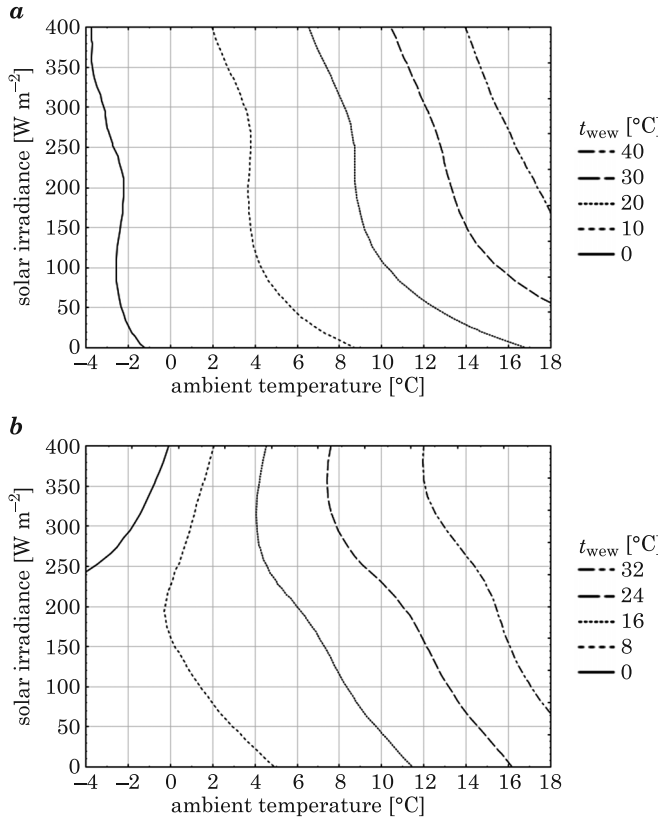

Fig. 2. Course of internal temperature as a function of ambient climate parameters for the object (*a*) without and (*b*) with thermal screen

method at maintained convergence coefficient 0.001), assumes the following form:

a) tunnel without thermal screen; $R^2 = 0.96$

b) tunnel with thermal screen; $R^2 = 0.95$

The dependencies given above may be applied within the stated range of experimental variables. Comparison between the values measured and computed from the suggested models were presented in Figure 3.

Detailed analysis revealed that for the same values of the ambient climate parameters, the temperature inside the object without a thermal screen was by c.a.4% higher in comparison with the temperature in the object equipped with thermal screen.

Using the derived dependencies, thermal transmittance value through the object casing ($U_{osł}$)was calculated. The course of its value as a function of the experimental variables: the difference in temperature (between the tunnel interior and ambient air) and wind velocity was presented in Figure 4.

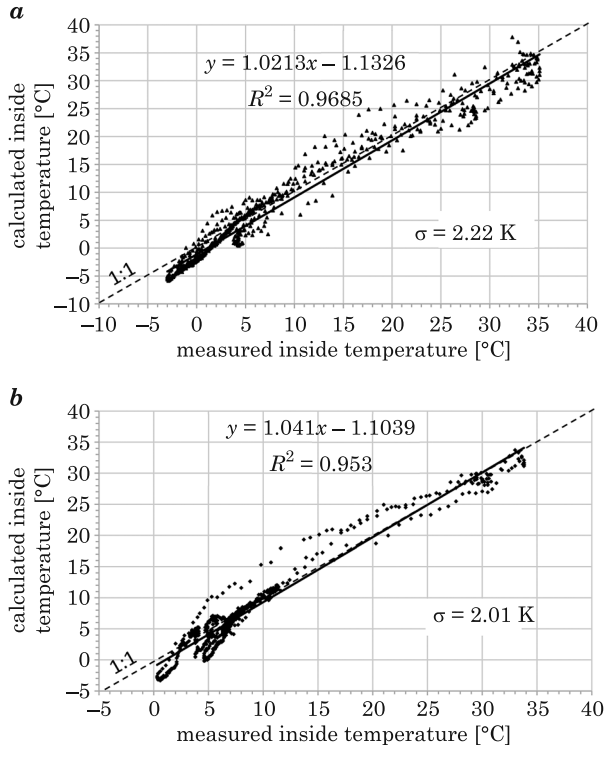

Fig. 3. Comparison of the temperature computed from the models and the values measured for the object (*a*) without and (*b*) with thermal screen

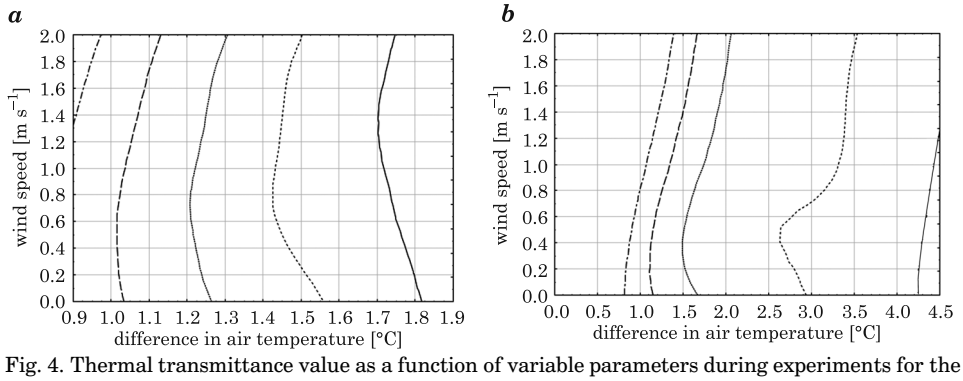

Fig. 4. Thermal transmittance value as a function of variable parameters during experiments for the object (*a*) without and (*b*) with thermal screen

It may be seen that in both cases thermal transmittance value ($U_{osł}$) is an increasing function of the difference of temperature and wind velocity. Mean thermal transmittance value in the analyzed range of the experimental parameters is 5.32 for the object without thermal screen and 4.61 $W \cdot m^{-2} \cdot K^{-1}$ for the object with a thermal screen.

Using the value of $U_{osł}$ computed for the period without solar radiation, the values of individual heat fluxes were calculated for both objects; additionally a change was marked in the amount of heat accumulated in their interior. The results were shown in Figure 5.

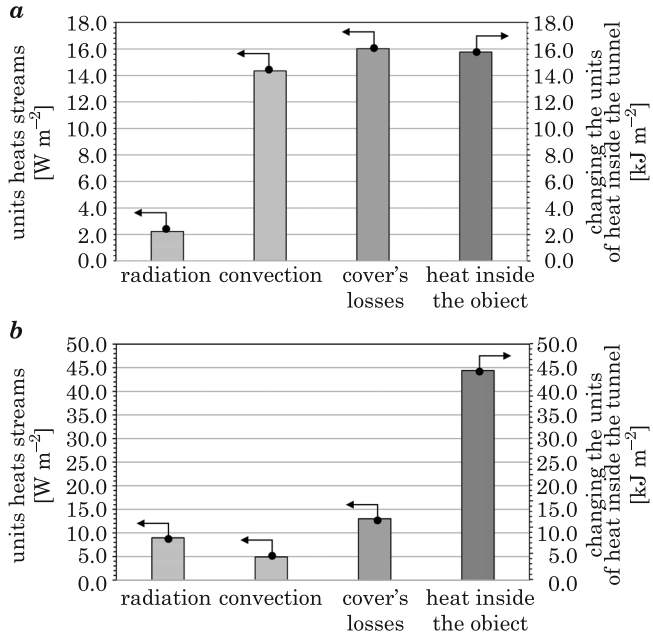

Fig. 5. Values of individual components of thermal balance in the objects for a selected cycle without solar radiation for the object (*a*) with and (*b*) without thermal screen

Conducted detailed analysis for the performed experimental cycles revealed that heat transfer through radiation was c.a. 18% of the total heat flux loss in the object without thermal screen, whereas for the object with thermal screen, mean values are about 68%. The final conclusion of the conducted analysis is determining the convert rate of solar radiation to heat (*f*) whose course as a function of solar radiation intensity was presented in Figure 6.

As may be seen, the value of this rate is growing with increasing solar radiation intensity. Mean values of this rate in the studied range of the ambient climate parameter values are 0.36 for the object without a thermal screen and 0.26 for the object with a thermal screen. It denotes that depending on the equipment, between 26% and 36% of solar radiation energy measured outside the tunnel is converted into heat.

Analyzing the obtained values and their dependencies on the ambient climate parameters it may be stated clearly, that apart from cognitive advan-

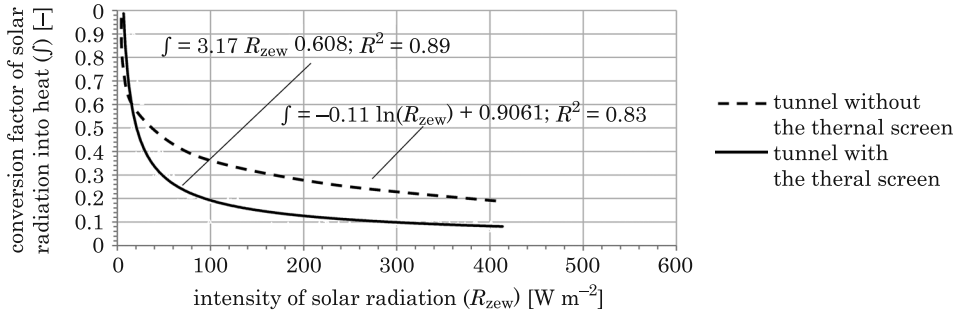

Fig. 6. Changeability of conversion rate of solar radiation to heat (*f*) inside the tunnel for the tested equipment

tages, they may find applications also for control of the microclimate parameters inside the object.

The values may prove debatable in the tunnel where plants are grown, because of additionally occurring heat flux used for plant transpiration, however it would not impact their tendencies and trends of changes.

Conclusions

1. For identical parameters of the ambient climate, the temperature inside the object without a thermal screen is about 4% higher compared to the temperature in the object equipped with thermal screen.

2. Mean thermal transmittance value in the analyzed range of climate parameters is 5.32 for the object without a thermal screen and 4.61 W · m^{-2} · K^{-1} for the object with a thermal screen.

3. Heat transfer through radiation in the object without thermal screen is c.a. 18% of the total heat flux loss, whereas for the object with the screen mean value is around 68%.

4. Mean value of convert rate of solar radiation to heat in the investigated range of ambient climate is 0.36 for the tunnel without a thermal screen and 0.26 for the object with thermal screen.

The Research was financed by the Ministry of Science and Higher Education of the Republic of Poland

References

Abdel-Ghany A.M. 2011. *Solar energy conversions in the greenhouses*. Sustainable Cities and Society, 1: 219–226.

Abdel-Ghany A.M., Al-Helal I.M. 2011. *Solar energy utilization by a greenhouse: general relations*. Renewable Energy, 36: 189–196.

CANAKCI M., AKINCI I. 2006. *Energy use pattern analyses of greenhouse vegetable production*. Energy, 31(8–9): 1243–1256.

CELIK A.N., MUNEER T. 2013. *Neural network based method for conversion of solar radiation data*. Energy Conversion and Management, 67: 117–124.

GRABARCZYK S. 2010. *Badania zmienności zużycia ciepła w szklarniach z osłonami energooszczędnymi*. Czasopismo Techniczne, Wydawnictwo Politechniki Krakowskiej, 2-B, 4(107): 67–74.

KITTAS C., KATSOULAS N., BAILLE A. 2003. *Influence of an aluminized thermal screen on greenhouse microclimate and canopy energy balance*. Transactions of the ASAE, 46(6): 1653–1663.

KURPASKA S. 2003. *Modyfikacja wyposażenia technicznego tunelu foliowego w aspekcie jego zapotrzebowania na ciepło*. Problemy Inżynierii Rolniczej, 1: 39–46.

LAMNATOU C., CHEMISANA D. 2013. *Solar radiation manipulations and their role in greenhouse claddings: fluorescent solar concentrators, photoselective and other materials*. Renewable and Sustainable Energy, 27: 175–190.

NAYAK S., TIWARI G.N. 2008. *Energy and exergy analysis of photovoltaic/thermal integrated with a solar greenhouse*. Energy and Buildings, 40(11): 2015–2021.

SANAYE S., SARRAFI A. 2015. *Optimization of combined cooling, heating and power generation by a solar system*. Renewable Energy, 80: 699–712.

SILVA A.M., MIGUEL A., ROSA R. 1991. *Thermal radiation inside a single span greenhouse with a thermal screen*. Journal of Agricultural Engineering Research, 49: 285–298.

SETHI V.P., SUMATHY K., LEE C., PAL D.S. 2013. *Thermal modeling aspects of solar greenhouse microclimate control: a review on heating technologies,* Solar Energy, 96: 56–82.

TEITEL M., BARAK M., ANTLER A. 2009. *Effect of cyclic heating and a thermal screen on the nocturnal heat loss and microclimate of a greenhouse*. Biosystems Engineering, 102(2): 162–170.

VADIEE A., MARTIN V. 2014. *Energy management strategies for commercial greenhouses*. Applied Energy, 114: 880–888.

ZHANG Y., GAUTHIER L., HALLEUX DE D., DANSEREAU B., GOSSELIN A. 1996. *Effect of covering materials on energy consumption and greenhouse microclimate*. Agricultural and Forest Meteorology, 82(1–4): 227–244.

YANO A., ONOE M., NAKATA J. 2014. *Prototype semi-transparent photovoltaic modules for greenhouse roof applications*. Biosystems Engineering, 122: 62–73.

Technical Sciences, 2016, 19(4), 325–337

Quarterly peer-reviewed scientific journal
ISSN 1505-4675
e-ISSN 2083-4527
TECHNICAL SCIENCES
Homepage: www.uwm.edu.pl/techsci/

INFLUENCE OF GRANULAR BED PARAMETERS ON EMULSION FLOW AND ELUTION PROCESS OF OIL-IN-WATER EMULSION

Mariola Błaszczyk, Piotr Pacholski, Łukasz Przybysz, Jerzy Sęk

Department of Chemical Engineering
Lodz University of Technology

Received 7 June 2016, accepted 7 November 2016, available online 10 November 2016

Key words: porous media, oil-in-water emulsion, elution.

Abstract

Emulsion flow through porous structure is used in many processes in the field of chemical engineering. Good examples of practical applications are Enhanced Oil Recovery (EOR) techniques, soil remediation and treatment of oily wastewater. The emulsion transport in through porous media is not easy to describe, due to rheological behavior of emulsions and porous structure properties. In case of emulsified system flow through porous bed it is possible to observe the retention of oil on porous structure, and reduction of permeability of bed. In the presented study, we tried to investigate the influence of porous bed parameters on oil-in-water emulsion behavior during its flow and elution from porous structure. In experiments we used porous beds with varied particle size range and with different lengths. We measured pressure drop and related permeability changes in time. The turbidimetric and microscopic analysis that we conducted allowed us to check how concentration of emulsion changed during its flow and elution from porous structure.

Symbols:

L_z – porous bed length [m]
Δp – pressure difference [Pa]
c_e – concentration of base emulsion [%]
c_w – concentration of emulsion during experiment [%]
ε – porosity of medium
Q_v – volumetric flow rate [m^3/s]
k – the permeability coefficient [m^2]
l – the distance of flow [m]

Correspondence: Mariola Błaszczyk, Wydział Inżynierii Procesowej i Ochrony Środowiska, ul. Wólczańska 213, 90-924 Łódź, phone: 42 631 39 75, e-mail: mariola.blaszczyk@p.lodz.pl

A – surface of cross-section of bed [m^2]
μ – dynamic viscosity of liquid [Pa · s]
n_{ei} – number of droplets with certain diameter
d_{ei} – diameter of emulsion drop

Introduction

Transport of emulsion in porous media is crucial for such processes as crude oil extraction, soil remediation and wastewater treatment (LANGEVIN et al. 2004 and YOUNG-CHUL 2007). The knowledge in field of emulsion flow in porous structure can help companies to reduce costs associated with oil recovery (CRAWFORD et al. 1997). The phenomena observed during two phase flow in porous medium are also important for geomechanics, hydrogeology and reservoir engineering (WANG 2000). Knowledge of emulsion systems migration in granular structures can contribute to the development of new techniques for obtaining oil from oil sands and oil shales (DULLIEN 1992, ALVARADO et al. 2013, BŁASZCZYK et al. 2016a). For example, in Enhanced Oil Recovery (EOR) techniques, better understanding of emulsion flow through porous media is needed for development and practical improvement of processes based on emulsion flooding mechanisms (MORADI et al. 2014, GUILLEN 2012, BŁASZCZYK et al. 2016c). It is also especially important in heavy oil recovery, where emulsified solvent flooding has been shown to be efficient technique (KUMAR et al. 2012).

Fundamental mathematical explanation of fluid flow through porous structure is given by Darcy's equation. This law can also be used to explain flow through porous bed indicated by a pump. In this case, the driving force will be the pressure difference Δp between the pressure produced by pump and the atmospheric pressure (HEINEMANN 2005). Also, for porous structure having certain length and diameter it is possible to determine the permeability coefficient according to the Darcy's law. In equation (1) parameter known as permeability coefficient is introduced. It is a measure of the ability of a porous material to allow fluids to pass through it. The Darcy's law therefore can be described as:

$$Q_v = k \frac{A}{\mu} \frac{\Delta p}{l} \tag{1}$$

Emulsion flow in porous media differs from the independent movement of individual phases, and therefore must be considered separately (IDORENYIN et al. 2012). To describe the nature of such flows, permeability reduction mechanisms and changes in concentration of internal phase must be recognized. This

allows to understand and to predict the way in which emulsion systems behave during transport in porous media. This knowledge is useful to obtain a comprehensive picture of multiphase flow in porous media.

During flow of emulsion through porous structure oil droplets can be trapped in it, because of the existing retention mechanisms of fluid in porous structure, caused by capillary forces (IRYNA et al. 2016). During the process of elution by washing liquid, these droplets can move again as emulsion systems.

In Enhanced Oil Recovery (EOR) techniques surfactants are added to the washing media, in order to reduce surface tension, and thereby increase the degree of elution. This is an additional factor causing the formation of the emulsion during the elution process (LI, GU 2005). During EOR sometimes emulsions are used to decrease mobility of the injected fluids, and they are called then extrusive liquid. They can be also applied to block highly permeable zones (MANDAL et al. 2010). However, the emulsions may also be formed in the bed by itself. For example crude oil can form dispersed system with water, since it contain naphthalene acid and resins, which exhibit the properties of natural surfactants to facilitate the formation of the emulsion structures. In such case during its extraction or transportation under shear forces emulsification phenomenon occurs. Moreover, the presence of variety of alkali in crude oil causes stabilization of formed systems. Evaluation of how the emulsions move in the granular bed, may also help to increase efficiency of soil treatment from oil-derived substances and reduce the associated financial costs (COBOS et al. 2009).

In practical situation during consideration of O/W emulsion flow process through porous medium it is important whether it can be treated as a homogeneous liquid or not. If the emulsion droplets are very small, compared to the size of the flow channels, it can be considered that the fluid behaves as one-phase medium and neglect the microscopic droplets of the emulsion (CORTIS, GHEZZEHEI 2007). However, in most practical cases, the sizes of the emulsion droplets are not significantly smaller than the pore sizes, or even larger from them, which means that their presence in the bed cannot be ignored. In such situation, it is necessary to examine how the various properties of the emulsion affect the flow through a porous medium (WANG, DONG 2011)

The flow of the emulsion through the porous medium depends on the properties of both: the porous bed and the dispersed system. Properties of obtained two-phase liquid such as: stability, concentration, droplets sizes and interfacial interactions, play here particular role. As regards to the parameters characterizing granular bed, wettability, pore average size and pore size distribution are the most relevant here. Wettability of the porous medium controls the flow, location and distribution of the fluid inside the porous bed.

This parameter affects the capillary pressure, relative permeability, water and oil saturation, and other properties (DULLIEN 1992). Pore sizes and their distribution are directly related to the capture and retention of oil drops. For example in the experiment described by CAI et al. (2012), GUILLEN et al. (2012) and ALVARADO et al. (2011) it was observed that, at the beginning of the process, the concentration of emulsion that leaved the porous bed was lower than the concentration of emulsion at the inlet to porous structure. Although, after some time, the concentration of emulsion leaving the bed increases and reaches the value similar to the one at the entrance to bed. This can be related to phenomenon known as "straining", where the oil phase is retained in porous medium and water flows out. The more precise explanation of this mechanism is as following: when small pores are clogged by oil drops the flow occurs through large paths. In that pores emulsion is not captured and their structure does not change, that is why the concentration of emulsion that leaves bed not varies.

Also, the pore diameter size distribution and emulsion droplet size distribution affects the reduction of permeability (HEINEMANN 2005). It has been observed (ALVARADO et al. 2011, BŁASZCZYK et al. 2016b) that the droplets leaving porous bed at the beginning of process were smaller than the ones initially pumped. However, during the process their size changed and bigger droplets were presented in outflow, and ultimately droplet size distribution was similar to the droplets size distribution in emulsion injected to the bed. The droplet size distribution was also a subject of other experiments (COBOS et al., 2009, MORADI et al. 2014) that showed that when droplet size increased, the retention of emulsion was also higher. It was explained by the fact that the probability that bigger droplets will be trapped inside pore is greater, and they fill pores faster. The emulsions with small diameter of droplets comparing to the pore sizes generally leave bed with the same oil droplet distribution (CORTIS, GHEZZEHEI 2007).

The aim of this study was to investigate the effect of particle size fractions on the processes of emulsion flow and elution from the porous bed. For this purpose experiments with the use of glass microspheres, with three different ranges of particle size diameters were carried out. Also the influence of bed length was examined.

Materials and Methods

For experiments we used equipment presented in Figure 1. The test stand consisted of following elements: container with liquid (*1*), pressure indicator (*3*), signal converter (*2*), peristaltic pump (*4*), exchangeable tubes (*5*) that were

packed with glass microspheres and volumetric flow indicator at outflow section (*6*).

The pump that we used was peristaltic type produced by ELPIN-PLUS-model 372c. This device was calibrated before measurements to obtain its characteristics. The signal converter PT-5261M was coupled with pressure indicator MD-5270. The tubes were made from stainless steel and had length of 0.2, 0.3 and 0.5 m and diameterof 0.05 m. For emulsion preparation we used: edible oil with viscosity of 60 mPa · s and density of 865 kg/m^3 (in ambient temperature), water and emulsifier Rokacet O7 obtained from PCC Exol S.A. To emulsify the liquids we used high speed handheld homogenizer. The glass microspheres were used as the porous beds. The experiments were carried in the temperature of 22^{o}C.

The emulsion preparation technique was as follows: oil, water and emulsifier were mixed together for three minutes with high speed homogenizer to obtain dispersed system with given concentration. We prepared oil-in-water emulsion with internal phase concentration of 5% and addition of 2% Rokacet O7 as an emulsifier. The obtained system had stability time of more than 24 hours. The viscosity of prepared emulsion was also measured and equaled 1.5 mPa · s.

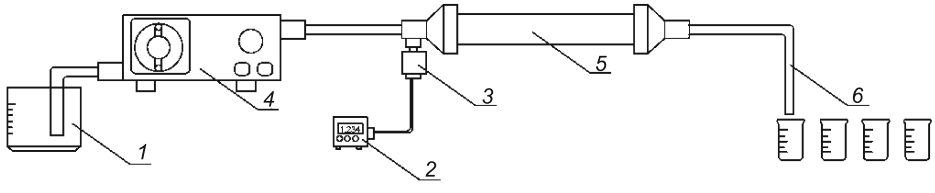

Fig. 1. Equipment used in experiments: *1* – container with liquid, *2* – signal converter, *3* -pressure indicator, *4* – peristaltic pump, *5* – tube with microspheres, *6* – outflow section with flow indicator

Before conducting the main part of the experiment we measured permeability of porous bed for water flow. In order to do so we packed the tubes with porous medium tightly, closed the tubes with nets and started to pump water. When the pressure showed by pressure indicator was stable, we noted it and calculated the permeability according to the equation (1). The results of this experiment are presented in Table 2.

To start the main part of experiment concerning emulsion flow and its elution from porous bed we placed certain amount of model porous bed in pipe. The bed was additionally compacted in order to make sure it is immovable. The experiments were conducted always with the same, previously established mass of porous bed that was also saturated with water. The tubes were equipped with rubber seals and nets preventing the bed from movement.Then

we started to pump previously prepared oil-in-water emulsion with known parameters through it. Every 30 seconds we noted pressure difference measured by pressure indicator at the inlet to the bed. The liquid at the outflow was collected in 100 ml bakers in order to conduct microscopic and turbidimetric analysis. The obtained samples allowed us to conduct further analysis of concentration of oil in them. When the steady state was reached, it means when the pressure varied by less than 0.01 bar (equivalent 10^3 Pa), we started to pump water through bed. At this time the elution process began. At this stage we continued to measure the pressure difference at the inlet and we continued to collect eluted liquid. We stopped pumping of water when the steady state was reached again. The emulsion and water were pumped with the same volumetric flow rate of $6.5 \cdot 10^{-6}$ m^3/s during the entire process.

During the experiments we focused on study of the influence of porous bed fraction and its length on the process of emulsion and water flow through porous bed. For the first experiment regarding the different porous bed fraction we prepared three different beds of microspheres with certain diameter ranges and followed the procedure presented in previous paragraph. The properties of porous media used in experiment are shown in Table 1. The second part of experiment was conducted in order to check the influence of bed length on the process of emulsion flow and elution from porous bed The experiments were conducted for the porous bed with the parameters that are shown in Table 1. For all experiments, at the beginning, we used oil-in-water emulsion with 5% concentration.

Table 1

Properties of porous media used in experiments

Bed type	Particle size range [μm]	Porosity ε	Mass [kg]		
			L_z = 0.2 m	L_z = 0.3 m	L_z = 0.5 m
Glass microspheres	90–150	0.33	0.736	1.103	1.845
Glass microspheres	150–250	0.34	–	1.090	–
Glass microspheres	200–300	0.34	–	1.088	–

In order to better understand the phenomena of permeability reduction in porous bed we decided to conduct additional experiment concerning pressure drop during flow of tap water through porous bed. The methodology of it was similar to the previous experiments, but in this case through the clean bed only tap water was pumped. In experiment we measured pressure drop, which allowed us to calculate permeability according to the equation (1).

The turbidimetric analysis of collected liquid samples was performed with TurbiscanLab® apparatus delivered by Formulaction Company (France) in

order to determine concentration of oil phase. The device scans the samples with near-infrared light. The TurbiscanLab® is equipped with two signal detectors: transmittance receiver that analyzes the light that goes through the sample and detector that receive back scattering light. The obtained results show the percentage of transmitted light (T%) and backscattering (BS%) in function of height of sample (h). The method of oil concentration determining in the samples of emulsion, which flowed out of the deposit, was developed on the basis of turbidimetric and microscopic tests, presented by LEMARCHAND et al., 2003, SĘK et al. 2011.

Emulsion structure (ie. oil droplets amount and size distribution) was examined with equipment used for analysis of microscopic images The system consisted of optic microscope Alphaphot-2 from Nikon, connected to digital video camera Panasonic GP-KR222 and computer used to analyze and data acquisition. For later droplet diameter analysis we used computer program SigmaScan PRO 5.

Results and Discussion

Microscopic analysis of emulsion droplet size and distribution

In order to correctly analyze the influence of porous bed parameters on emulsion flow through it, it is necessary to determine what parameters influence its flow. Especially important is emulsion concentration and diameter and size of droplets in it. Microscopic picture of base emulsion with 5% oil concentration used in experiments is presented in Figure 2. The system presented in Figure 2*a* is stable oil-in-water emulsion, with oil droplet size distribution showed in Figure 2*b*.

As it was mentioned, the computer program for image analysis helped us to determine the distribution of droplet size that were present in emulsified system. It also allowed us to calculate frequency of occurrence of certain oil droplets diameters, such as presented in Figure 2*b*. As it might be noticed the droplets with diameter 3–4 μm were prevailing and counted for about 40% of all drops. The diameter of emulsion droplets generally didn't exceeded 60 μm.

Additionally for calculation of mean droplet size, we used Sauter equation as following (2).

$$d_s = \frac{\Sigma n_{ei} d_{ei}^3}{\Sigma n_{ei} d_{ei}^2} \tag{2}$$

According to the equation (2) the mean drop size of equalled to 3.58 μm.

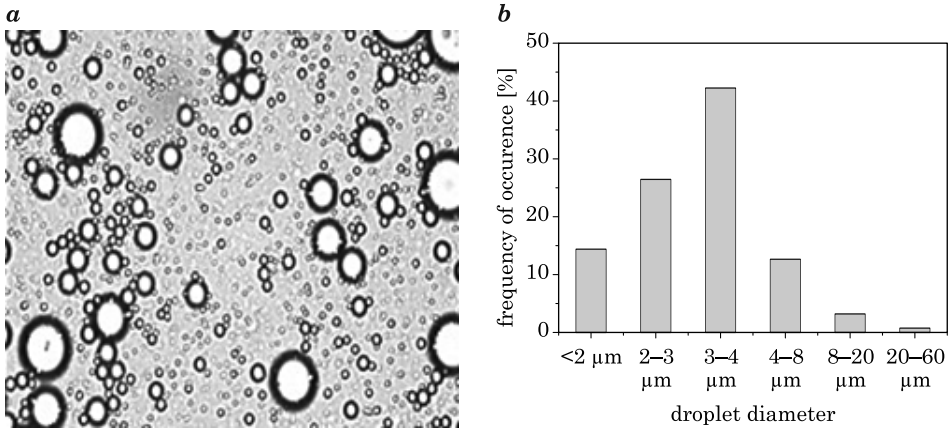

Fig. 2. Oil-in-water emulsion with 5% concentration used in experiments (*a*), droplet size distribution diagram for prepared system (*b*)

Flow resistance and concentration of emulsion change during the process of emulsion flow and elution

The results of experiments concerning pressure drop and emulsion concentration at outflow are showed in the form of graphs. In Figure 3*a* and 4*a* the inlet pressure Δp versus time is presented. In Figure 3*b* and 4*b* the concentrations c_w of emulsion leaving the porous bed versus time are shown for $L_z = 0.3$ m.

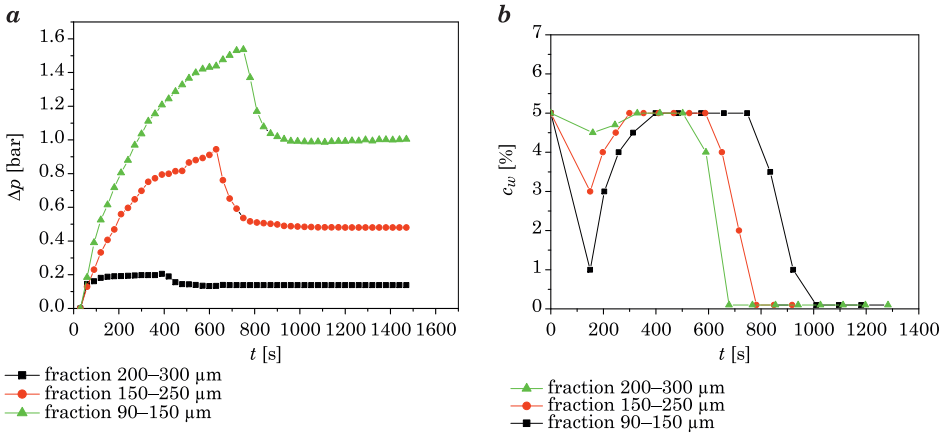

Fig. 3. Pressure difference versus time for different porous bed fractions (*a*), emulsion concentration versus time for different porous bed fractions (*b*)

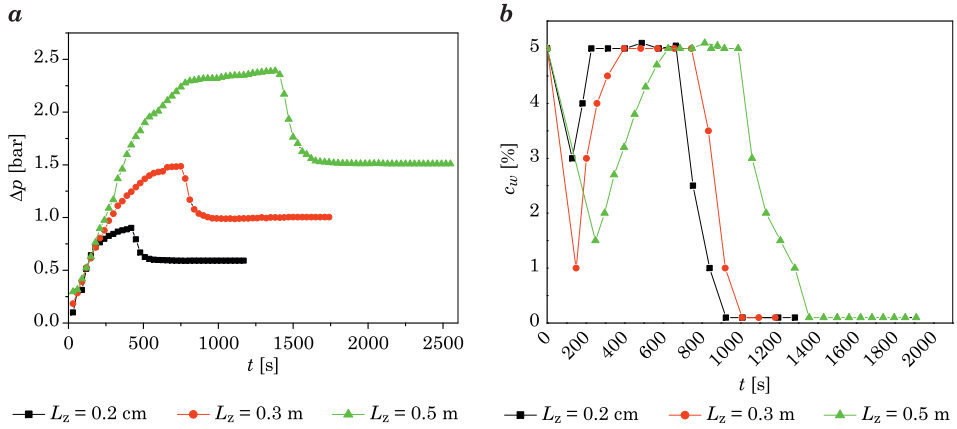

Fig. 4. Pressure difference versus time for different porous bed length (*a*), emulsion concentration versus time for different porous bed fractions (*b*)

The time of switch from emulsion flow to elution with water differ depended on which porous bed size was used. For bed with 90–150 μm – it was 710 s, while for 150–250 μm – 584 s and for 200–300 μm – 392 s. The time of change was also different for various bed lengths. Accordingly for 0.2 m it was 410 s, for 0.3 m the time equaled to 710 s and for 0.5 m – 1331 s.

The fraction size has direct impact on the size of free pores spaces. Therefore the emulsion flow is greatly influenced by this parameter, as it can be observed in Figure 3*a*. In case of bed with larger microspheres size, the flow resistance was smaller. Therefore, as it is presented in Figure 3*b* the significant drop of emulsion concentration was not observed in the first phase of experiment. Contrary, in case of porous bed with smaller diameter the situation was different. In this situation the flow resistance was higher, as can be seen in Figure 3*a*, and the retention mechanism was clearly observed, which can be concluded from concentration of emulsion drop observed in Figure 3*b*. From Figure 3*a* it can be also noted that the steady state was reached faster for the porous bed with larger fraction. It is true both for emulsion flow and its elution with water. This was caused by the fact that porous media with bigger fraction had less pores with sizes that were similar to the diameter of oil droplets in prepared emulsion. Therefore fewer spaces could be blocked by oil droplets.

The process of emulsion retention in porous structure depends also on the length of porous bed. To show how this parameter influences the emulsion flow and elution from porous media we conducted experiments with three tubes with different lengths. The results of experiment are presented in Figure 4*a* and Figure 4*b* for particle size range 90–150 μm.

In Figure 4*a* it is possible to observe that for the longer bed was used, the bigger flow resistance was noted. Time that was needed to reach steady state

was also dependent from this parameter. For every tube the time until steady state was reached varied. In case of shorter tubes, it means 0.2 m and 0.3 m the steady state was reached in shorter time, than for 0.5 m length bed. It was caused by the fact that in longer pipes there are more free pores that can be blocked by oil phase. Therefore the time of pores clogging is also longer, as can be seen from emulsion concentration drop in Figure 4*b* – for 0.5 m length the drop in emulsion concentration is observed after 300 s, while for 0.2 m after 150 s. During the process of elution with water the time until the steady state was reached was also dependent from porous bed length.

The analysis of porous bed permeability change during emulsion flow and elution

Knowing the pressure changes during the flow as well as certain parameters such as flow rate, porous bed length and its diameter, it was possible to determine permeability changes of bed in time of process of emulsion flow and elution. The graphs in Figure 5 present the changes in permeability of bed calculated according to the equation (1).

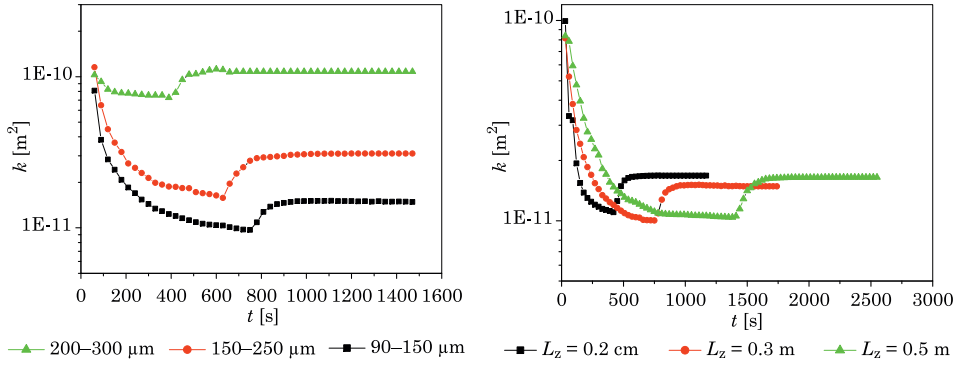

Fig. 5. Permeability change versus time for different porous bed fractions during experiment (Lz = 0.3 m) (*a*), permeability change versus time for different porous bed lengths – particle size range 90–150 µm (*b*)

As it is possible to observe from Figures 5*a* and 5*b* the permeability of porous bed decreases with time. This drop is dependent on the particle size range used in experiments. The smaller particle size were used the lower value of permeability is observed. This confirms the phenomena of oil droplets retention that is more intense in porous bed with smaller microspheres. However, for porous bed with different length the values of permeability at the end of emulsion flow

experiments are similar. The difference in this case is observed in terms of time that is needed to reach the steady state-as shown in Figure 5*b*.

During analysis of elution process it is possible to note the increase in permeability factor for all cases. Eventually during elution with water the constant value of permeability is reached. In order to better understand and extend the capability of understanding the phenomenon that occurred during experiments we decide to conduct experiments concerning the flow of water only through the porous bed with three particle size fractions. Then we calculate the value of permeability for the flow of water. The results are presented in Table 2.

Table 2

Permeability of porous bed used in experiments

Particle size [μm]	Permeability [m^2]		
	L_z = 0.2 m	L_z = 0.3 m	L_z = 0.5 m
90–150	$2.15 \cdot 10^{-11}$	$2.02 \cdot 10^{-11}$	$2.27 \cdot 10^{-11}$
150–250	–	$4.58 \cdot 10^{-11}$	–
200–300	–	$1.22 \cdot 10^{-10}$	–

Considering the data from Table 2 as well as Figure 5 it can be observed that permeability for water flow are higher than values of permeability for bed that was previously saturated with emulsion. This is true for every analyzed case in our experiment. Therefore it is possible to state that the phenomena of trapping of oil in porous bed occurred. In case of porous media with smaller microspheres, permeability for bed length of 0.3 m was smaller by 27% when comparing to permeability in experiment only with water (from value $2.02 \cdot 10^{-11}$ m^2 to $1.48 \cdot 10^{-11}$ m^2). Meanwhile for porous bed particle size range 200–300 μm the value of permeability decreased by only 11% (from $1.22 \cdot 10^{-10}$ m^2 to $1.08 \cdot 10^{-10}$ m^2). Regarding the influence of length of porous bed on oil retention mechanism it is possible to state that permeability of clean bed was 25% higher comparing to bed saturated previously with emulsion.

Conclusion

The conducted work delivered valuable experimental data that concern influence of parameters of porous bed on process of emulsion flow and elution. The work quantitatively determines the flow resistance during flow and concentration changes of fluid at the outlet from bed. The analysis of change in concentration in permeability of bed indicates the gradual change of permea-

bility that suggests the phenomena of oil retention inside the porous structure. After comparison of permeability for water flow that was previously saturated with emulsion, with the permeability for water flow through clean bed it was possible to determine the retention rate of oil phase in porous structure. The analysis of changes in emulsion concentration that leaved the bed showed that in the first phase of process the concentration of emulsion rapidly decreases. It was caused by retention of big droplets in porous structure. When all spaces where droplets can be trapped are filled, the flow takes place through the main paths of flow. This is the reason that concentration of effluent emulsion increase and ultimately reaches the original value.

Acknowledgment

The authors acknowledge the financial support provided by National Science Center through the Preludium program, Project number: 2013/05/N/ST8/03798.

References

Alvarado V., Romero M.I., Carvalho M.S. 2011. *Experiments and network model of flow of oil-water emulsion in porous media.* Physical Review E, 84(4).

Alvarado V., Márcio R.V.P.F., Carvalho S. 2013. *Emulsion flow model based on mobility control and displacement efficiency effects*. Mobility 22nd International Congress of Mechanical Engineering, Ribeirœo Preto, SP, Brazil, November 3–7.

Błaszczyk M., Sęk J., Przybysz Ł. 2016a. *Modelling and experimental study of pressure elution of high-viscosity substances with a low-viscosity liquid from granular bed*. Canadian Journal of Chemical Engineering, 94: 1548–1559.

Błaszczyk M., Sęk J., Przybysz Ł. 2016b. *Capillary bundle model for gravitational flow of emulsion through granular media and experimental validation.* Chemical Engineering Science, 155: 415–427, doi.org/10.1016/j.ces.2016.08.032.

Błaszczyk M., Sęk J., Pacholski P., Przybysz Ł. 2016c. *The analysis of emulsion structure changes during flow through porous structure.* Journal of Dispersion Science and Technology, in-press, DOI 10.1080/01932691.2016.1226184.

Cai J., Li C., Tang X., Ayello F., Richter S., Nesic S. 2012. *Experimental study of water wetting in oil-water two phase flow-Horizontal flow of model oil.* Chemical Engineering Science, (73): 334–344.

Cortis A., Ghezzehei A. 2007. *On the transport of emulsions in porous media.* Journal of Colloid and Interface Science, (313): 1–4.

Cobos S., Carvalho M.S., Alvarado V. 2009. *Flow of oil-water emulsions through a constricted capillary*. International Journal of Multiphase Flow, (35): 507–515.

Crawford S., Clifford J., David K., John W. 1997. *Effects of emulsion viscosity during surfactant enhanced soil flushing in porous media*. Journal of Soil Contamination, 64: 355–370.

Demikhova I.I., Likhanova N.V., Hernandez Perez J.R., Lopez Falcon D.A., Olivares-Xometl O., Montezuma Bertier A.E., Lijanova I.V. 2016. *Emulsion flooding for enhanced oil recovery: Filtration model and numerical simulation.* Journal of Petroleum Science and Engineering, (14): 235–244.

DULLIEN F.A.L. 1992. *Porous Media Fluid Transport and Pore Structure*. Academic Press Inc, San Diego, California.

GUILLEN V.R., GUILLEN M.S., CARVALHO V., ALVARADO V. 2012. *Pore Scale and Macroscopic Displacement Mechanisms in Emulsion Flooding.* Transport in Porous Media, 94: 197–206.

GUILLEN V.R., ROMERO M.I., CARVALHO M., ALVARADO V. 2012. *Capillary-driven mobility control in macro emulsion flow in porous media.* International Journal of Multiphase Flow, 43: 62–65.

HEINEMANN Z.E. 2005. *Fluid flow in porous media*. Textbook Series, 1, Leoben.

IDORENYIN E., SHIRIF E. 2012. *A new simulation model for two-phase flow in porous media.* Brazilian Journal of Petroleum and Gas, 6(1): 1–18.

KUMAR R., DAO E., MOHANTY K. 2012. *Heavy-Oil Recovery by In-Situ Emulsion Formation*. Society of Petroleum Engineers Journal, 17: 2, SPE-129914-PA

LANGEVIN D., POTEAU S., HENAUT I., ARGILLIER J. 2004. *Crude Oil Emulsion Properties and their Application to Heavy Oil Transportation.* Oil & Gas Science and Technology, 59(5): 511–521.

LEMARCHAND C., COUVREUR P., VAUTHIER C., COSTANTINI D., GREF R. 2003. *Study of emulsion stabilization by graft copolymers using the optical analyzer Turbiscan*. International Journal of Pharmacy, 254: 77–82.

LI J., GU Y. 2005. *Coalescence of oil-in-water emulsions in fibrous and granular beds.* Separation and Purification Technology, 42: 1–13.

MANDAL A., SAMANTA A., BERA A., OJHA K. 2010. *Role of oil-water emulsion in enhanced oil recovery*. International Conference on Chemistryand Chemical Engineering, number Iccce. August Session, p. 190–194.

MORADI M., KAZEMPOUR M., FRENCH J.T., ALVARADO V. 2014. *Dynamic flow response of crude oil-in-water emulsion during flow through porous media*. Fuel, 135: 38–45.

SĘK J., BŁASZCZYK M., DZIUBIŃSKI M, PADYK A. 2011. *The study of permeation process of model fluids and fluids formed from the processing of crude oil through porous medium.* Environmental Engineering Ecology and Technology, 26: 48–58.

THIELE E.S., FRENCH R.H. 1998. *Light-Scattering Properties of Representative, Morphological Rutile Titania Particles Using a Finite-Element Method*. Journal of American Ceramic Society, 81(3): 469–79.

WANG H.F. 2000. *Theory of Linear Poroelasticity with Applications to Geomechanics and Hydrogeology*. Princeton University Press, p. 4–17.

WANG J., DONG M. 2011. *Trapping of the non-wetting phase in an interacting triangular tube bundle model*. Chemical Engineering Science, 66: 250–259.

YOUNG-CHUL L., TAE-SOON K., JUNG-SEOK Y., JI-WON Y. 2007. *Remediation of groundwater contaminated with DNAPLs by biodegradable oil emulsion*. Journal of Hazardous Materials, 140: 340–345.

Technical Sciences, 2016, 19(4), 339–357

Quarterly peer-reviewed scientific journal
ISSN 1505-4675
e-ISSN 2083-4527
TECHNICAL SCIENCES
Homepage: www.uwm.edu.pl/techsci/

FLEXURAL BEHAVIOUR OF CONCRETE SLABS REINFORCED WITH FRP BARS IN EXPERIMENTS AND ACCORDING TO ACI 440.1R GUIDE

***Marcin Abramski*[1], *Piotr Korzeniowski*[2], *Witold Tisler*[3]**

[1] Department of Rail Transportation and Bridges
[2] Department of Concrete Structures
[3] Department of Geotechnics, Geology and Marine Civil Engineering
Faculty of Civil and Environmental Engineering
Gdansk University of Technology

Received 20 April 2016; Accepted 11 November 2016; Available online 21 November 2016

Key words: basalt fibres, carbon fibres, FRP reinforcement, reinforcement bar, concrete slab, experiment.

Abstract

The paper presents research conducted on two concrete slabs reinforced with the carbon composite bars and two other concrete slabs reinforced with basalt composite bars. The carbon bars were plain, while the basalt ones were ribbed. The slabs were experimentally investigated in the flexural state of effort with the concentrated forces applied. The results are compared with the analytical solution proposed in the guide ACI 440.1R-06 of the American Concrete Institute. The calculation procedures in respect of flexure, as well as deflection, as per ACI 440.1R-06, are presented, briefly explained and discussed in the paper. Some suggestions to revise the existing procedures are offered. The authors present and discuss the following results of their experimental investigation: the ultimate capacity of the slabs, their modes of failure, deflections and the strains in reinforcement.

Introduction

Using Fibre Reinforced Polymer (FRP) materials in concrete structures may be profitable for its durability. Apart from the high corrosion resistance there are other important advantages of FRP materials: magnetic neutrality

Correspondence: Marcin Abramski, Katedra Transportu Szynowego i Mostów, Politechnika Gdańska, ul. Narutowicza 11/12, 80-233 Gdańsk, phone: 58 347 18 38, e-mail: marcin.abramski@wilis.pg.gda.pl

and high tensile strength. Unfortunately, FRP have also its disadvantages in comparison to steel such as the fragility or the low elastic modulus which is (with the exception of carbon FRP) much lower than for steel. Moreover the FRP materials are not ductile at all: they do not yield but are elastic until the destruction. FRP materials are also anisotropic: they are strong to tension only in one direction. The behaviour of concrete reinforced with FRP reinforcement bars is different from a traditionally (i.e. with steel bars) reinforced structure. Application of this technology in construction requires from engineers a broadened knowledge on calculating load-carrying capacity of structures reinforced with FRP bars. This knowledge should be based on existing design standards.

The article presents research conducted on two concrete slabs reinforced with carbon composite bars and two other concrete slabs reinforced with basalt composite bars. The slabs were experimentally investigated in the flexural state of effort with concentrated forces applied.

One of the objectives of the experiments was to compare the behaviour of the slabs reinforced with the polymer bars made from the different fibres (basalt and carbon). The prices of the FRP bars are about seven times higher for the carbon composite than for the basalt composite. The authors preferred the ribbed bars as the reinforcement for the examined slabs. However the ribbed rods made from the carbon fibres were not available at the time. Consequently, the ribbed basalt bars and the plane carbon bars had to be used for the experiments.

The second objective was to compare the experimental load bearing capacity of the tested slabs with the analytical solution proposed in a guide (ACI 2006) of the American Concrete Institute.

State of the art

Flexural behaviour of concrete slabs reinforced with FRP bars is a very popular issue in recent years (SALAKAWY, KASSEM 2003), (GANGARAO et al. 2007). An intense research is carried out in China and Japan (SALAKAWY, KASSEM 2003) and in Europe (OSPINA and NANNI 2007), (EL-GHANDOUR et al. 2003). Experiments from the last few years show that FRP reinforcement bars have under some specific circumstances more advantages than traditional steel (SALAKAWY, KASSEM 2003).

As it is reported in the literature using FRP reinforcement instead of steel usually increases load capacity of a concrete slab. That is caused mainly due to high tensile strength of the FRP reinforcement. This fact is a very important argument for applying the alternative type of reinforcement. Using the same

amount of reinforcement a higher flexural strength (even up to 100%) can be obtained (SALAKAWY, KASSEM 2003). However, numerous differences between steel and FRP materials must be taken into account. Linear-elastic behaviour of FRP until failure, low ductility and lower elastic modulus than steel (with the exception of the carbon FRP) cause that load-carrying capacity of the concrete slab differs substantially. Concrete slab reinforced with steel bars usually achieves yield strength before rupture and failure is not rapid. Concrete slab reinforced with FRP bars are characterized by a different destruction mode: usually concrete crushing or rarely reinforcement rupture. The both failure modes are rapid.

The basalt FRP are an interesting alternative for the better known and wider spread carbon or glass FRP. In addition to good mechanical properties, basalt has a high chemical and thermal stability, good thermal insulating, electrical and sound properties. Basalt fibres are also significantly better chemically resistant than glass fibres, particularly in a strongly alkaline environment. For example, corrosive liquids and gases can be transported with pipes made of basalt composite (URBAŃSKI et al. 2013), (VAN DE VELDE et al. 2002).

The authors of the paper decided to program their experimental research based on the Guide for the Design and Construction of Structural Concrete Reinforced with FRP Bars (ACI 2006) published by the American Concrete Institute. Computations of a cross section strength according to that document should be based on the following assumptions:

– perfect bond exists between concrete and FRP reinforcement,

– the tensile behaviour of the FRP reinforcement is linearly elastic until failure,

– the tensile strength of concrete is ignored,

– the maximum usable compressive strain in the concrete is assumed to be 0,003,

– strain in the concrete and in the FRP reinforcement is proportional to the distance from the neutral axis.

Calculation procedures proposed by ACI 440.1R-06

Flexure

The strength design philosophy states that the design flexural capacity $\phi \cdot M_n$ must exceed the factored acting bending moment M_u:

$$\phi \cdot M_n \geq M_u \tag{1}$$

where:
M_n – nominal moment capacity,
M_u – factored moment at section,
ϕ – strength reduction factor.

The design flexural strength is calculated as nominal flexural strength M_n multiplied by a strength reduction factor ϕ. The nominal flexural strength is determined based on strain compatibility, internal force equilibrium and the controlled mode of failure.

In the beginning of the procedure a mode of failure has to be determined. A reinforcement ratio (Eq-2) has to be assumed and compared to the balanced reinforcement ratio (Eq-3). Comparison of these two values determine the failure mode. As it was mentioned above, FRP reinforcement does not yield, so balanced ratio is computed using design tensile strength:

$$\rho_f = \frac{A_f}{b \cdot d} \tag{2}$$

$$\phi_{fb} = 0.85 \cdot \beta_1 \cdot \frac{f_c'}{f_{fu}} \cdot \frac{E_f \cdot \varepsilon_{cu}}{E_f \cdot \varepsilon_{cu} + f_{fu}} \tag{3}$$

where:
ρ_f – FRP reinforcement ratio,
A_f – area of FRP reinforcement,
b – width of rectangular section,
d – distance from extreme compression fiber to centroid of tension reinforcement,
ρ_{fb} – FRP reinforcement ratio producing balanced strain conditions,
β_1 – factor reducing the real depth of the section, taken as 0.85 for concrete strength f_c' up to and including 4000 psi (28 MPa),
f_c' – specified compressive strength of concrete,
f_{fu} – design tensile strength of FRP, considering reductions for service environment,
E_f – design modulus of elasticity of FRP,
ε_{cu} – ultimate strain in concrete.

If the balanced ratio is bigger than reinforcement ratio ($\rho_{fb} > \rho_f$), the concrete crushing must be obtained. Otherwise, reinforcement rupture governs. In the following paragraph the case of concrete crushing is considered.

Based on the equilibrium of forces and strain compatibility (Fig. 1), it can be written as follows:

$$M_n = A_f \cdot f_f \cdot \left(d - \frac{a}{2}\right) \tag{4}$$

$$a = \frac{A_f \cdot f_f}{0.85 \cdot f_c' \cdot b} \tag{5}$$

$$f_f = E_f \cdot \varepsilon_{cu} \cdot \frac{\beta_1 \cdot d - a}{a} \tag{6}$$

where:
f_f – stress in FRP reinforcement in tension,
a – depth of equivalent rectangular stress block, equal $\beta_1 \cdot c$.

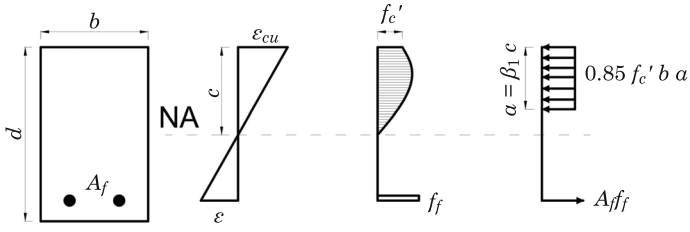

Fig. 1. Strain and stress distribution at ultimate conditions
Source: ACI (2006).

Substituting value a from equation (5) into equation (6), it can be obtained:

$$f_f = \left(\sqrt{\frac{(E_f \cdot \varepsilon_{cu})^2}{4} + 0.85 \cdot \beta_1 \cdot \frac{f_c'}{\rho_f} \cdot E_f \cdot \varepsilon_{cu}} - 0.5 \cdot E_f \cdot \varepsilon_{cu}\right) \leq f_{fu} \tag{7}$$

Nominal flexural strength is defined above. The FRP reinforcement is linearly elastic up to failure, so result of equation (7) must be less than f_{fu} (design tensile strength). This model of failure (concrete crushing) is recommended to design.

If $\rho_f < \rho_{fb}$ the failure mode is reinforcement rupture and maximum strain in concrete (0.003) may not be attained. The calculation procedure is other than for concrete crushing failure mode. Analysis has two unknown values: com-

pressive strain ε_c in concrete at failure and the depth to neutral axis c. Nominal flexural strength can be computed using equation (8):

$$M_n = A_f \cdot f_{fu} \cdot \left(d - \frac{\beta_1 \cdot c}{2}\right) \tag{8}$$

where:
c – distance from extreme compression fibre to the neutral axis.

For a given section the product of $\beta_1 \cdot c$ in equation above depends on material properties and FRP reinforcement ratio. The maximum value is obtained when maximum concrete strain (0.003) is attained. A simplified calculation of nominal strength is based on these two equations:

$$M_n = A_f \cdot f_{fu} \cdot \left(d - \frac{\beta_1 \cdot c_b}{2}\right) \tag{9}$$

$$c_b = \frac{\varepsilon_{cu}}{\varepsilon_{cu} + \varepsilon_{fu}} \cdot d \tag{10}$$

where:
c_b – distance from extreme compression fibre to centroid of tension reinforcement,
ε_{fu} – design rupture strain of FRP reinforcement.

Because FRP bars are not characterized by a ductile behaviour, a strength reduction factor must be used to provide a higher reserve of strength in a designed structural member. The strength reduction factor ϕ for compression controlled failure is 0.65 in recommendation (ACI 2006). The member constructed for concrete crushing may not fail accordingly. For instance, if the concrete strength is higher than specified, a member failure mode may be a FRP rupture. This is the main reason for creating a relationship between two values of factor ϕ. A section controlled by a concrete crushing is defined as a section in which $\rho_f > 1.4 \cdot \rho_{fb}$ and a section with FRP rupture is defined by $\rho_f > \rho_{fb}$. Strength reduction factor can be computed using equation (11):

$$\phi = \left\{ \begin{array}{c} 0.55 \text{ for } \rho_f < \rho_{fb} \\ 0.3 + 0.25 \cdot \dfrac{\rho_f}{\rho_{fb}} \text{ for } \rho_{fb} \le \rho_f < 1.4 \cdot \rho_{fb} \\ 0.65 \text{ for } \rho_f \ge 1.4 \cdot \rho_{fb} \end{array} \right\} \tag{11}$$

A relation between strength reduction factor and reinforcement ratio is presented on Fig. 2. There is a linear transition between factors 0.55 and 0.65.

If a member is designed to fail by FRP rupture, a minimum amount of reinforcement should be obtained ($\phi \cdot M_n \geq M_{cr}$). Provisions are based on ACI 318-14 (American Concrete Institute 2014). To compute a minimal amount of reinforcement eq. (12) can be used.

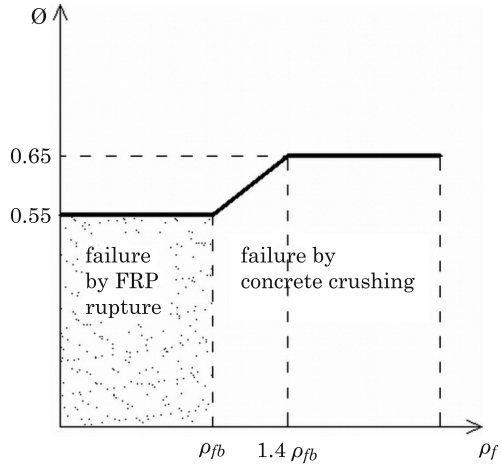

Fig. 2. Strength reduction factor as a function of the reinforcement ratio
Source: ACI (2006).

$$A_{f,\min} = \frac{4.9 \cdot \sqrt{f_c'}}{f_{fu}} \cdot b_w \cdot d \geq \frac{330}{f_{fu}} \cdot b_w \cdot d \tag{12}$$

where:

$A_{f,\min}$ – minimum area of FRP reinforcement needed to prevent a failure of flexural member upon cracking,

b_w – width of the web.

If a failure mode is concrete crushing ($\rho_{fb} > \rho_f$) the minimum amount of reinforcement is automatically achieved. Therefore, eq. (12) can be used only if failure mode is controlled by FRP rupture.

Deflection

Calculating the short term deflection in the ACI Report (ACI 2006) is based on the effective moment of inertia. Taking into consideration the differences in stiffness and bond characteristic between steel and FRP, an effective moment of inertia is computed using the following equation:

$$I_e = \left(\frac{M_{cr}}{M_a}\right)^3 \cdot I_g \cdot \beta_d + \left[1 - \left(\frac{M_{cr}}{M_a}\right)^3\right] \cdot I_{cr} \leq I_g \tag{13}$$

where:
I_e – effective moment of inertia,
β_d – reduction coefficient used in calculating deflection,
M_{cr} and M_a – cracking and applied moment, respectively,
I_{cr} and I_g – cracked and gross moment of inertia of concrete section, respectively.

The most important factor in this equation is β_d which reduces the stiffness of FRP bars. In the next to last revision of ACI (ACI 2003) this coefficient was based on the proportion of the FRP and steel elastic moduli:

$$\beta_d = 0.5 \cdot \left(\frac{E_{\text{FRP}}}{E_s} + 1\right) \tag{14}$$

where:
E_{FRP} – modulus of elasticity of FRP.

However effective moment of inertia I_e calculated with use of the equations (13) and (14) resulted in obtaining too low values of deflection. Therefore coefficient β_d required some new considerations. The newer evaluation of FRP RC test data, based on (YOST et al. 2003), leads to the following proposal:

$$\beta_d = \frac{1}{5} \cdot \frac{\rho_f}{\rho_{fb}} \leq 1 \tag{15}$$

Based on the value of effective moment of inertia a deflection of a simply supported beam can be computed using the following equation:

$$\Delta = \frac{5}{48} \cdot \frac{M \cdot l^2}{E_c \cdot I_e} \tag{16}$$

where:
Δ – deflection due to sustained loads,
M – maximum bending moment,
l – span length,
E_c – modulus of elasticity of concrete.

Analysing the two β_d approaches two values of deflection can be obtained, one with coefficient used in the previous guide (ACI 2003) and second – in the current one (ACI 2006). The authors performed a comparative analysis of the both approaches (Tab. 1). Material characteristics of concrete, amount of

reinforcement and the applied moment (which was assumed as equal to 20 kNm) are the same for all cases. Moduli of elasticity and ultimate tensile strengths of reinforcement are taken from the report (ACI 2006).

Table 1

Comparison of different approaches to calculating β_d coefficient

Type of reinforcement	Modulus of elasticity E_f [GPa]	Ultimate tensile strength f_{fu} [MPa]	Coefficient (eq. 15) β_1 [–]	Coefficient (eq. 14) β_2 [–]	Moment of inertia (eq. 13) I_{e1} mm^4	Moment of inertia (eq. 13) I_{e2} mm^4	Deflection (eq. 16) Δ_1 mm	Deflection (eq. 16) Δ_2 mm
GFRP	41.4	552	0.262	1.530	$2.99 \cdot 10^6$	$3.2 \cdot 10^6$	53.1	49.58
AFRP	82.7	1172	0.584	2.568	$5.46 \cdot 10^6$	$5.79 \cdot 10^6$	29.04	27.38
CFRP	152	2070	1.000	4.300	$9.0 \cdot 10^6$	$9.55 \cdot 10^6$	17.62	16.61

Authors' experimental investigation

Four slabs were experimentally investigated. Two slabs were reinforced with basalt FRP bars and two other with carbon FRP bars. The slabs were 360 cm long × 90 cm wide × 8 cm thick and had two spans, both 160 cm long (Fig. 3).

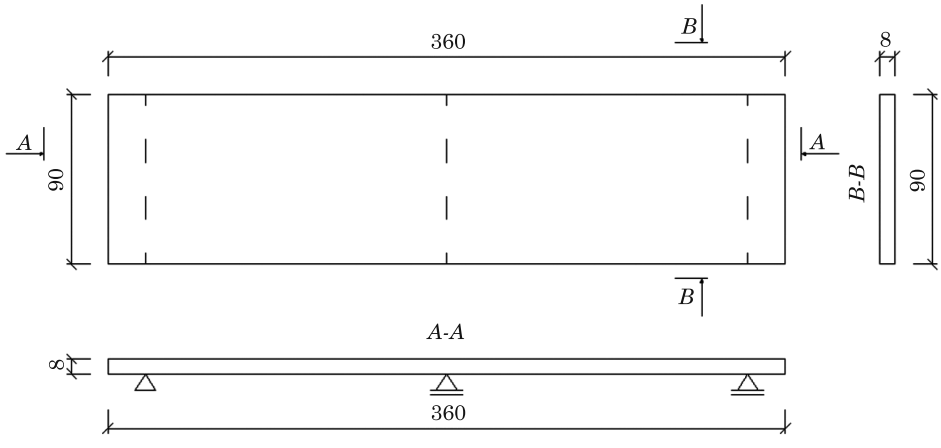

Fig. 3. Dimensions of the investigated slabs

Test specimens and material properties

The diameters of the both bar types were equal to 8 mm. The basalt bars were ribbed while the carbon bars were plane (as mentioned beforehand, the ribbed carbon bars were unavailable). The ribs in the basalt bars were made by

winding the additional basalt yarn around the previously prepared plane bars, see Figure 4.

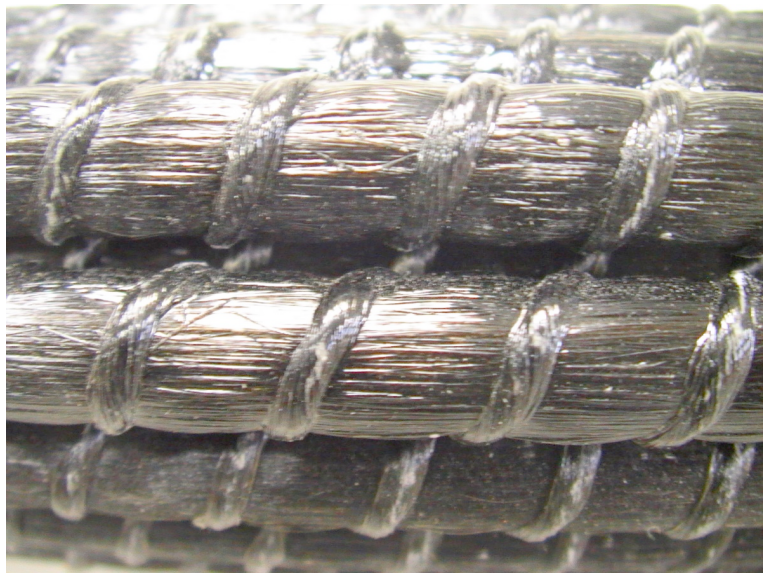

Fig. 4. Detail of basalt FRP bars

Parameters of the slabs and concrete are presented in Table 2.

An amount of reinforcement was the same in all investigated slabs. The reinforcement ratio was bigger than the balanced ratio ρ_{fb}. The expected mode of failure was mostly the concrete crushing. Configuration of the reinforcement was a little different in the both slab types (Tab. 3, Fig. 6). For all the slabs concrete cover was 1.5 cm both at the top and the bottom. The material characteristics declared by suppliers were similar for the both bar types. An important difference was a surface of the bars. The basalt bars were ribbed on their entire length and the carbon bars were plain. This fact influenced the experiments results very much.

Table 2

Material characteristics

Bar type		Reinforcement (according to supplier data)		Concrete (according to results of the own tests)	
		tensile strength [MPa]	elastic modulus [GPa]	compressive strength [MPa]	elastic modulus [GPa]
Basalt FRP	B-1	1100	90	37.88	34.98
	B-2	1100	90	37.88	34.98
Carbon FRP	C-1	1280	98	34.78	36.60
	C-2	1280	98	35.70	37.40

Table 3

Details of slab reinforcement at their bottom and top sides

SLAB		ρ_f [%]	ρ_{fb} [%]	ρ_f/ρ_{fb} [%]	Bars positioning			
					number on top	length [cm] in the both sides from the central support	number at the bottom	length
BASALT	B-1	0.94	0.73	1.29	11	50	11	whole slab
	B-2	0.94	0.73	1.29	11	40	11	whole slab
CARBON	C-1	0.94	0.55	1.73	11	100	11	whole slab
	C-2	0.94	0.56	1.69	11	100	11	whole slab

Test set-up

The slabs were loaded by two equal concentrated forces (Fig. 5). The load was controlled by displacement.

Fifteen strain gauges were installed on each slab, 9 on the top reinforcement and 6 in bottom reinforcement (Fig. 6). Arrangement of strain gauges at the top reinforcement was intentionally asymmetrical towards an axis of the middle support. The distance between the axis and the strain gauges in the left span was L/3 (where L was 1.6 m – span length). At the right span this distance was equal to L/4.

Two indicators were used to measure a deflection of the slab. The indicators were installed at one edge of the slab, directly underneath the points, were two concentrated forces acted. The accuracy of the measurement was equal to 0,01 mm. The left span of the slab has been marked as the *W* (the point of the compass) and the right one as *E*.

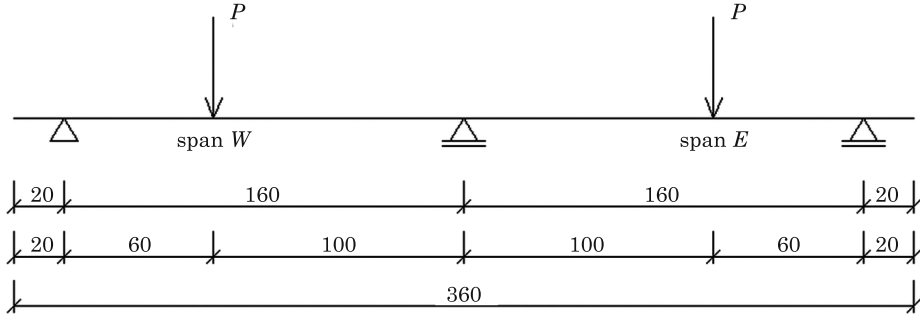

Fig. 5. Static scheme of experimental set-up

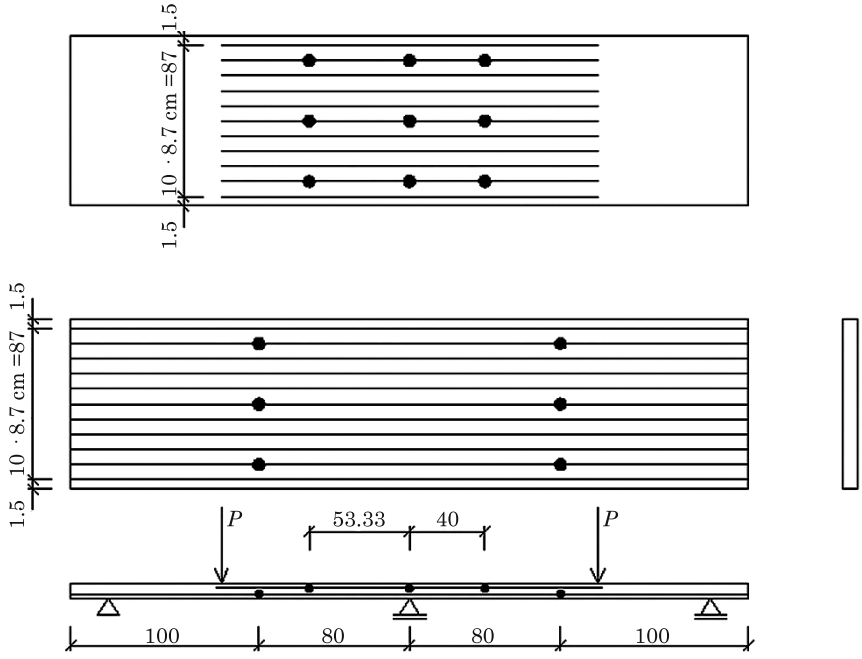

Fig. 6. Location of strain gauges

Test results and discussion

Ultimate capacity and mode of failure

The amount of reinforcement was the same in every investigated slab. The calculation based on a procedure proposed by ACI guide (ACI 2006) brought a concrete crushing as an expected failure mode, because reinforcement ratio ρ_f was 1.78 times higher than balanced reinforcement ratio ρ_{fb}.

In the case of the slabs reinforced with the basalt bars the failure mode was as expected, the same as in the over-reinforced slabs with the steel reinforcement, see Figure 7.

Unexpectedly, the failure mode of slabs reinforced with carbon bars was definitely different. The most probable reason for that was a weak bond between concrete and bars. As a result, the obtained load-carrying capacities of the slabs C-1 and C-2 were significantly lower than expected and reached 40% of the calculated value, i.e. 90 kN (see Tab. 4). Three splits were formed: one in the symmetry axis of the elements and two under the point loads (Fig. 8). All the splits developed before the destruction of the slabs. The reason for the premature failure must have been slip of reinforcement bars in concrete. The

Fig. 7. Slab B-2 shortly before its failure

carbon bars were plain, while the basalt ones were ribbed. The slip hypothesis was confirmed by the behaviour of the longitudinal reinforcement bars. They were not covered by concrete at the slab face and were visible on two face surfaces of the slab before the test beginning. When the experiments were over, the bars were visible too, but they were pulled about 1 cm into the slab (Fig. 9).

Table 4

Comparison of test results with code predictions

Type of reinforcement		Experimental failure load [kN]	Theoretical flexural capacity [kN]	Experimental/ Theoretical [–]	Experimental/ Theoretical with strength reduction factor (0.65) [–]	Mode of failure
BASALT	B-1	70	91.46	0.765	1.17	CC
	B-2	65	91.46	0.71	1.10	CC
CARBON	C-1	35	89.36	0.39	0.60	SF
	C-2	38	90.86	0.42	0.64	SF

Note: CC – failure obtained by the concrete crushing
SF – failure obtained by the reinforcement slip in concrete.

Fig. 8. Mode of failure slabs C-1 and C-2

Fig. 9. Detail of slab C-2 after its failure

In the Table 4 the predicted values of load-carrying capacities of the tested slabs are compared with the experimental results. The predicted values were computed based on the calculation procedures presented in the chapter 3. The strength reduction factor ϕ was taken into account according to the equation (11). It is worth noting that in the case of the slabs reinforced with the carbon plain bars the predicted load-bearing capacity is much overestimated in comparison to the experimental one. Such a difference is not acceptable. In the case of the slabs reinforced with the ribbed basalt bars the

load-bearing capacity obtained from the experiments is much lower than the theoretical value, but when the strength reduction factor ϕ is used, the consistency between experimental and theoretical load-bearing capacity is quite good (does not exceed 17%).

The obtained difference in the load-carrying capacities of the both slab types was equal up to 50% (Fig. 10).

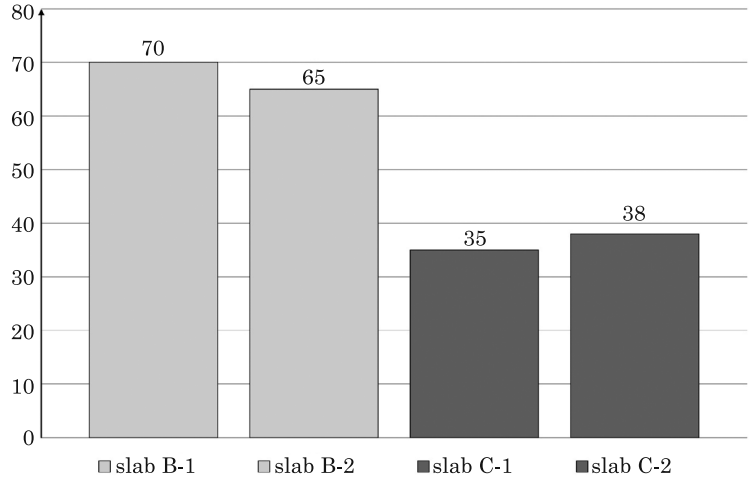

Fig. 10. Load-carrying capacities in [kN] of the tested slabs

Deflection

The load versus deflection diagrams for all the tested slabs are presented in Figure 11. The deflection was taken as the mean value from the both spans. All the slabs reached deflection of about 4 cm. The cracking bending moment was observed for all the slabs at the load level 15 kN.

The load-deflection curves obtained for the slabs reinforced with bars made of basalt composite (B-1 and B-2) differ considerably from the curves obtained for the slabs reinforced with bars made of carbon composite (C-1 and C-2). The first two curves are almost bilinear: they consist of two almost straight sections: before cracking and after cracking up to failure. In case of the slabs C-1 and C-2 the second section of the curve becomes flat shortly before reaching the maximum load level. The reason of such a behaviour must be a slip of plain carbon bars in concrete.

None of experimental curves coincide in the stage after cracking with a development of deflection obtained analytically according to (ACI 2006). The deflections obtained analytically are too small in comparison to experimental

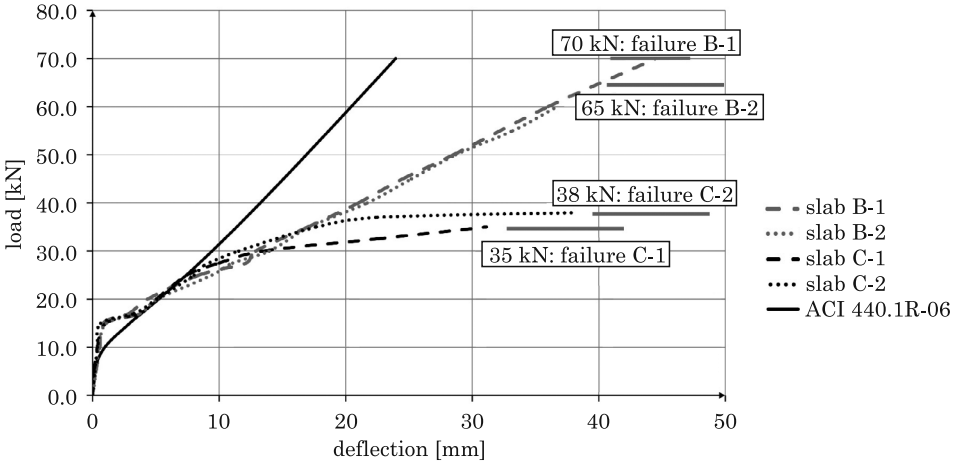

Fig. 11. Load versus deflection diagrams obtained in four experiments and in an analysis performed according to (ACI 2006)

data. The reason of this inconsistency is factor β_d (Eq. 15). According to the last version of the guidelines (ACI 2006) this factor depends on the balanced reinforcement ratio ρ_{fb}. This ratio is influenced by the ultimate tensile strength f_{fu} (Eq. 3). It means that deflection could be different for elements which have the same stiffness but different ultimate strength, which is incorrect. This remark was noticed already in (EL-GHANDOUR et al. 2003) and was recommended to consider in the next revision of the guidelines (ACI 2006).

According to the previous version of (ACI 2006) the factor β_d was computed according to equation (14), which was giving much higher values. The application of that approach leads to increasing effective moment of inertia I_e and would in effect result in even lower deflections that obtained from equation (15). It confirms, that the changes made in the last revision of the guidelines (ACI 2006) were needed.

Strains in reinforcement

Figures 12 and 13 present strain development in the reinforcement bars under the concentrated loads (Fig. 12) and in the symmetry axis of the slab (Fig. 13) versus the applied load. The graphs made for the slabs with basalt reinforcement do not present the full range of loading the slabs because of local damages of strain gauges. The damages occurred by strain level of about 6%.

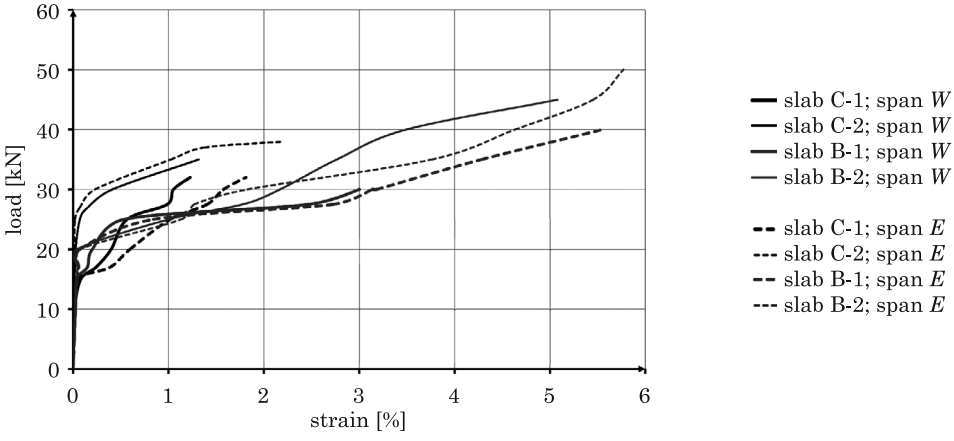

Fig. 12. Comparison of strain development in all the tested slabs in the both spans: *W* and *E*

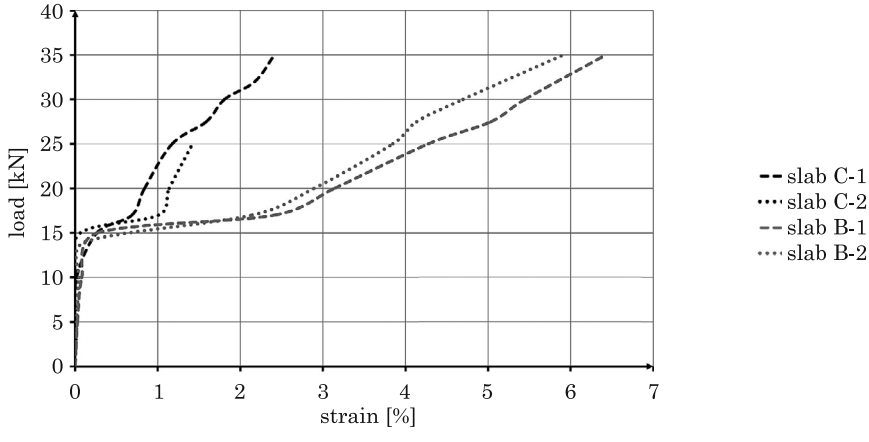

Fig. 13. Comparison of strain development in the symmetry axis of the slab (i.e. over the middle support)

If properly anchored, the both basalt and carbon bars would have been deformed longitudinally to the same extent up to load level P = 30 kN, as the deflection development up to that load level was very similar for all the tested slabs (see Fig. 11). However, the strain development in carbon bars was slow in comparison to basalt bars. Therefore, the reinforcement bars made of carbon composite were significantly less effective. In case of the slab C-2 the lower effectiveness was observed since the cracking load (P = 15 kN) up to failure (P = 38 kN). In case of the slab C1 it was observed also since the cracking load (P = 15 kN) for the support bars and since the load level about P = 25 kN for the bars of the both spans. The strain development presented in the both diagrams confirms the slip of carbon bars in concrete.

Conclusions

As mentioned beforehand the objective of the authors' investigations was to compare the behaviour of the concrete slabs reinforced with the basalt and carbon bars, whereas it turned out that the crucial problem was not in the material of the fibres but in the bond between the concrete and the polymer bars. Load-carrying capacity of slabs reinforced with ribbed bars is definitely higher than capacity of slabs reinforced with plain ones, although the strength as well as the modulus of the elasticity were higher for the plain carbon bars than for the ribbed basalt ones. In the presented experimental investigation the difference was equal to 50%. The plain bars (in the presented investigation made of a carbon composite) cannot be properly anchored in concrete and are not effective in sustaining bending moments. The problem of the bond between the concrete and the bar seems to be crucial when using the polymer bars as a reinforcement of the concrete structures. The surface of the plain polymer bars should be made rough, for instance by coating it with special adhesive and sand. The American guidelines (ACI 2006) address this problem just in an outline. Thus, the calculation procedures proposed by this guide is not useful if a bond between FRP reinforcement and concrete is too weak, like in the case of plain bars. In such a case the flexural failure mode differs much from the mode assumed in the theory of reinforced concrete structures.

In case of slabs reinforced with ribbed bars (in the presented investigation made of a basalt composite) the load-carrying capacity calculated according to (ACI 2006) is more consistent with the experimental results. However, deflections obtained from the calculation procedure underestimate the values obtained in the experiments. The problem was reported in the literature (EL-GHANDOUR et al. 2003) and should be considered in the next revision of the guidelines.

Acknowledgement

The research was co-financed by the European Union from the European Regional Development Fund (85%) and by Polish Ministry of Regional Development (15%) as part of operational programme "Innovative Economy". The project was called "Innovative means and effective methods to improve safety and durability of buildings and transport infrastructure in a sustainable development strategy" and was run by Technical University of Lodz, Poland. The authors of this paper carried out Task No. 018818. This support is greatly acknowledged.

References

ACI. 2003. *Guide for the Design and Construction of Concrete Reinforced with FRP Bars*. ACI 440.1R-03.

ACI. 2006. *Guide for the Design and Construction of Structural Concrete Reinforced with FRP Bars*. ACI 440.1R-06.

American Concrete Institute. 2014. *Building code requirements for structural concrete and commentary*. ACI 318-14, p.525.

EL-GHANDOUR A.W., PILAKOUTAS K., WALDRON P. 2003. *Punching Shear Behavior of FRP RC Flat Slabs* Part 1: *Experimental Study*. Journal of Composites for Construction, 7(3): 258–265.

GANGARAO H.V.S., TALY N., VIJAY P.V. 2007. *Reinforced Concrete Design with FRP Composites*. Boca Raton, Florida, USA: CRC Press.

OSPINA C.E., NANNI A. 2007. *Current FRP-reinforced concrete design trends in ACI 440.1 R*. Proceedings of the 8th International Symposium on Fiber Reinforced Polymer Reinforcement for Concrete Structures – FRPRCS-8. Patras, Greece, pp. 14–6.

EL-SALAKAWY E., KASSEM C., BENMOKRANE B. 2003. *Flexural behaviour of bridge deck slabs reinforced with FRP composite bars*. Proc., 6th International Symposium on FRP Reinforcement for Concrete Structures. Singapore. Singapore: World Scientific Publishing, pp. 1291–1300.

URBAŃSKI M., ŁAPKO A., GARBACZ A. 2013. *Investigation on concrete beams reinforced with basalt rebars as an effective alternative of conventional R/C structures*. 11th International Conference on Modern Building Materials, Structures and Techniques. Vilnius, Lithuania, pp. 1183–1191.

VELDE VAN DE K., KIEKENS P., VAN LANGENHOVE L., CATER S. 2002. *Basalt fibers as reinforcement for composites.* Editorial, International Composites News.

YOST J.R., GROSS S.P., DINEHART D.W. 2003. *Effective Moment of Inertia for Glass Fiber-Reinforced Polymer-Reinforced Concrete Beams*. ACI Structural Journal, 100(6): 732–739.

Technical Sciences, 2016, 19(4), 359–366

Quarterly peer-reviewed scientific journal
ISSN 1505-4675
e-ISSN 2083-4527
TECHNICAL SCIENCES
Homepage: www.uwm.edu.pl/techsci/

THERMAL ANALYSIS OF ALUMINUM BRONZE BA1032

Tomasz Chrostek

Department of Materials and Machine Technology
University of Warmia and Mazury in Olsztyn, Poland

Received 8 February 2016, accepted 18 November 2016, available online 21 November 2016.

K e y w o r d s: thermal analysis, DSC, differential scanning calorimetry, BA1032, CuAl10Fe3Mn2.

A b s t r a c t

In this study, aluminum bronze BA1032 was analyzed thermally by differential scanning calorimetry (DSC). The article presents the results of measurements of phase transitions occurring in aluminum bronze at a temperature of up to 600°C. Thermal analyses were conducted at constant heating rates of 5°C/min, 10°C/min and 15°C/min.

Introduction

Aluminum bronzes increasingly often replace tin bronzes due to their unique properties. Alloys containing up to 11% Al are suitable for industrial applications. Aluminum bronzes with 4–8% Al content can undergo both cold and hot forming, whereas alloys containing 9–11% are used for casting or are hot forged at a temperature of 870°C. Most aluminum bronzes are enriched with Fe and Ni to increase their strength. Aluminum bronzes are characterized by high tensile strength R_m of around 400–600 MPa as well as high corrosion resistance, and they are used in the production of vessel propellers, pump parts, machinery for paper and chemical industries, sheet metal, pipes, gears and wire. Aluminum bronzes with approximately 10% Al content can be hardened due to the presence of eutectoid transformations in the Cu-Al system

Correspondence: Tomasz Chrostek, Katedra Technologii Materiałów i Maszyn, Uniwersytet Warmińsko-Mazurski, ul. Oczapowskiego 11/E27, 10-719 Olsztyn, phone: 89 523 38 55, e-mail: tomasz.chrostek@uwm.edu.pl

at a temperature of 565°C and eutectoid at 11.8% Al. Alloys hardened in water at a temperature of approximately 900°C are tempered at 400–600°C for 2-3 hours. The hardness of quenched CuAl10 is estimated at 180 HB and at around 160 HB after tempering at 500°C (GÓRNY et al. 2003, ROMANKIEWICZ, ROMANKIEWICZ 2007).

Aluminum-iron-manganese bronze BA1032 (CuAl10Fe3Mn2 according to PN-EN 12163:2011) has high corrosion resistance and impact strength. The analyzed alloy is characterized by exceptional resistance to static loading, wear and high temperature, as well as satisfactory fluidity. It is used in the production of machines, engines and parts (rollers, sleeves) exposed to very high mechanical load, corrosion (in particular in acidic solutions) and wear. The BA1032 alloy is also suitable for the production of bars, flats, custom sheet metal and machine parts designed for operation in sea water. The analyzed material has estimated hardness of 120 HB (WIERZBICKA 2000).

Thermal analysis involves a series of methods for determining selected physical properties of a substance across a temperature gradient under a controlled temperature program. Processes that accompany changes in the temperature of various substances are investigated with the involvement thermoanalytical techniques. Differential scanning calorimetry (DSC) is one of such methods, and it is increasingly often used in various areas of science, including in metallurgy. This method is highly useful for measuring phase transition temperature and the amount of heat involved in those processes. Phase transitions structures are already known for the balance of Cu-Al, but there is little information on the phase transformations occurring in aluminum bronze BA1032. Additions of other elements present in the alloy may cause changes in the course of phase transitions (FRĄCZYK, BRECZKO 2010, SECKO, RÓŻAŃSKI 2011, SZUMERA 2012, 2013).

Materials and Methods

Aluminum bronze was tested by dynamic thermal analysis which involves a linear increase and decrease in temperature. The applied method is a fast analytical technique. Analyses were conducted in the DSC Phoenix 204 F1 differential scanning calorimeter (Netzsch) which measures the energy required to establish a zero temperature difference between the analyzed sample and a reference sample. The measured parameter is free heat flow.

Alloy samples weighing 74.92–76.33 mg were placed in aluminum crucibles. Crucibles should have similar weight, and in this experiment, their weight ranged from 39.64 to 40.38 mg. Thermal parameters were measured during heating to a temperature of 600°C at heating rates of 5, 10 and 15°C/min (FRĄCZYK, BRECZKO 2010, SUCHOŃ, JURA 2003).

Results and Discussion

Before the analysis, DSC curves were adjusted with the use of the "DSC Horizontal On" function. This operation was performed to bring the area under the curve where no reactions took place to zero. Adjusted calorimetric curves for BA1032 at heating rates of 5, 10 and 15°C/min are presented in Figure 1.

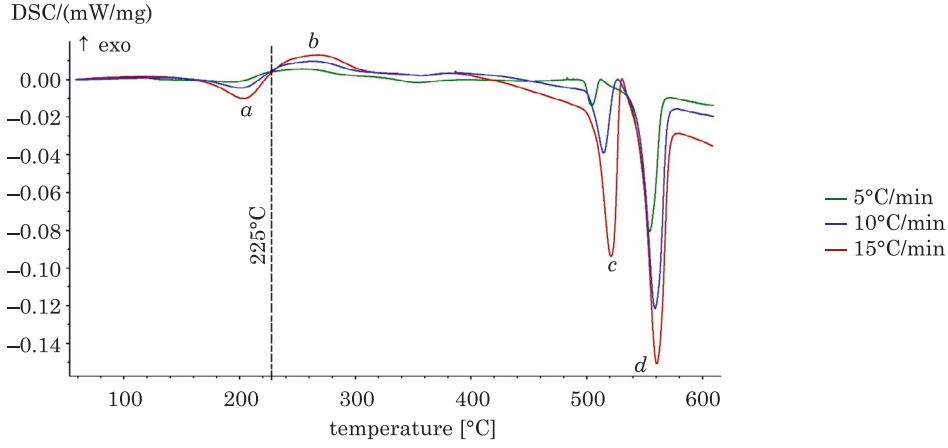

Fig. 1. DSC curves for BA1032 illustrating processes taking place at a temperature of up to 600°C

Information about the exchange of heat between the sample and its environment at different temperatures (T) can be read from a DSC curve. If the DSC curve is a straight (horizontal) line, there are no reactions at a given temperature. Four phase transitions, marked a, b, c and d, can be observed in Figure 1 at a temperature of approximately 205°C, 265°C, 515°C and 560°C (peak maxima), for different heating rates.

The first two peaks, a and b, have low enthalpy which becomes more visible only at a heating rate of 15°C/min. At a temperature of about 205°C reaches the endothermic phase transitions. At a temperature of about 267°C follow on an exothermic phase transition. Figure 2 shows the phase transitions of the peaks a and b at heating rate 15°C/min.

At a heating rate of 10°C/min and 15°C/min, a minor endothermic effect was noted between peaks b and c beginning from the temperature of around 390°C.

The last two transitions, c and d, have well-defined peaks, but their enthalpy is also relatively low. Peaks c and d, the onset and end of phase transitions, and the enthalpy of each peak at heating rates of 5, 10 and 15°C/min are shown in Figures 3, 4 and 5. Peak maxima denoting the temperatures at which the reaction takes place at the highest rate are also marked.

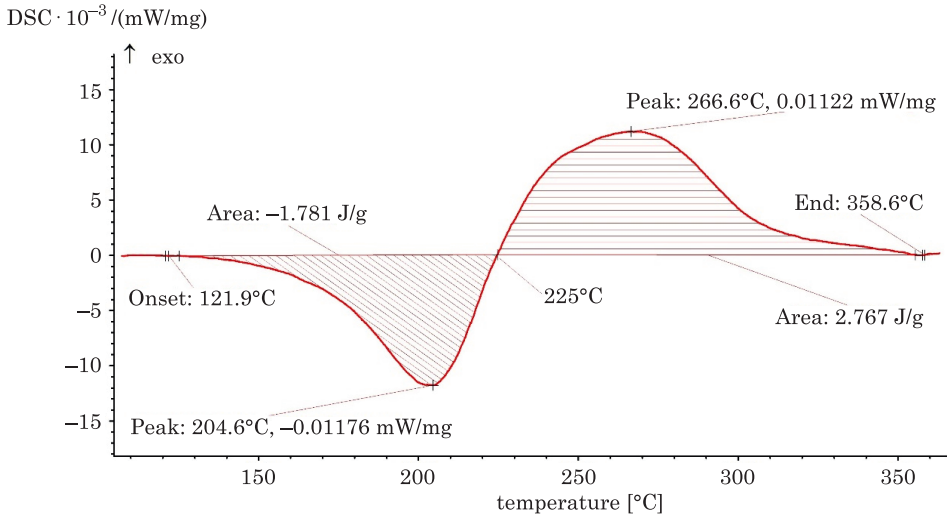

Fig. 2. DSC curves for BA1032 presenting the main reactions taking place at peak *a* and *b* and a heating rate of 15°C/min

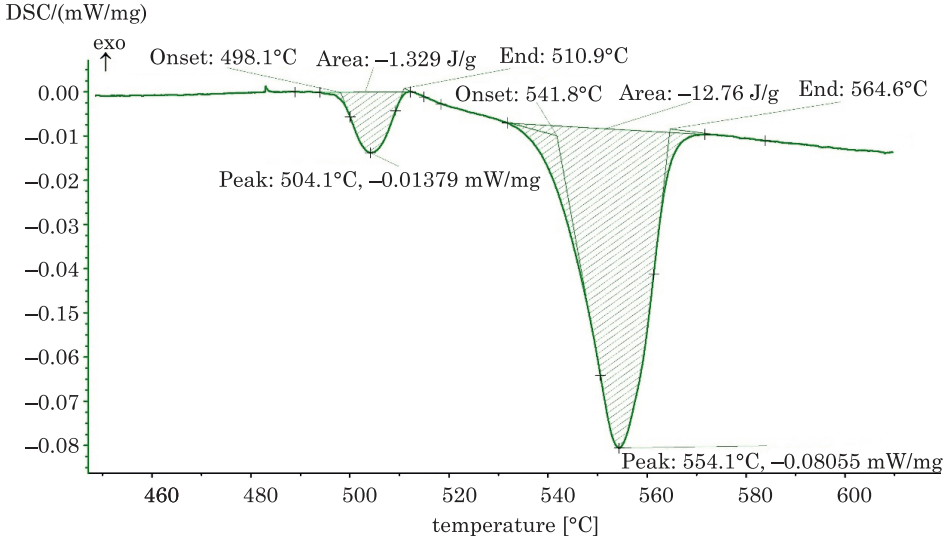

Fig. 3. DSC curves for BA1032 presenting the main reactions taking place at a temperature of up to 600°C and a heating rate of 5°C/min

Peaks are more visible at higher heating rates, but peaks positioned close to one another can overlap, which rules out heating at a higher rate. The area under the peak was determined based on the onset and endset values of phase transitions to produce comparable results. Data for peaks *c* and *d* from Figures 3, 4 and 5 are presented in Table 1.

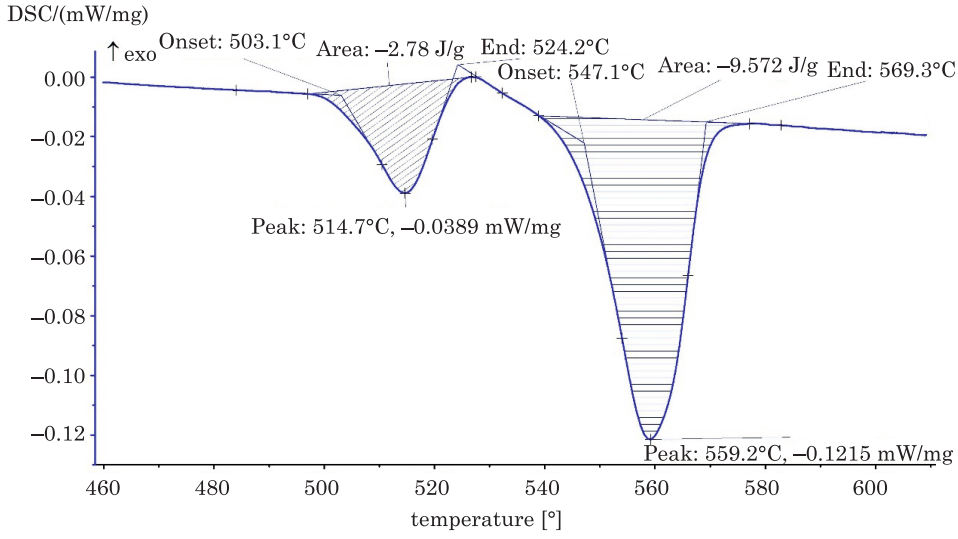

Fig. 4. DSC curves for BA1032 presenting the main reactions taking place at a temperature of up to 600°C and a heating rate of 10°C/min

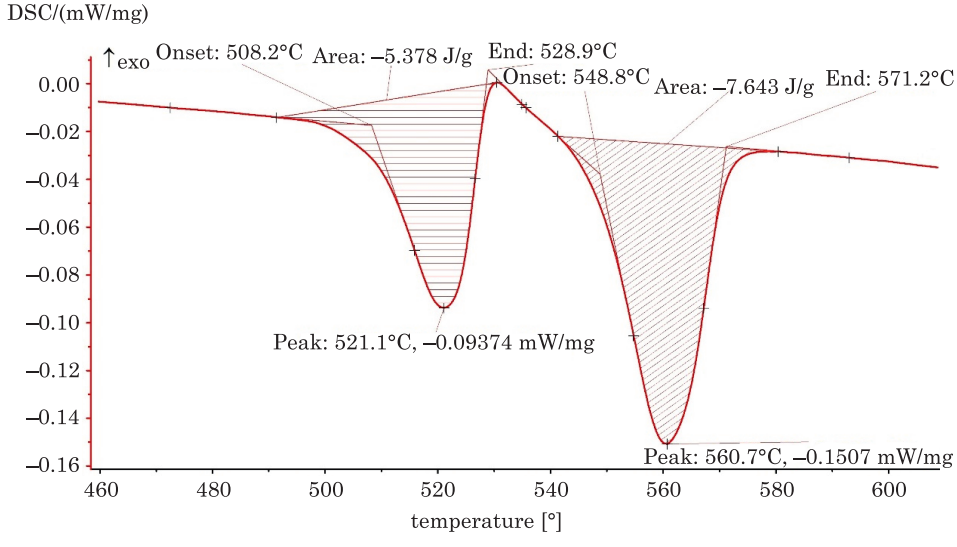

Fig. 5. DSC curves for BA1032 presenting the main reactions taking place at a temperature of up to 600°C and a heating rate of 15°C/min

Table 1
Primary crystallization parameters of BA1032 determined by DSC for peaks *c* and *d*

Heating rate	5°C/min	10°C/min	15°C/min
Peak *c*			
Onset peak [°C]	498.1	503.1	508.2
Maximum peak temperature [°C]	504.1	514.7	521.1
End peak [°C]	510.9	524.2	528.9
Enthalpy of phase transformation peak [J/g]	-1.329	-2.780	-5.378
Peak *d*			
Onset peak [°C]	541.8	547.1	548.8
Maximum peak temperature[°C]	554.4	559.2	560.7
End peak [°C]	564.6	569.3	571.2
Enthalpy of phase transformation peak [J/g]	-12.760	-9.572	-7.643

The peaks *c* and *d* create double endothermic effect and it reflects the eutectoid transformation proceeding at temperature of 565°C, in accordance with phase equilibrium diagram Cu-Al. Analogical effect can be observed during the cooling, of the sample: both effests, the solubility limit of phase α and the exothermic effect of eutectoid transformation starting at a temperature of about 538°C and ending at about 473°C, as shown in Figure 6 (GAZDA et al. 2009).

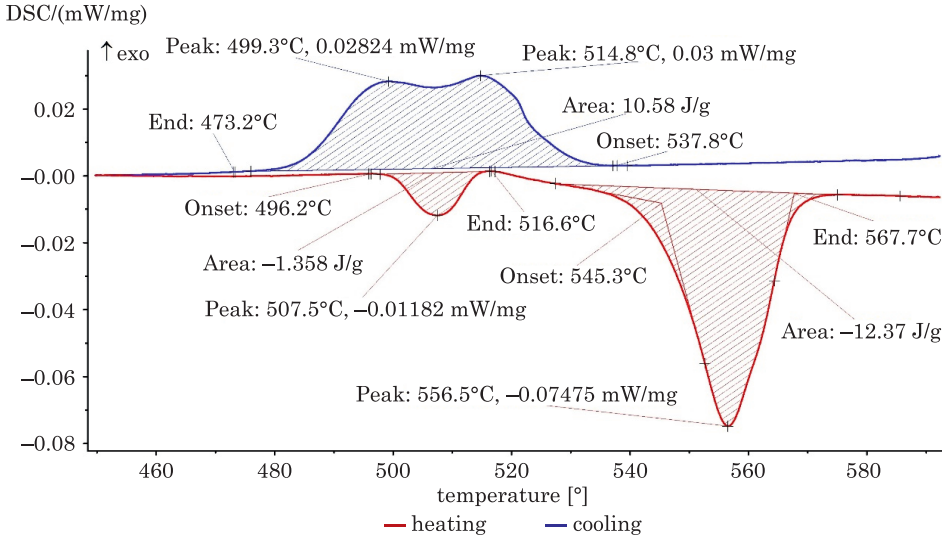

Fig. 6. DSC curves for BA1032 presenting the process of heating and cooling (5°C/min)

Conclusions

Analyzing the results of the research can be concluded that:

– in the present study, four phase transitions were observed in the analyzed material at a temperature of up to 600°C,

– peak broadening can be observed, which indicates that reactions took place relatively slowly within a wide range of temperatures,

– phase transitions *a* and *b* occurred one after the other. An endothermic phase transition ($\nu \rightarrow \alpha + \nu$) took place in peak *a*, whereas an exothermic phase transition ($\alpha + \nu \rightarrow \alpha + \gamma_2$) took place in peak *b*. The temperature of the transition between peaks *a* and *b* was 225°C. The end temperature of peritectoidal transformation ($\alpha + \nu \rightarrow \alpha + \gamma_2$) is 363°C (according to the phase equilibrium diagram), but occurs fastest at a temperature about 267°C. The span across the phase transition is 134°C (od 225°C do 359°C)

– at a heating rate of 10°C/min and 15°C/min, a minor endothermic effect was noted between peaks *b* and *c* beginning from the temperature of around 390°C.

– it confirmed the presence of a double endothermic effect, which consists of peaks *c* and *d*. In peak *c* took place a $\alpha + \gamma_2 \rightarrow \alpha + \gamma_2 + \beta$ transition, whereas in peak *d* a $\alpha + \gamma_2 + \beta \rightarrow \alpha + \beta$ transition. The transitions were noted across a narrow temperature range. The distance between peaks decreased with an increase in heating rate, which can be attributed to an increase in the enthalpy of peak *c* at a higher heating rate. The reverse was observed in peak *d* where enthalpy decreased with an increase in heating rate. When heating rate increases, phase transitions begin later (at higher temperature) and end later, and peak broadening occurs. Energy effects overlap during cooling,

– for industrial practice can be assumed that to achieve the phase $\alpha + \gamma_2$, tempering temperature aluminum-iron-manganese bronze BA1032 should total at least 225°C and not more than 495°C.

References

FRĄCZYK A., BRECZKO T. 2010. *Study of crystalization of Fe95Si5 amorphous alloy using XRD and DSC*. Materials Physics and Mechanics, 2(9): 85–89.

GAZDA A., GÓRNY Z., KLUSKA-NAWARECKA S., POŁCIK H., WARMUZEK M. 2009. *Comparative studies of the effect of various additives on structure and mechanical properties of CuAl10Fe3Mn2 alloy*. Prace Instytutu Odlewnictwa, 49(1): 5–26.

GÓRNY Z., KLUSKA-NAWARECKA S., POŁCIK H. 2003. *Symulacja krzepnięcia brązu aluminiowego BA1032 z weryfikacją doświadczalną.* Archiwum Odlewnictwa, 3(9): 140–147.

PN-EN 12163:2011. *Copper and Copper Alloys – Rod for General Purposes*.

ROMANKIEWICZ F., ROMANKIEWICZ R. 2007. *Study of ferric phase on bronze BA1032.* Archiwum Technologii Maszyn i Automatyzacji, 27(1): 87–91.

SECKO J., RÓŻAŃSKI P. 2011. *Przykładowe wykorzystanie analizy termicznej w badaniach instytutu metalurgii żelaza.* Instytut Metalurgii Żelaza, Prace IMŻ, 1: 32–39.

SUCHOŃ J., JURA S. 2003. *Wyznaczanie spektralnego ciepła krystalizacji brązu B102 i BA1032.* Archiwum Odlewnictwa, 3(10): 221–228.

SZUMERA M. 2012. *Charakterystyka wybranych metod termicznych.* Cz. 1. LAB Laboratoria, Aparatura, Badania, 17(6): 28–34.

SZUMERA M. 2013. *Charakterystyka wybranych metod termicznych.* Cz. 2. LAB Laboratoria, Aparatura, Badania, 18(1): 24–33.

WIERZBICAKA B. 2000. *Obróbka cieplna brązu aluminiowego krzepnącego pod ciśnieniem*. Solidification of Metals and Alloys, 2(42): 117–124.

Technical Sciences, 2016, 19(4), 367–386

Quarterly peer-reviewed scientific journal
ISSN 1505-4675
e-ISSN 2083-4527
TECHNICAL SCIENCES
Homepage: www.uwm.edu.pl/techsci/

EXPERIENCE IN MODELLING OF A SINGLE-STAGE SILICA GEL-WATER ADSORPTION CHILLER

***Jarosław Krzywański*[1], *Małgorzata Szyc*[2], *Wojciech Nowak*[3], *Zygmunt Kolenda*[3]**

[1] Institute of Technical Education and Safety
Jan Dlugosz University in Czestochowa
[2] Fortum Corporation, Czestochowa CHP
[3] Center of Energy
AGH University of Science and Technology

Received 1 June 2016, accepted 18 November 2016, available online 21 November 2016

Key words: low grade thermal energy, waste heat recovery, adsorption chillers, silica gel, coefficient of performance, cooling capacity.

Abstract

Heat utilization for cooling capacity production is nowadays a desirable challenge in several industrial applications. There are lots of industrial processes with low parameters of heat generated as by-product, which utilization is very important to improve theirs total energy efficiency.

Waste heat driven chillers seem to be great competitors for mechanical chillers. Among them special attention should be paid to adsorption chillers, since they can be powered with low – temperature heat sources.

The paper presents a model of a single-stage adsorption chiller with silica gel as adsorbent and water, acting as a refrigerant. The performed model allows to predict the behaviour of the adsorption chiller, among others the main energy efficiency factors, such as coefficient of performance (COP) and cooling capacity (CC) for different working conditions.

Nomenclature

A	–	area of heat exchanger, m^2
CC	–	cooling capacity,
COP	–	coefficient of performance, dimensionless
c_p	–	specific heat capacity at constant pressure, J kg^{-1} K^{-1}
$dM_{chilled}/dt$	–	mass flow rate of chilled water, kg s^{-1}
$dM_{cooling}/dt$	–	mass flow rate of cooling water, kg s^{-1}
$dM_{heating}/dt$	–	flow of hot water, kg s^{-1}
D_S	–	diffusive surface, m_2 s^{-1}
D_{S0}	–	kinetic diffusion constant for the water-silica gel system, m^2 s^{-1}

Correspondence: Jarosław Krzywański, Instytut Techniki i Systemów Bezpieczeństwa, Akademia im. Jana Długosza, al. Armii Krajowej 13/15, 42-200 Częstochowa, phone: 34 361 59 70, e-mail: jkrzywanski@tlen.pl

E_a – activation energy, kJ kmol^{-1}
h – specific enthalpy, latent heat of evaporation, kJ kg^{-1}
HP – heating power transferred with the hot water flow
K – mass transfer coefficient, m s^{-1}
K_0 – Tóth constant, 1 Pa^{-1}
M – mass, kg
n – structural heterogeneity parameter
P – pressure, Pa
q – amount of vapor adsorbed in the bed, kg kg^{-1}
q* – maximum bed saturation under given temperature and pressure conditions, kg kg^{-1}
q_0 – monolayer maximum sorption capacity of silica gel, kg kg^{-1}
Q_{ST} – isostheric heat of adsorption, kJ kg^{-1}
R – universal gas constant or individual or for water vapor, kJ kmol^{-1} K^{-1}
R_p – average radius of silica-gel particles, m
t – dimensionless Tóth constant
T – temperature, K
T_0 – temperature at starting point for model calculation, K
t_{cycle} – cycle time, s
T_k – temperature of water inside of heat exchanger component, K
U_{cond} – heat transfer coefficient during condensation, W m^{-2} K^{-1}
$U_{cooling}$ – heat transfer coefficient during bed cooling process, W m^{-2} K^{-1}
U_{evap} – heat transfer coefficient during evaporation, W m^{-2} K^{-1}
$U_{heating}$ – heat transfer coefficient during bed heating process, W m^{-2} K^{-1}
v – specific volume of the vapour phase under given conditions, m^3 kg^{-1}
V – volume of water flowing via heat exchanger, m^3

Greek symbols

γ – flag coefficient
δ – flag coefficient
θ – flag coefficient
ρ – density of water at a given temperature, kg m^{-3}
χ – flag coefficient

Subscripts and superscripts

ads – adsorber
bed – bed
chw – chilled water
cond – condenser
cw – cooling water
evap – evaporator
f – liquid state
g – gas, vapour state
Hex – heat exchanger
hw – hot water
i – inlet
ini – initial state
max – maximumm
o – outlet
ref – refrigerant
s – saturated state
sg – silica gel
x – adsorption
y – desorption
z – switching time

Introduction

In their vast majority, high valued energy sources, e.g. electricity and fossil fuel driven appliances are used for the heating and cooling purposes. However, there are also a wide range of low grade sources of thermal energy, e.g. sewage water, underground resources, solar heat, waste heat, which also can be used to deliver useful heating or cooling (AMMAR et al. 2012, STANEK, GAZDA 2014). Adsorption cycles have a distinct advantage over other systems in the ability to use low grade heat, especially heat of low near ambient temperature (AMMAR et al. 2012, STANEK, GAZDA 2014).

Application of adsorption processes for cooling cycle was first described in 1920s (LOH 2010). Further research in this area provided lots of experimental data for different pairs of adsorbent-adsorbate (ARISTOV et al. 2006, DEMIR et al. 2008, WANG et al. 2014). A novel design with passive evaporation was discussed by WANG et al. (2011) and most common pairs of adsorbent-adsorbate are reported by DEMIR et al. (2008). The adsorption of water on silica gel surface was examined inter alia by ARISTOV et al. (2006) and CHUA et al. (2002). Results of experiment for silica gel impregnated with $CaCO_3$ can be found in AKISAWA and MIYAZAKI (2010). Adsorption kinetics for active carbon-R134a and active carbon – R507A was investigated in HABIB et al. (2010).

Besides zeolite/water the silica gel-water is considered as one of the most promising working pairs best suited for the solutions using low grade sources of thermal energy (MYAT et al. 2013, SZYC, NOWAK 2014a,b. SIMILAR conclusion was reported in CHOROWSKI and PYRKA (2015) and QIAN et al. (2013).

It is due to relatively easy regeneration process of the adsorbent. These two pairs adsorbent-adsorbate mostly have found their implementation in commercialised chillers offered by suppliers on market.

There are some applications with adsorption chillers in industrial scale in Europe. Adsorption chillers can use solar energy (HABIB et al. 2013, SEKRET, TURSKI 2012 and other waste heat sources. A review of the existing installations can be found inter alia by Wu et WANG (2006).

One of the well-known method to improve the heat and mass transfer coefficient between the bed of sorbent and the immersed heating surface is the idea to apply of a fluidized bed instead of the fixed-bed of the sorbent, commonly used in the heat recovery technologies (KRZYWANSKI et al. 2012, WIN et al. 1995, YANG 2003). WANG et al. (2012) proposed a fluidized-bed adsorber/desorber for the adsorption refrigeration system. The working pair of activated carbon and R134a in a fluidized bed was applied in the paper. The authors pointed out that the fluidized adsorbent can enhance the heat and mass transfer, leading to the increase the specific cooling power. Due to the enhanced heat and mass transfer the heating transfer area can be greatly

reduced which is beneficial, extending the applications of the adsorption refrigerators (WANG et al. 2012).

CHEN et al. (2015) proposed to use a periodic operating silica gel fluidized bed system to adsorb/desorb moisture in air-conditioning systems. The authors reported that the fluidized bed system allows to increase the adsorption/desorption processes compared with the packed bed. HORIBE et al. (2013) applied fluidized bed to study the sorption and desorption characteristics of a new organic sorbent material HU720PR. The connected fluidized beds for adsorption and desorption processes are used in the unit. Two funnels inside the beds allow particles to circulate between adsorption and desorption beds to ensure continuous operating of a dehumidification air conditioning system (CHEN et al. 2015). Similar process was also carried out by HAMED (2005). The author used an inclined-fluidized bed in the adsorption and desorption operations.

The main feature of adsorption chillers is its lower sensitivity to hot water inlet temperature fluctuations. It makes adsorption chillers more suitable for the use of low grade sources of thermal energy in comparison to their main competitors, i.e. absorption chillers. The improvement of total efficiency of adsorption process is however still challenging task.

Modelling is a wide used method of data handling which can be helpful to carry out such undertaking. Several models and experimental works on adsorption cooling cycles are described in the literature. Modeling and performance analysis of an adsorption desalination cycle was described by THU (2010), whereas the distributed-parameter approach to capture both the transient and steady state behaviors of adsorption chiller was presented by CHUA et al. (2004). A dynamic model for the prediction of the optimal cyclic operation mode of the two-bed adsorption chiller was shown by GRÄBER et al. (2011).

The analysis of an advanced three-stage adsorption chiller as well as the entropy generation analysis and performance analysis of a pressurized adsorption chiller were presented in LOH et al. (2010), SAHA et al. (1995), THU et al. (2013).

A multi-bed regenerative adsorption chiller design and a novel silica gel-water adsorption chiller model with three vacuum chambers were proposed by CHUA et al. (2001) and WANG et al. (2005), respectively.

The experimental analysis of a compact adsorption chiller, the evaluation of the effect of adsorbent isobar shape on the dynamics of the chillers and the water adsorption dynamics for adsorption chillers with adsorbent beds of loose grains was discussed in ARISTOV et al. (2012), LU et al. (2013) and OKUNEV and ARISTOV (2014). The dynamic behaviour of a single effect two bed adsorption chiller employing adsorbent beds with various layers of loose grain configur-

ations and silica gel particle sizes and the effect of design parameters on the switching frequency was discussed by CHAKRABORTY et al. (2014) and ALAM et al. (2003), respectively.

Analytically and experimentally investigated silica gel-water system was described by BOELMAN et al. (1995) and SAHA et al. (1995). Three-bed and a dual mode, three stage non-regenerative and six bed regenerative silica gel – water chillers were investigated in SAHA (2003) and SAHA et al. (2003).

The work presents a model of a single-stage adsorption chiller with silica gel acting as a solid porous sorbent and water working as refrigerant. The set of thermodynamic equations used in the model of chiller operation is described in the paper. The validation of the model was successfully performed against the experimental results from the existing adsorption chiller at National University of Singapore. Such approach is undertaken since the comparison between desired and calculated data is regarded as the most difficult type of model's validation procedure (KRZYWANSKI et al. 2015a, b, c).

An object of investigations and working principle

Typical single stage-adsorption chiller consists of: an evaporator, a condenser and two fixed-beds, which are packed in separate reactors (CHUA et al. 2001, LOH 2010, THU 2010). Silica gel-water is considered during the study as a working pair of adsorbent-adsorbate. Solid porous sorbent has relatively high sorption capability with refrigerant. The heat transfer between hot and cold water and the sorbent occurs via the coils immersed inside the beds. The scheme of the considered system is given in Figure 1.

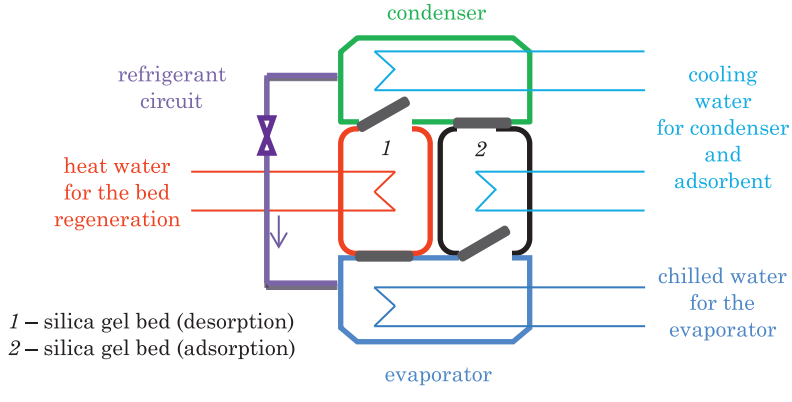

Fig. 1. Schematic diagram of an adsorption chiller

The experimental procedure for a conventional adsorption chiller is as follows. The evaporated refrigerant (water) passes form the evaporator to the fixed adsorption bed 2, which is cooled by the cold water flowing inside tubes into the bed. The adsorption processes occur until the pressure inside the adsorption bed reaches about the saturated pressure of water, corresponding to the cooling water temperature in the adsorption bed. To regenerate the bed, hot water is put into the coil and the vapour is released from the bed.

The desorbed vapour enters into the condenser (SZYC, NOWAK 2014a, b).

To improve the efficiency more than one bed are applied. Adsorption chillers usually consists of two or four beds (CHOROWSKI, PYRKA 2015, SZYC, NOWAK 2014a, b). When some of the beds work as adsorbers, the desorption process occurs in other beds at the same time, and on the contrary.

To increase the efficiency of the unit, the beds must be properly prepared for the upcoming phase. Therefore before the two main stages (i.e. adsorption and desorption) starts the beds previously must be pre-heated (before desorption) or pre-cooled (before adsorption), respectively.

During these short periods, usually called switching time periods, all valves connecting the beds with the evaporator and the condenser are closed.

By this way, four phases, i.e.: pre-cooling, adsorption, pre-heating and desorption, occur one by one during the full adsorption cooling cycle in each of the bed of an adsorption chiller.

Mathematical modelling of adsorption chiller

Fundamental assumptions

The model is based on Tóth adsorption isotherm, equation of the kinetics of the process and energy balance equations for the elements: evaporator, condenser and silica gel bed (CHUA et al. 2004, SZYC, NOWAK 2014a). The RD silica gel type is used as an adsorbent. To simplify the model, the following assumptions were taken into account:

– the values for pressure and temperature in isotherm equations during adsorption are constant, i.e. the reactor pressure is equal to the pressure in the evaporator and the reactor temperature is equal to the temperature of the cooling water bed,

– isosteric heat of adsorption is constant,

– water vapour adsorbed on the silica gel is in dry saturated conditions ($x = 1$),

– the adsorption of water vapour on silica gel is uniform,

– water vapour is adsorbed on the dry silica gel in each cycle, so the maximum amount of refrigerant is uptaken by bed under the considered pressure and temperature conditions,

– the temperature profile across the bed is uniform,

– the temperature in the different parts of the device is uniform,

– heat transfer coefficients for heat exchangers have constant values,

– the system is thermally insulated from the environment (the losses have been omitted),

– during the adsorption phase the reactor pressure is constant and has the same value as in the evaporator,

– during the desorption phase the pressure in the reactor is constant and has the same value as the condenser.

The system of balance differential equations was solved by the Runge--Kutty method of the 4^{th} order using C++ language.

Adsorption isotherm and refrigerant uptake by bed

For estimation of the amount of vapor adsorbed on the bed surface the Tóth isotherm is used (CHUA et al. 2004):

$$q^* = \frac{K_0 \exp\left[\frac{Q_{ST}}{RT_s}\right] P_s}{\left\{1 + \left[\frac{K_0}{q_0} \exp\left(\frac{Q_{ST}}{RT_s}\right) P_s\right]^t\right\}^{\frac{1}{t}}} \tag{1}$$

The changes of bed saturation in time describes linear driving force equation (LOH et al. 2010):

$$\frac{dq(t)}{dt} = K(q^* - q) \tag{2}$$

The K coefficient is defined, as follows:

$$K = \frac{15 D_s}{R_p{}^2} \tag{3}$$

where:

$$D_s = D_{s0} \exp\left[\frac{-E_a}{RT_s}\right] \tag{4}$$

Substituting equation (4) to (3), and then into equation (2), we have the final equation (5):

$$\frac{dq(t)}{dt} = \frac{15D_{s0}\exp\left[\frac{-E_a}{RT_s}\right](q^* - q)}{R_{p^2}} \tag{5}$$

The isosteric heat adsorption can be expressed by the Dubinin-Astakov equation (LOH et al. 2010):

$$Q_{ST} = h + E_a \ln\left(\frac{q_0}{q}\right)^{1/n} + Tv_g\frac{dP}{dT}(P,T) \tag{6}$$

Energy balance during adsorption phase

For bed which is connected to the evaporator (index x) the energy balance can be written, as follows:

$$\left(M_{sg}cp_{sg} + M_{Hex}cp_{Hex} + M_{sg}q_{bed,x}\left[cp_g(,T_{bed,x}) + Q_{ST}\left\{\frac{1}{T_{bed,x}} - \frac{1}{v_g(T_{bed,x})}\left(\frac{\partial v_g}{\partial T_{bed,x}}\right)\right\}\right]\right)$$

$$\frac{dT_{bed,x}}{dt} = M_{sg}\frac{dq_{bed,x}}{dt}[\delta\{h_g(T_{evap}) - h_g(T_{bed,x}) + Q_{ST}\} + (1-\delta)\{h_g(T_{i,chw}) - h_g(T_{bed,x}) +$$

$$Q_{ST}\}] - U_{cooling}A_{bed}(T_{bed,x} - T_k) \tag{7}$$

The equation (7) allows to determine bed temperature profile during adsorption.

The energy balance equation for the cooling water, which flows inside tubes immersed into the sorbent bed during the adsorption stage, is as follows:

$$\rho_f cp_f(T_k)V_{bed}\frac{dT_k}{dt} = \frac{dM_{cooling}}{dt}[h_f(T_{i,cw}) - h_f(T_k)] + U_{cooling}A_{bed}(T_{bed,x} - T_k) \tag{8}$$

where:

$$T_0(t) = T_{i,cw},\ T_k(0) = T_{i,cw},\ T_{bed,x}(0) = T_{i,cw},\ T_{evap}(0) = T_{i,chw},\ q_{bed,x}(0) = q^{ini}{}_{bed,x}$$
$$P_{evap}(0) = P_s(T_{i,chw}).$$

This equation allows to estimate the temperature profile for cooling water which is responsible for removing heat of adsorption.

Energy balance during desorption phase

The energy balance for the bed which is connected with the condenser (index y) can be expressed by the equation:

$$\left(M_{sg}cp_{sg} + M_{Hex}cp_{Hex} + M_{sg}q_{bed,y}\left[cp_g(T_{bed,y}) + Q_{ST}\left\{\frac{1}{T_{bed,y}} - \frac{1}{v_g(T_{bed,y})}\left(\frac{\partial v_g}{\partial T_{bed,y}}\right)\right\}\right]\right)$$

$$\frac{dT_{bed,y}}{dt} = M_{sg}\frac{dq_{bed,y}}{dt}[\theta\{h_g(T_{i,hw}) - h_g(T_{bed,y}) + Q_{ST}\} + (1-\theta)\{h_g(T_{cond}) - h_g(T_{bed,y}) +$$

$$Q_{ST}\}] - U_{heating,y}A_{bed,y}(T_{bed,y} - T_k) \quad (9)$$

Equation (9) allows to determine bed temperature changes during desorption.

The energy balance for hot water supplied for the desorption process can be written, as follows:

$$\rho_f cp_f(T_k)V_{bed}\frac{dT_k}{dt} = \frac{dM_{heating}}{dt}[h_f(T_{i,hw}) - h_f(T_k)] + U_{heating,y}A_{bed,y}(T_{bed,y} - T_k) \quad (10)$$

where:

$$T_0(t) = T_{i,hw},\ T_{bed,y}(0) = T_{i,hw},\ q_{bed,y}(0) = q_{inibed,y},\ P_{cond}(0) = P_s(T_{i,cw}),\ T_k(0). = T_{i,hw}.$$

Energy balance during switching time

In the period when a bed is prepared for desorption, reactor is not connected neither with the evaporator nor condenser (index z). The energy balance for the bed can be described by the equation:

$$\left(M_{sg}cp_{sg} + M_{Hex}cp_{Hex} + M_{sg}q_{bed,z}\left[cp_g(T_{bed,z}) + Q_{ST}\left\{\frac{1}{T_{bed,z}} - \frac{1}{v_g(T_{bed,z})}\left(\frac{\partial v_g}{\partial T_{bed,z}}\right)\right\}\right]\right)$$

$$\frac{dT_{bed,z}}{dt} = -U_{heating}A_{bed}(T_{bed,z} - T_k) \quad (11)$$

Similar energy balance equations can be written for the adsorption stage (equation 12):

$$\left(M_{sg}cp_{sg} + M_{Hex}cp_{Hex} + M_{sg}q_{bed,z}\left[cp_g(T_{bed,z}) + Q_{ST}\left\{\frac{1}{T_{bed,z}} - \frac{1}{v_g(T_{bed,z})}\left(\frac{\partial v_g}{\partial T_{bed,z}}\right)\right\}\right]\right)$$

$$\frac{dT_{bed,z}}{dt} = -U_{cooling}A_{bed}(T_{bed,z} - T_k) \tag{12}$$

For hot water flowing inside the tubes immerged in the adsorber bed we have:

$$\rho_f cp_f(T_k)V_{bed}\frac{dT_k}{dt} = \frac{dM_{heating}}{dt}[h_f(T_{i,hw}) - h_f(T_k)] + U_{heating}A_{bed}(T_{bed,z} - T_k) \tag{13}$$

and the same for cooling water:

$$\rho_f cp_f(T_k)V_{bed}\frac{dT_k}{dt} = \frac{dM_{cooling}}{dt}[h_f(T_{i,hw}) - h_f(T_k)] + U_{cooling}A_{bed}(T_{bed,z} - T_k) \tag{14}$$

where:
$T_0(t) = T_{i,hw}$ or $T_{i,cw}$, $T_{bed,z}(0) = T_{i,hw}$ or $T_{i,cw}$, $q_{bed,z}(0) = q^{ini}_{bed,z}$, $P_{cond}(0) = P_s(T_{i,cw})$, $T_k(0) = T_{i,hw}$.

Energy balance for the evaporator

The energy balance for the evaporator is described as follows:

$$[cp_f(T_{evap})M_{ref,evap} + cp_{evap}M_{evap}]\frac{dT_{evap}}{dt} + h_f(T_{evap})\frac{dM_{ref,evap}}{dt} =$$

$$-\theta(1-\gamma)h_f(T_{cond})M_{sg}\frac{dq_{bed,x}}{dt} - [\delta h_g(T_{evap}) + (1-\delta)h_g(T_{bed,x})]M_{sg}\frac{dq_{bed,x}}{dt} -$$

$$U_{evap}A_{evap}(T_{evap} - T_k) \tag{15}$$

where amount of refrigerant circulated in cooling loop is calculated from:

$$\frac{dM_{ref,evap}}{dt} = -M_{sg}\sum_{z=1}^{2}\chi\frac{dq_{bed}}{dt} \tag{16}$$

During the period, when a bed is connected with the evaporator (adsorption) $\chi = 1$, whilst $\chi = \theta(1 - \gamma)$ when bed is connected with condenser, during desorption, and:

$$\frac{dM_{ref,evap}}{dt} = - M_{sg} \left((1 - \delta)(1 - \gamma) \frac{dq_{bed}}{dt} \right) - \frac{dq_{bed}}{dt} \tag{17}$$

For chilled water the energy balance equation can be written as follows:

$$\rho_f cp_f(T_k) V_{evap} = \frac{dM_{chilled}}{dt} [h_f(T_{i,chw}) - h_f(T_k)] + U_{evap} A_{evap} (T_{evap} - T_k) \tag{18}$$

where:
$M_{ref,evap}(0) = M_{ref,evap}^{ini}$, $T_0(t) = T_{i,chw}$, $T_{evap}(0) = T_{i,chw}$, $T_{bed,x}(0) = T_{i,cw}$, $T_{cond}(0) = T_{i,cw}$, $T_k(0) = T_{i,chw}$.

Energy balance for the condenser

The energy balance for the condenser can be described by the following equation:

$$[cp_f(T_{cond}) M_{ref,cond} + cp_{cond} M_{cond}] \frac{dT_{cond}}{dt} - \gamma h_f(T_{cond}) M_{sg} \frac{dq_{bed,y}}{dt} = -[\theta h_g(T_{bed,y}) + (1 - \theta) h_g(T_{cond}) - \theta(1 - \gamma) h_f(T_{cond})] M_{sg} \frac{dq_{bed,y}}{dt} - U_{cond} A_{cond} (_{evap} - T_k) \tag{19}$$

When the condenser collects sufficient amount of condensate $M_{ref,cond}^{max}$, refrigerant flows into the evaporator. The governing assumptions are as follows:

– when $M_{ref,cond} < M_{ref,cond}^{max}$, or $M_{ref,cond} = M_{ref,cond}^{max}$, and $\frac{dq_{bed,y}}{dt} > 0$ then $\gamma = 1$

and

– when $M_{ref,cond} = M_{ref,cond}^{max}$ and $\frac{dq_{bed,y}}{dt} \leq 0$ then $\gamma = 0$.

The energy balance for cooling water in condenser is, as follows:

$$\rho_f cp_f(T_k) V_{cond} \frac{dT_k}{dt} = \frac{dM_{cond}}{dt} [h_f(T_{i,cw}) - h_f(T_k)] + U_{cond} A_{cond} (T_{cond} - T_k) \tag{20}$$

where:
$M_{ref,cond}(0) = M^{max}_{ref,cond}$, $T_0(t) = T_{i,cw}$,$T_{cond}(0) = T_{i,cw}$, $T_{bed,y}(0) = T_{i,hw}T_k(0) = T_{i,cw}$.

Performance parameters

The main performance parameter of a chiller is Coefficient of Performance (COP), defined as:

$$COP = \frac{CC}{HP} \tag{21}$$

where CC is cooling capacity achieved from the system and HP is heating power supplied to the system.

The CC and HP can be determine from the equations (22) and (23):

$$CC = \frac{dM_{chilled}}{dt} cp_{f,i,chw}(T_{i,chw} - T_{o,chw}) \tag{22}$$

$$HP = \frac{dM_{heating}}{dt} cp_{f,i,hw}(T_{i,hw} - T_{o,hw}) \tag{23}$$

Results and discussion

Validation

The above presented set of balance equations was used to create the simulation code in C++ programming language. The performed model allows to determine temperature profiles for each of the elements and further to calculate performance coefficients, like coefficient of performance (COP) and cooling capacity (CC). Operating parameters of simulated single – stage adsorption chiller are given in Table 1.

The results of simulations were compared with experimentally obtained data for two different working conditions. The experimental data which has been collected, analysed and compared with simulation results comes from the existing adsorption chiller installed at the National University of Singapore. The detailed description of the adsorption system can be found in SZYC, NOWAK 2014a,b, THU 2010). The system can also work with heat regeneration, but during experiments it operated as a single-stage device. The measured

Table 1

The operating parameters used in the study

Parameter	Temperature °C		Mass flow rate kg s^{-1}	Other
	test 1	test 2		
Chilled water inlet (evaporator)	10	20	0.8	–
Cooling water inlet (adsorber)	29.5		0.8	–
Cooling water inlet (condenser)	29.5		2.0	–
Hot water inlet (desorber)	70–110		0.8	–
Mass of silica-gel (per bed) [kg]	–		–	36
Switching time [s]	–		–	45
Cycle time adsorption/desorption [s]	–		–	480–900

Table 2

Selected data used for simulations

Parameter	Value
q_0	0.45
Q_{ST}	2.37×10^{3}
K_0	2×10^{-12}
t	12
R_p	1.7×10^{-4}
D_{s0}	2.54×10^{-4}
E_a	4.2×10^{4}
n	1.1
$c_{p,sg}$	0.921
$M_{Hex}c_{p,Hex}$	195
A_{ads}	47.1
V_{cond}	0.1
V_{bed}	0.157
V_{evap}	0.0142
$M_{evap}c_{p,evap}$	25.4
$M_{cond}c_{p,cond}$	18.0
$M^{max}_{ref,cond}$	10

data were sampled every 3 second. Selected data used further for calculations are given in Table 2. These values together with the data from Table 1 constitute the parameters of entry conditions during simulations.

The comparison between desired and calculated by the model values of COP and CC during Tests 1 and 2 are given in Figures. 2 and 3. The calculated results are located within the range of ± 20% compared to the desired, i.e. experimental data.

The points in the Figures 2 and 3 which were used to validate the model, correspond to different inlet temperatures of chilled water. The approach was undertaken since the comparison between desired and calculated data is regarded as the most difficult type of model's validation procedure (KRZYWANSKI et al. 2015b,c).

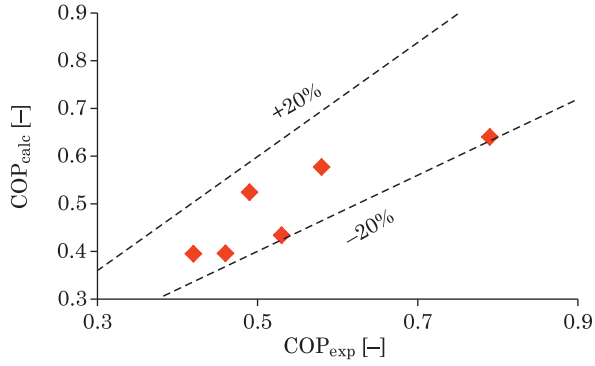

Fig. 2. Comparison between measured and calculated results for the coefficient of performance

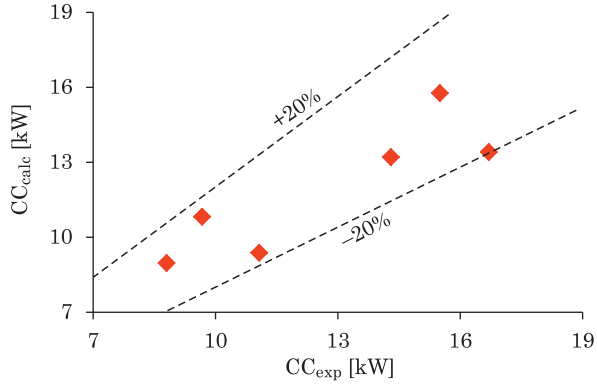

Fig. 3. Comparison between measured and calculated results for the cooling capacity

The effect of the cycle time

The dependence of the COP on the cycle time for the two considered inlet temperatures of chilled water is presented in Figure 4. As it can be seen the coefficient of performance increases with the cycle time.

Similar results were obtained by other researchers (MARLINDA et al. 2010, WANG et al. 2015). Such behaviour can be explained taking into account the differences between sorption and desorption rates and is also the result of the changes in dynamism of adsorption/desorption processes with time. Since the desorption runs faster than adsorption the heating power HP supplied to the bed may not be consumed during desorption stage when lengthening the cycle time. Therefore the instantaneous value of the heating power, constituting the denominator in equation (21), used for desorption is reduced leading to the increase in COP (MARLINDA 2010, SZYC, NOWAK 2014a).

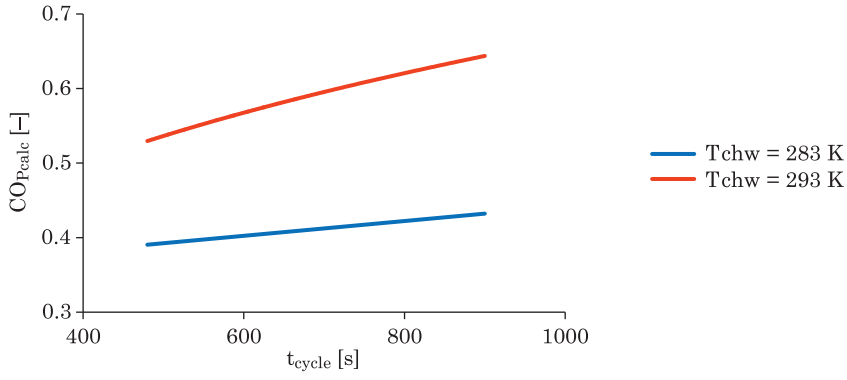

Fig. 4. The effect of the time cycle on the coefficient of performance

The effect of the cycle time on the cooling capacity is shown in Figure 5. Similar behaviour was reported by MARLINDA et al. (2010) and SAPIENZA et al. (2011). When the cycle time gets longer the water vapour-silica gel system tends to reach equilibrium and sorption processes are slowing down. This influencing the cooling capacity ratio as the coolant mass transfer between the condenser and the evaporator is also slowed down. As the result the disturbances in coolant evaporation process occur, which leads to the decrease in cooling capacity of the adsorption chiller (SZYC, NOWAK 2014a).

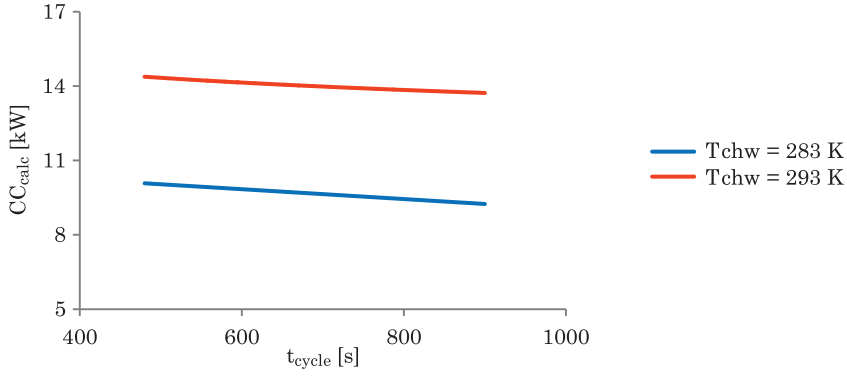

Fig. 5. The effect of the time cycle on the cooling capacity

The effect of the chilled and hot water inlet temperature

The effect of the hot water inlet temperature on the COP is given in Figure 6. The heating power (HP) supplied to the system increases with the hot water inlet temperature T_{hw}. As the HP constitutes the denominator in equation (20) the COP decreases with the increase of hot water inlet temperature.

Generally speaking, both considered parameters, i.e. COP and CC are higher for the chilled inlet water temperature of 20°C than it is for the T_{chw} = 10°C. Similar behaviour was noted by JEON et al. (2010). Since the evaporation processes are enhanced at higher temperatures the increase in the chilled water inlet temperature cause the increase in cooling capacity CC, achieved from the system. As the result, according to equation (20), the COP tends to increase.

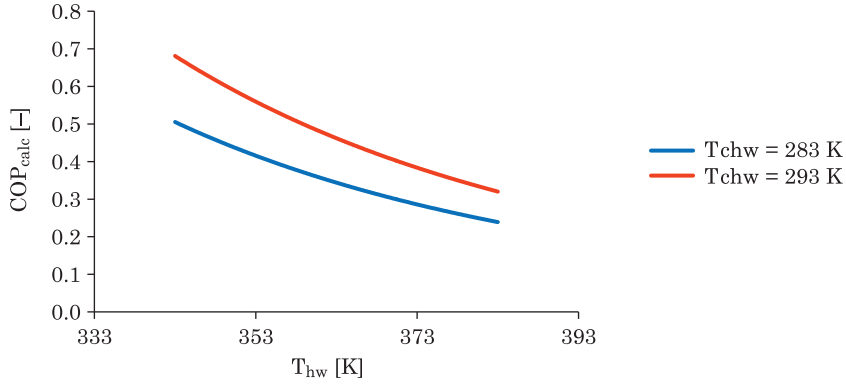

Fig. 6. The effect of the hot water inlet temperature on the coefficient of performance

The effect of the cooling water temperature and the typical profiles of beds temperatures and amounts of vapour adsorbed on the silica gel

The dependence of the cooling water temperature on the CC and COP is given in Figure 7. The main energy efficiency factors, such as coefficient of performance and cooling capacity decrease with the increase in cooling water temperature. It is the result of the decrease in the amounts of refrigerant being adsorbed for higher temperatures of cooling water flowing inside tubes into the bed. Typical profiles of the average bed temperatures as well as the amounts of vapour adsorbed on the silica gel are shown in Figure 8. As it can be seen the profiles correspond to both adsorption an desorption cycles.

Conclusions

The paper presents a model of a single-stage adsorption chiller with silica gel as adsorbent and water acting as a refrigerant. The validation of the model was successfully performed against the experimental results from the existing

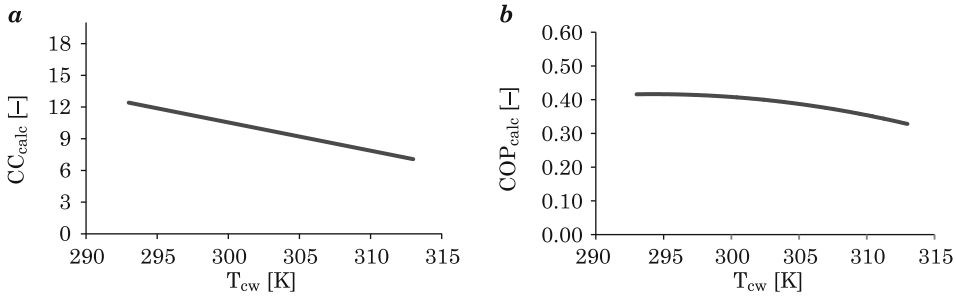

Fig. 7. The effect of the cooling water temperature on the: *a* – cooling capacity and *b* – coefficient of performance; T_{chw} = 283 K

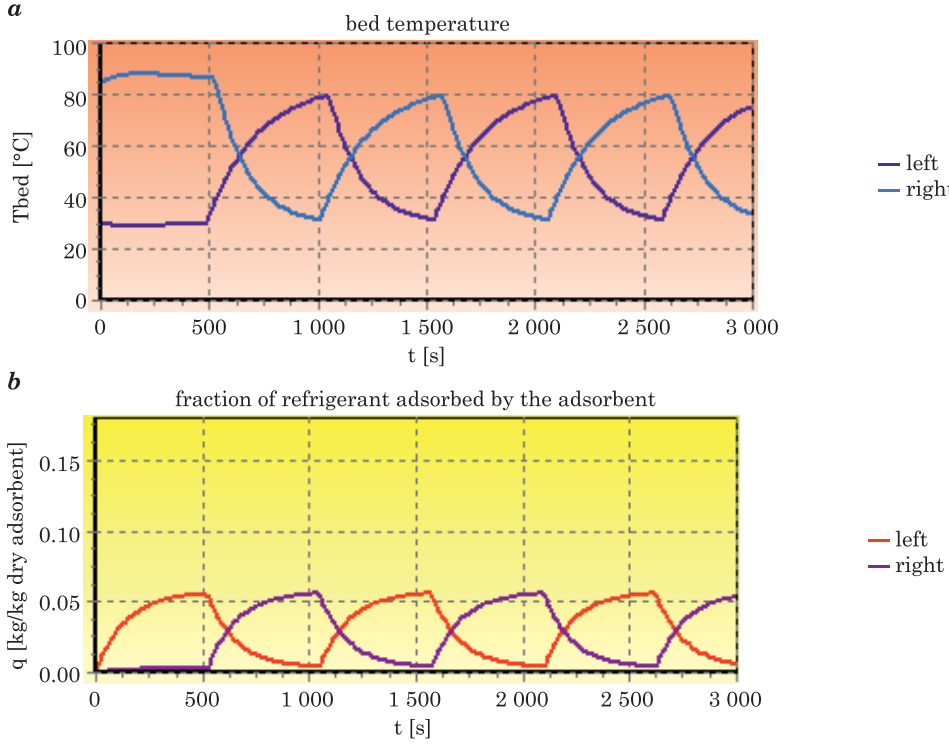

Fig. 8. The average beds temperatures (*a*) and amounts of vapour adsorbed profiles (*b*)

adsorption chiller installed at the National University of Singapore. Obtained results (calculated data) are located in the borders of ± 20% in the relationship to experimental results.

The developed model allows to predict the behaviour of the adsorption chiller, among others the main energy efficient factors, i.e. coefficient of

performance (COP) and cooling capacity (CC) for different working conditions. The calculations carried out in the paper lead to the fallowing conclusions:

– the coefficient of performance increases whereas cooling capacity decreases with the cycle time,

– the COP decreases with the increase of hot water inlet temperature,

– both considered parameters, i.e. COP and CC are higher for the higher chilled inlet water temperatures,

– the main energy efficiency factors (i.e. COP and CC) decrease with the increase in cooling water temperature.

The developed model can be used as an optimization tool of the examined adsorption chiller.

Acknowledgments

The authors thank NG Kim Choon for making possible to conduct the experiments during the internship in Singapore. They also would like to thank Fortum Corporation and New Energy Transfer Company for their financial support. The co-author, Małgorzata Szyc, received a grant for the project DoktoRIS Scholarship Program for innovative Silesia co-financed by the European Union under the European Social Fund.

References

Akisawa A., Miyazaki T. 2010. *Multi-bed adsorption heat pump cycles and their optimal operation*. In: *Advances in Adsorption Technology*. Eds. B.B. Saha, K.C. Ng. Nova Science Publishers, p. 241–279.

Alam K.C.A., Kang Y.T., Saha B.B., Akisawa A., Kashiwagi T. 2003. *A novel approach to determine optimum switching frequency of a conventional adsorption chiller*. Energy, 28: 1021–1037.

Ammar Y., Joyce S., Norman R., Wang Y., Roskilly A.P. 2012. *Low grade thermal energy sources and uses from the process industry in the UK*. Applied Energy, 89: 3–20.

Aristov Y.I., Glaznev I.S., Girnik I.S. 2012. *Optimization of adsorption dynamics in adsorptive chillers: loose grains configuration*. Energy, 46: 484–492.

Aristov Y.I., Tokarev M.M., Freni A., Glaznev I.S., Restuccia G. 2006. *Kinetics of water adsorption on silica Fuji Davison RD*. Microporous and Mesoporous Materials, 96: 65–71.

Boelman E., Saha B.B., Kashiwagi T. 1995. *Experimental investigation of a silica gel water adsorption refrigeration cycle – the influence of operating conditions on cooling output and COP*. ASHRAE Transactions, 101: 358–366.

Chakraborty A., Saha B.B., Aristov Y.I. 2014. *Dynamic behaviors of adsorption chiller: Effects of the silica gel grain size and layers*. Energy, 78: 304–312.

Chen C.H, Schmid G., Chan C.T., Chiang Y.C., Chen S.L. 2015. *Application of silica gel fluidised bed for air-conditioning systems*. Applied Thermal Engineering, 89: 229–238.

Chorowski M., Pyrka P. 2015. *Modelling and experimental investigation of an adsorption chiller using low-temperature heat from cogeneration*. Energy, 92: 221–229.

Chua H.T., Ng K.C., Chakraborty A.O.N.M., Othman M.A. 2002. *Adsorption Characteristics of Silica Gel + Water System*. Journal of Chemical & Engineering Data, 47: 1177–1181.

CHUA H.T., NG K.C., MALEK A., KASHIWAGI T., AKISAWA A., SAHA B.B. 2001. *Multi-bed regenerative adsorption chiller-improving the utilization of waste heat and reducing the chilled water outlet temperature fluctuation*. International Journal of Refrigeration, 24(2): 124–136.

CHUA H.T, NG K.C, WANG W., YAP C., WANG X.L. 2004. *Transient modeling of a two-bed silica gel-water adsorption chiller*. International Journal of Heat and Mass Transfer, 47: 659–669.

DEMIR H., MOBEDI M., ÜLKÜ, S. 2008. *A review on adsorption heat pump: problems and solutions*. Renew Sustain Energy Rev, 12: 2381–2403.

GRÄBER M., KIRCHES C., BOCK H.G., SHLÖDER J.P., TEGETHOFF W., KÖHLER J. 2011. *Determining the optimum cyclic operation of adsorption chillers by a direct method for periodic optimal control*. International Journal of Refrigeration, 34: 902–913.

HABIB K., CHOUDHURY B., CHATTERJEE P.K., SAHA B.B. 2013. *Study on a solar heat driven dual-mode adsorption chiller*. Energy, 63: 133–141.

HABIB K., SAHA B.B., RAHMAN K.A., CHAKRABORTY A., KOYAMA S., NG K.C. 2010. *Experimental study on adsorption kinetics of activated carbon/R134a and activated carbon/R507A pairs*. International Journal of Refrigeration, 33: 706–713.

HAMED A.M. 2005. *Experimental investigation on the adsorption/desorption processes using solid desiccant in an inclined-fluidized bed*. Renewable Energy, 30: 1913–1921.

HORIBE A., HARUKI N., HIRAISHI D. 2013. *Sorption-desorption operations on two connected fluidized bed using organic sorbent powder*. International Journal of Heat and Mass Transfer, 65: 817–825.

JEON J., LEE S., HONG D., KIM Y. 2010. *Performance evaluation and modeling of a hybrid cooling system combining a screw water chiller with a ground source heat pump in a building*. Energy, 35: 2006–2012.

KRZYWANSKI J., NOWAK W. 2012. *Modeling of heat transfer coefficient in the furnace of CFB boilers by artificial neural network approach*. International Journal of Heat and Mass Transfer, 55: 4246–4253.

KRZYWANSKI J., NOWAK W. 2015a. *Artificial Intelligence Treatment of SO_2 Emissions from CFBC in Air and Oxygen-Enriched Conditions*. J. Energy Eng. – ASCE, 142(1): 04015017.

KRZYWANSKI J., CZAKIERT T., BLASZCZUK A., RAJCZYK R., MUSKALA W., NOWAK W. 2015b. *A generalized model of SO_2 emissions from large- and small-scale CFB boilers by artificial neural network approach.* Part 1. *The mathematical model of SO_2 emissions in air-firing, oxygen-enriched and oxycombustion CFB conditions*. Fuel Processing Technology, 137: 66–74.

KRZYWANSKI J., CZAKIERT T., BLASZCZUK A., RAJCZYK R., MUSKALA W., NOWAK W. 2015c. *A generalized model of SO_2 emissions from large- and small-scale CFB boilers by artificial neural network approach.* Part 2. *SO_2 emissions from large- and pilot-scale CFB boilers in O_2/N_2, O_2/CO_2 and O_2/RFG combustion atmospheres*. Fuel Processing Technology, 139: 73–85.

LOH W.S. 2010. *Experimental and theoretical studies of waste heat driven pressurized adsorption chillers*. National University of Singapore.

LOH W.S., SAHA B.B., CHAKRABORTY A., NG K.C., CHUN W.G. 2010. *Performance analysis of waste heat driven pressurized adsorption chiller*. Journal of Thermal Science and Technology, 5: 252–265.

LU Z., WANG R., XIA Z. 2013. *Experimental analysis of an adsorption air conditioning with micro-porous silica gel-water*. Applied Thermal Engineering, 50: 1015–1020.

MARLINDA A.S.U., MIYAZAKI T., YUKI U.E.D.A., AKISAWA A. 2010. *Numerical Analysis of double effect adsorption refrigeration cycle using silica-gel/water working pair*. Energies, 9: 1704–1720.

MYAT A., NG K.C., THU K., YOUNG-DEUK K. 2013. *Experimental investigation on the optimal performance of Zeolite-water adsorption chiller*. Applied Energy, 102: 582–590.

OKUNEV B.N., ARISTOV Y.I. 2014. *Making adsorptive chillers faster by a proper choice of adsorption isobar shape: Comparison of optimal and real adsorbents*. Energy, 76: 400–405.

SAHA B.B. 2003. *Performance evaluation of a low-temperature waste heat driven multi-bed adsorption chiller*. International Journal of Multiphase Flow, 29(8): 1249–1263.

SAHA B.B., BOELMAN E.C., KASHIWAGI T. 1995. *Computational analysis of an advanced adsorption-refrigeration cycle*. Energy, 20: 983–294.

SAHA B.B., BOELMAN E., KASHIWAGI T. 1995. *Computer simulation of a silica gel water adsorption refrigeration cycle – the influence of operating conditions on cooling output and COP*. ASHRAE Transactions, 101: 348–357.

SAHA B.B., KOYAMA S., KASHIWAGI T., AKISAWA A., NG, K.C., CHUA H.T. 2003. *Waste heat driven dual-mode, multi-stage, multi-bed regenerative adsorption system*. International Journal of Refrigeration, 26(7): 749–757.

SAPIENZA A., SANTAMARIA S., FRAZZICA A., FRENI A. 2011. *Influence of the management strategy and operating conditions on the performance of an adsorption chiller*. Energy, 36: 5532–5538.

SEKRET R., TURSKI M. 2012. *Research on an adsorption cooling system supplied by solar energy*. Energy and Buildings, 51: 15–20.

STANEK W., GAZDA W. 2014. *Exergo-ecological evaluation of adsorption chiller system*. Energy, 76: 42–48.

SZYC M., NOWAK W. 2014a. *Operation of an adsorption chiller in different cycle time conditions.* Chemical and Process Engineering, 4, 35: 109–119.

SZYC M., NOWAK W. 2014b. *Analysis of cooling cycle in single-stage adsorption chiller.* Polish Journal of Environmental Studies, 23: 1423–1426.

THU K. 2010. *Adsorption desalination: theory & experiments [dissertation].* National University of Singapore.

THU K., YOUNG-DEUK K., MYAT A., CHUN W.G., NG K.C. 2013. *Entropy generation analysis of an adsorption cooling cycle*. International Journal of Heat and Mass Transfer, 60: 143–155.

QIAN S., GLUESENKAMP K., HWANG Y., RADERMACHER R., CHUN H.H. 2013. *Cyclic steady state performance of adsorption chiller with low regeneration temperature zeolite*. Energy, 60: 517–526.

WANG Q., GAO X., XU J.Y., MAIGA A.S., CHEN G.M. 2012. *Experimental investigation on a fluidized-bed adsorber/desorber for the adsorption refrigeration system*. International Journal of Refrigeration, 35: 694–700.

WANG X., HE Z., CHUA H., 2015. *Performance simulation of multi-bed silica gel-water adsorption chillers*. International Journal of Refrigeration, 52: 32–41.

WANG R.Z., XIA Z.Z., WANG L.W., LU Z.S., LI S.L., LI T.X., WU J.Y., HE S. 2011. *Heat transfer design in adsorption refrigeration systems for efficient use of low-grade thermal energy.* Energy, 36: 5425–5439.

WANG D., XIA Z., WU J., WANG R., ZHAI H., DOU W. 2005. *Study of a novel silica gelewater adsorption chiller. Part I. design and performance prediction*. International Journal of Refrigeration, 28: 1073–1083.

WIN K.K., NOWAK W., MATSUDA H., HASATANI M., BIS Z., KRZYWAŃSKI J., GAJEWSKI W. 1995. *Transport Velocity of Coarse Particles in Multi – Solid Fluidized Bed*. Journal of Chemical Engineering of Japan, 28(5): 535–540.

WU D.W., WANG R.Z. 2006. *Combined cooling, heating and power: A review*. Progress in Energy and Combustion Science, 32: 459–495.

YANG W.C. 2003. *Handbook of Fluidization and Fluid-Particle Systems*. Marcel Dekker Inc.

Technical Sciences, 2016, 19(4), 387–399

Quarterly peer-reviewed scientific journal
ISSN 1505-4675
e-ISSN 2083-4527
TECHNICAL SCIENCES
Homepage: www.uwm.edu.pl/techsci/

ENVIRONMENTAL FACTORS INFLUENCE MILLING AND PHYSICAL PROPERTIES AND FLOUR SIZE DISTRIBUTION OF ORGANIC SPELT WHEAT

***Małgorzata Warechowska*[1], *Józef Warechowski*[2], *Krystyna A. Skibniewska*[1], *Ewa Siemianowska*[1], *Józef Tyburski*[3], *Marek A. Aljewicz*[4]**

[1] Chair of Foundations of Safety
[2] Department of Process Engineering and Equipment
[3] Department of Agroecosystems
[4] Department of Dairy Science and Quality Management
University of Warmia and Mazury in Olsztyn, Poland

Received 24 October 2016, accepted 21 November 2016, available online 21 November 2016

K e y w o r d s: organic spelt, physical and mechanical properties, milling, particle size distribution (PSD).

A b s t r a c t

Spelt grain harvested at four organic farms in Poland were assessed for physical and milling properties and flour size distribution. The spelt grain was diversified in relation to the majority of tested milling quality parameters. The environmental conditions had a significant impact on thousand kernel weight, vitreousness, PSI, kernel ash content, specific energy of milling and the particle size distribution of flour. The values of specific energy of milling, coefficient of grinding efficiency, rupture force and rupture energy in the spelt from the organic farms were significantly lower than common wheat. The highest spelt flour yield was obtained of kernels cultivated on ecological farm with semi-coherent and very dry soil was similar to that of common wheat; the milling yield of the spelt originating from other farms was by 9.5% to 12.7% less than from the wheat one. The greatest differences in PSD between the tested flours were detected for the values over 40 μm. The content of this fraction was determined in the range of app. 1% to almost 4.5%; the flour from common wheat contained app. 2.8% of this fraction.

Correspondence: Małgorzata Warechowska, Katedra Podstaw Bezpieczeństwa, Uniwersytet Warmińsko-Mazurski, ul. Jana Heweliusza 10, 10-719 Olsztyn, phone: 89 524 56 13, e-mail: gosiaw@uwm.edu.pl

Introduction

Recently organic agriculture became one of the most rapidly developing branch of agriculture in the world. The reason is growing demand for organic food. Between 2004–2013 acreage of land under organic cultivation in Europe has been increased from 890 000 to 1 845 000 ha (WILLER, SCHAACK 2015). Along the increase of organic cereal acreage the area of spelt cultivation also increases because this kind of cereal is grown mostly in organic farms.

Due to the fact that spelt is cultivated not only in Europe but worldwide, it has become necessary to determine the impact of spelt reaction to environmental factors. WILSON et al. (2008) emphasized that the environmental conditions have an impact on the quality characteristics and technological parameters of grain. Only limited possibility influencing grain quality by fertilization and pesticide application is permissible in organic production, so, besides genetic features, environmental conditions (type of soil, climate) influence the quality of grain. The assessment of the milling quality of grain is important and, in the case of spelt, it has been studied only to a limited extent. Only few studies investigated physical and mechanical properties of spelt wheat (MARKOWSKI et al. 2013, ŚWIECA et al. 2014). Knowledge of mechanical properties and milling grain spelled leads to the optimization of the design process and equipment intended for such purposes, as well as the harvest and distribution of grain. Milling is the basic process in cereal processing. The physical properties of kernels have a significant impact on the effectiveness of milling. The main factors that influence the properties of kernels during milling are hardness and vitreousness (GREFFEUILLE et al. 2007a,b). The hard wheat varieties produce higher yield of flour since the endosperm is more effectively separated from bran (POSNER 2003b). The hardness of kernels significantly influences energy consumption during grinding. The milling of hard wheat is more energy-consuming as opposed to soft wheat (DZIKI et al. 2012). Furthermore, kernel hardness has an impact on the size distribution of middlings and flour. The milling of wheat with soft endosperm produces more small particles than the processing of kernels with hard endosperm (DEVAUX et al. 1998, GREFFEUILLE et al. 2007b). Depending on the degree of grinding of raw material, the course of such processes as mixing, pelleting, dough preparation and baking is different. The quality of final products is also different (PARK et al. 2006). The quality of milling (including flour yield, ash content and flour color) is associated with the morphological parameters of kernels if the milling is performed in comparable conditions (ZHANG et al. 2005). The same varieties of spelt, though they have the same genotype, have to adapt to different regions and therefore react dissimilarly to the environment. Therefore, the cultivation conditions, apart from genetic potential, have an impact on the quality of grain.

The aim of the study was to investigate some physical and milling properties and flour size distribution of organic spelt grain from different environmental conditions of cultivation. Spelt was compared with common wheat. This study may help elucidate some unique characteristics of spelt grain and flour for future uses in the food industry.

Materials and Methods

Samples

The samples of spelt (*Triticum spelta* L.) Schwabenkorn cultivar (SG1 – SG4) originated from a field trial carried out in 2010 on 4 certified organic farms in Poland, differing in the type of soil and its humidity, were assessed. The grain of common wheat Korweta cultivar (CW) from organic farm was the reference (Tab. 1). This common wheat cultivar is known as healthy and well yielding wheat in the ecological cultivation.

The samples of spelt grain, 10 kg each, were hulled in a laboratory device (LD 180 ST 4, WINTERSTEIGER). The moisture content (MC) of spelt and common wheat was determined (ICC Standard Method No. 110/1).

Table 1

Location, certificate number and type of soil organic farms

Samples	Located organic farms	No of certificate	Type of soil
SG1	located at 53°17'N, 19°14'E	AgroBioTest Pl – Eko-07-90013/09	heavy soil with average humidity
SG2	53°01'31.41''N, 17°43'46.56''E	AgroBioTest Pl – Eko-07-05843	semi-coherent soil with average humidity
SG3	53°23'57''N, 19°34'37''E	AgroBioTest Pl – Eko-07-00005	semi-coherent soil and very dry
SG4	53°21'54''N, 19°06'24''E	AgroBioTest Pl – Eko-07-90011/09	very heavy and humid
CW	53°21'54''N, 19°06'24''E	AgroBioTest Pl – Eko-07-90011/09	very heavy and humid

Physical properties

Thousand kernel weight (TKW) was measured for each sample with the use of an electronic kernel counter (Kernel Counter LN S 50A, UNITRA CEMI, Poland) and an electronic scale WPE 120 (Radwag, d = 2 mg, Poland). The kernels were also evaluated for bulk density (BD) (AACC Method 55–31, 2002).

The kernel vitreousness (KV) was evaluated by cross-sections of kernels and expressed as the percentage of vitreous kernels in the sample of 50 elements. The partially vitreous kernels were classified as semi-vitreous kernels and their number in the sample was multiplied by 0.5. The particle size index (PSI) was determined after the AACC Method 55–30: 2002. Total ash content in grain (KAC) and in flour (FAC) were also determined in accordance with ICC Standard Method No. 104/1. The index FA/WA (flour ash/wheat ash) was used to evaluate the differences in the milling of tested spelt grain (POSNER 2009). The kernels of each sample were classified into five fractions based on the thickness: 2.0 – 2.25; 2.25 – 2.5; 2.5 – 2.75; 2.75 – 3.0; 3.0 – 3.5 mm by using the sieves of the following sizes: 2.0, 2.25, 2.5, 2.75, 3.0 and 3.5 mm and by shaking for 5 minutes.

Mechanical tests

Quasi-static compression tests on a single wheat kernel were performed. Thirty kernels were randomly selected from every sample. Each kernel was crushed between parallel plates of Texture Analyzer TA.XT Plus (Stable Micro Systems) with a constant velocity of 0.05 mm $\cdot$ s^{-1} until the distance between plates was fixed at 0.5 mm. The kernel was placed on the lower plate of the testing machine and crushed. For each test load-deformation data was recorded with the computed system. The mechanical behavior of wheat kernels was expressed in terms of deformation, force (F), and energy required to reach the point of total rupture (W) of a single kernel during the quasi-static compression test. The mean value of kernel displacements (l) up to the rupture point for each kernel was calculated.

Test milling

Moisture content of spelt and common wheat was determined and the grain was then re-moisturized to 14.5 ± 0.2% moisture with the addition of distilled water. The restoration of moisture was performed in a tightly-closed container for 48 hours. The samples of grain (100 g) from each farm were weighed on a WLC 2/A1 electronic scale (Radwag, d = 10 mg, Poland) and then milled using Quadrumat Junior mill (Brabender) equipped with a cylinder sifter with a 70GG sieve (PE 236 μm) and flour yield was determined. Six samples of each material were milled.

Milling energy determination

The mill was connected to the power source through the system measuring the consumption of electrical energy. The milling time (t_m) was measured with a stop watch with accuracy of ± 0.1 s. The power of idle running (P_i) of the mill was also determined (the average value of power consumed before the measurements and immediately after the milling of the last sample of each material). The energy necessary for putting the elements of the mill into motion (E_i – energy of idle running) was calculated by multiplying the active power of idle running and the time of milling ($E_i = P_i \cdot t_m$). The work of milling was determined assuming that the total energy consumed (E_c) by the mill equaled the sum of grinding energy and the energy needed for putting the elements of the mill into motion. The specific energy of milling E_m (kJ · kg^{-1}) was calculated with the following formula:

$$E_m = (E_c - E_i) : m \tag{1}$$

where:
m – the weight of grain (kg).

The coefficient of grinding efficiency K_0 (kJ · kg^{-1} flour) was also calculated after GREFFEUILLE et al. (2007b):

$$K_0 = (E_c - E_i) : m_{Fl} \tag{2}$$

where:
m_{Fl} – the mass of the obtained flour (kg).

Particle size analysis

The particle size distribution (PSD) of flour was obtained with Laser Diffraction Analysis (LDA) with Malvern Mastersizer 2000 (version 5.22, Malvern lnstruments Ltd, Malvern, UK). The result of the measurement was expressed as the mean value from six replications. Average size of particles, as a widely used parameter characterizing the granulometric composition, was calculated as the sum of the products of the volumetric part (φ_i) and the average size of each faction (d_i) with the following formula (VELU et al., 2006):

$$d = \text{SUM } (\varphi_i \cdot d_i) \tag{3}$$

Particle sizes $d(0.1)$, $d(0.5)$ and $d(0.9)$ are equivalent to the sieve with mesh sizes correspond to pass of 10%, 50% and 90% (respectively) mass of the material. They were used as indexes of the smallest, average and maximum particle size of flour, respectively.

Statistical analysis of results

Analysis of variance (one-way ANOVA) was performed. The significance of differences between the means was evaluated with Tukey's test. The statistical calculations were performed with STATISTICA® for Windows v. 10 (StatSoft Inc.). The statistical hypotheses were tested at a significance level of $p = 0.05$.

Results and Discussion

Properties of kernels of spelt of Schwabenkorn cultivar are presented in Table 2. No significant difference was calculated for moisture content (MC) determined for spelt and common wheat samples. The values of bulk density (BD) of spelt grain (from 677.1 to 695.6 kg · m^{-3}) from the organic farms were similar, nevertheless, were significantly lower than the BD of common wheat (719.5 kg · m^{-3}).

Table 2

Physical properties of spelt and common wheat grain before milling

Feature	SG1	SG2	SG3	SG4	CW
MC [%]*	11.98 ± 0.23**	11.79 ± 0.25	11.21 ± 0.22	11.56 ± 0.18	11.70 ± 0.22
BD [kg · m^{-3}]	677.1^{a} ± 4.6	684.0^{a} ± 4.2	683.4^{a} ± 2.5	695.6^{b} ± 2.6	719.5^{c} ± 0.5
TKW [g]	36.3^{a} ± 0.6	41.4^{b} ± 0.9	43.9^{c} ± 1.9	43.5^{bc} ± 0.8	36.5^{a} ± 0.7
KAC [%]	2.23^{d} ± 0.03	2.16^{c} ± 0.02	1.98^{a} ± 0.02	2.09^{b} ± 0.01	1.94^{a} ± 0.02
KV [%]	3^{c} ± 1.50	6^{c} ± 1.53	41^{b} ± 5.01	9^{c} ± 3.33	60^{a} ± 5.68
PSI [%]	81.63^{c} ± 7.46	61.08^{b} ± 3.37	53.60^{a} ± 2.14	60.45^{b} ± 1.52	64.75^{b} ± 1.76

* MC – moisture content, BD – bulk density, TKW – thousand kernel weight, KAC – kernel ash content, KV – kernel vitreousness, PSI – particle size index

** The values are expressed as mean ± SD (n=3).

a, b, c, d – values denoted in individual lines with the same letters do not differ significantly for $p \leq 0.05$

The thousand kernel weight (TKW) ranged from 36.6 to 43.9 g and depended on the place of cultivation. Such an influence was also proved in the study of ZHANG et al. (2004). WILSON et al. (2008) determined TKW of spelt grain originating from Ohio in a range of 26 to 41 g, whereas for the same varieties cultivated in Europe MARCONI et al. (1999) reported the range from 49 to 55 g. Environment of plant vegetation play an important role in formation of wheat TKW. Occurrence of soil drought at the time of plant growth depress

shapeliness: endosperm filling extent deceases what is manifested with kernels wrinkling (GAINES et al. 1997). The highest TKW value was determined for SG3 grain; these kernels also yielded the highest milling efficiency. According to POSNER (2003b), larger wheat kernels are correlated with higher flour yield whereas smaller kernels have a larger pericarp-endosperm ratio and therefore less endosperm is available. This correlation was confirmed in our studies.

According to some authors (GREFFEUILLE et al. 2006, MIŚ et al. 2002, TURNBULL, RAHMAN 2002) the genetic potential and environmental conditions have a major impact on the hardness of kernels. The virtuousness and hardness of kernels are important factors which influence the behavior of grain during milling (GREFFEUILLE et al. 2007a,b). The virtuousness (KV) of spelt grain ranged from 3% to 41% and significantly depended on the environment of cultivation in agreement to the previous studies of GREFFEUILLE et al. (2006). The kernels of spelt had lower virtuousness than the common wheat ones (60%). The hardness of tested kernels expressed with the PSI ranged from 53.6% for SG3 to 81.63% for SG1, so, the kernels of spelt and common wheat were classified as "extra soft". MIŚ and GEODECKI (2000) proved that gradual reduction of hardness occurs as a result of repeated moistening of kernels. According to GLENN and JOHNSTON (1994), the kernels with more vitreous endosperm are usually harder. A similar correlation was observed in our studies.

SINGH et al. (2010) proved that grain of wheat grown in different environmental conditions displayed generally diverse chemical composition. This was also confirmed in this study; the kernel ash content (KAC) in spelt was found in the range of 1.98% – 2.23% and depended on the environment of cultivation. Similar to the studies of CACAK-PIETRZAK and GONDEK (2010) and KRAWCZYK et al. (2008), the kernels of spelt had higher KAC than common wheat (1.94%).

Every grain sample was divides into five fractions (Tab. 3). Kernels of thickness 2.50 – 2.75 mm predominated and their content ranged from 44 (CW) to 55% (SG4).

Rapture force (F) and the rupture energy (W) differed significantly among samples from various sites of cultivation. The highest value F and W (58.9 N and 20.8 mJ, respectively) was detected in common wheat and the lowest (26.5 N and 4.7 mJ) was in spelt from SG1 (Tab. 4). The values of rupture force and energy of the spelt Schwabenkorn cv. from the organic farms were significantly lower than common wheat Korweta ones. F and W obtained for Schwabenkorn cv. were similar to values obtained for spelt wheat cv. Ceralio, Holsternkorn and Oberkulmer Rotkorn (MARKOWSKI et al. 2013). Contrary to the most the common European wheat cultivars, spelt kernels characterized by the lower value of rupture force and the rupture energy (DZIKI et al. 2012).

Table 3

Share of fraction grain of spelt and common wheat (thickness of kernel)

Fraction [mm]	d_k [mm]	Share of fraction [%]				
		SG1	SG2	SG3	SG4	CW
2.00 – 2.25	2.125	9	7	8	4	9
2.25 – 2.50	2.375	22	22	23	18	33
2.50 – 2.75	2.625	45	50	53	55	44
2.75 – 3.00	2.875	14	10	7	11	7
3.00 – 3.50	3.125	10	11	9	11	7

d_k – average size of kernel fraction.

Table 4

The mechanical properties of individual fractions of spelt and common wheat

Feature	SG1	SG2	SG3	SG4	CW
l [mm]*	$0.22^{a} \pm 0.04$*	$0.30^{ab} \pm 0.06$	$0.37^{ab} \pm 0.04$	$0.36^{ab} \pm 0.06$	$0.48^{b} \pm 0.06$
F [N]	$26.5^{a} \pm 3.1$	$26.9^{a} \pm 3.4$	$52.2^{b} \pm 6.6$	$39.3^{ab} \pm 5.3$	$58.9^{b} \pm 6.8$
W [mJ]	$4.7^{a} \pm 1.5$	$5.6^{a} \pm 1.5$	$15.3^{ab} \pm 3.3$	$12.5^{ab} \pm 3.9$	$20.8^{b} \pm 4.7$

* l – kernel displacement up to the rupture point, F – rupture force, W – rupture energy
The values are expressed as averages values ± standard deviation ($n = 30$).
a, b – values denoted in individual lines with the same letters do not differ significantly for $p \leq 0.05$

The values of kernel displacements up to the rupture point (l) changed from 0.22 (SG1) to 0.48 mm (CW) and were significantly lower than those reported for common wheat (DZIKI et al. 2012).

The milling efficiency is the main indicator of milling properties of cereal grain. In this study the highest flour yield (FY) was obtained from SG3 (66%), and was comparable with FY for common wheat (Tab. 5). The kernels of spelt from other farms produced statistically significantly lower flour yield (from 55 to 57%). Similarly, ZHANG et al. (2004) proved that flour yield depended in a higher extent on spelt genotype than on cultivation environment. The milling efficiency of all tested spelt samples was low and lower than the values reported for spelt in other studies (ABDEL-AAL et al. 1997, MARCONI et al. 1999, WILSON et al. 2008). Some authors (ABDEL-AAL et al. 1997, CACAK-PIETRZAK, GONDEK 2010, MARCONI et al. 2002) stated that milling of spelt grain produced lower flour yield than of common wheat what indicated poorer milling parameters of spelt than common wheat. The ash content of flour is an important indicator of milling value. Grain with low ash content, in particular in the endosperm, is a desirable raw material for cereal and milling industry. The flour ash content (FAC) in the tested flours ranged from 0.44 (SG3) to 0.57% (CW). The lowest ash content was determined for the flour the spelt grain of the highest flour yield.

Table 5

Milling properties of spelt grain and common wheat

Feature	SG1	SG2	SG3	SG4	CW
FY [%]*	$56.0^{b} \pm 1.5$	$55.0^{b} \pm 1.6$	$66.0^{a} \pm 3.3$	$57.0^{b} \pm 2.1$	$63.0^{a} \pm 1.7$
E_m [kJ · kg^{-1}]	$42.5^{c} \pm 3.5$	$36.6^{ab} \pm 2.5$	$41.6^{bc} \pm 2.7$	$35.5^{a} \pm 3.3$	$55.3^{d} \pm 3.6$
K_0 [kJ · kg^{-1}]	$76.2^{ab} \pm 6.4$	$69.7^{a} \pm 5.8$	$64.1^{a} \pm 5.4$	$62.3^{a} \pm 5.1$	$89.0^{b} \pm 5.2$
FAC [%]	$0.53^{a} \pm 0.02$	$0.50^{ab} \pm 0.04$	$0.44^{b} \pm 0.03$	$0.55^{a} \pm 0.02$	$0.57^{a} \pm 0.04$
FA/WA [–]	0.238^{b}	0.231^{b}	0.222^{a}	0.263^{c}	0.294^{d}

*FY – flour yield, E_m – specific energy of milling, K_0 – coefficient of grinding efficiency, FAC – flour ash content, FA/WA – flour ash/wheat ash.
The values are expressed as averages values ± standard deviation ($n = 6$).
a, b, c, d – values denoted in individual lines with the same letters do not differ significantly for $p \leq 0.05$.

In order to reveal the difference in milliability of the grain, the coefficient FA/WA were determined. The lower value of FA/WA coefficient indicates better milling properties and announces good separation of bran from endosperm (POSNER 1991). In our studies dependence of the environment of spelt cultivation on the milling capacity was proved (Tab. 5). The lowest FA/WA value was detected for the SG3 spelt (0.222); this grain also was classified as a grain with the best milling parameters. The highest milling value was detected for the SG4 grain.

The results of milling energy requirements of spelt grain showed that the specific energy of milling E_m ranged from 35.5 (SG4) to 42.5 kJ kg^{-1} (SG1). Also, for these spelt samples the highest and the lowest values of coefficient of grinding efficiency (K_0) were obtained, i.e. from 62.3 to 76.2 kJ k^{-1}. The analysis of variance of specific energy input for kernel grinding (Er) revealed significant differences between the materials originating from different environments. The milling efficiency coefficient K_0, corresponding to the energy necessary for producing a certain amount of flour, depended to a larger extent on the variety of wheat than on the environment of cultivation. It was found that the grinding of spelt kernels, regardless of the location of growing, required less energy than the grinding of common wheat grain. It resulted mainly from soft texture of spelt wheat grain. Similar observations were reported by ŚWIECA et al. (2014) and WARECHOWSKA et al. (2013). The studies by CACAK-PIETRZAK (2010) indicated that milling of hard and vitreous grain required more the specific energy of milling than the non-vitreous (starchy) grain. In the most extreme cases, the differences in energy consumption of grinding of wheat with hard and soft endosperm reached 100% (PUJOL et al. 2000). According to DZIKI et al. (2012) vitreous kernels are more resistant and require more energy input for grinding, what results from the internal structure of kernel: in vitreous grain, starch granules are deeply seated in the

protein matrix, as opposed to non-vitreous grain which has a loose structure of endosperm (starch granules are separated from each other).

The environmental conditions had a significant impact on the particle size distribution of spelt flours. The resultant flours were composed of many fractions (Fig. 1). Four size fractions were identified in each tested samples of flours. Two fractions were predominant in each product: with modal values app. 25 μm and near 100 μm (with the exception of SG3 sample, which structure was mainly composed of two fractions with modal values app. 30 and 70 μm). In each of the tested wheat, these fractions were smaller than 80 μm resulting in high PSI values. The flours of SG1 and SG2 had the highest content of 25 μm fraction (even greater than that of common wheat flour).

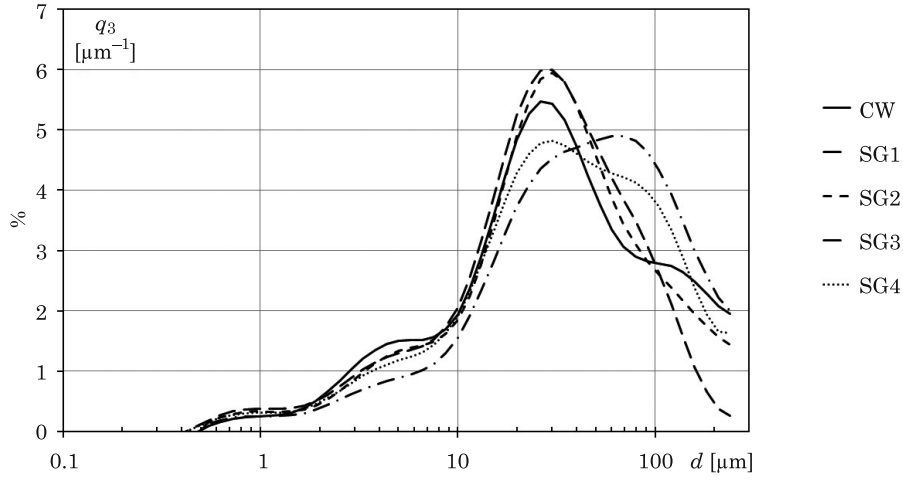

Fig. 1. The particle size distribution of flour

Furthermore, contribution of the largest particles constituting the coarse SG3 and SG4 fraction was greater by approx. 1–2 μm^{-1} than in the case of common wheat. Common wheat had high PSI value (64.75) due to a higher content of 4 μm fraction (higher than any of the tested spelt kernels). An opposite tendency relating to the content of main fractions in comparison with common wheat was observed in the flours obtained from SG4. The content of the 30 μm fraction was smaller by app. 1% and the content of the 80 μm fraction was also significant and higher by app. 1% than in the flour of common wheat. The milling product from SG3 spelt grain, characterized by contribution of 80 μm fraction more approx. 0.5% than 30 μm fraction. Flour obtained from SG4 spelt grain have opposite tendency. It constituted a comparable amount of milling product as the corresponding fraction of common wheat.

The greatest differences between PSD's the tested flours were detected in the section over 40 μm. The lowest content of this fraction was found in SG1 and SG2 material (app. 1% of the total) and the highest was in SG3 and SG4 material (almost 4.5% of the total). The flour from common wheat contained app. 2.8% of the total of this fraction. Similar findings were reported by ABDEL-AAL et al. (1997) who carried out studies on soft spelt.

Specific area of the tested materials assumed the similar values (Tab. 6), excluding SG3. The minimal., median and maximal particle size of flour ($d(0.1)$, $d(0.5)$ and $d(0.9)$ respectively), as well as mean particle size (d) of SG4 and the of common wheat cultivated in the station with comparable soil and climatic conditions assumed the similar values. In the case of SG3 $d(0.1)$ amounted to 7.253 μm, which indicated that this flour contained significantly less fine fractions than other. SG3 assumed the higher values of the traits mentioned above. SG1, SG2 and SG4 assumed the similar values of the parameters of particle size distribution as in the case of common wheat. For all obtained flours fine fraction predominant, $d(0.5)$ was about 60% of the average particle size.

Table 6
The parameters of particle size distribution and specific area of flours of spelt and common wheat

Material	Spec. area [$m^2 \cdot cm^{-3}$]	$d(0.1)$ [μm]	$d(0.5)$ [μm]	$d(0.9)$ [μm]	d [μm]
SG1	0.571	4.666	26.396	86.257	36.000
SG2	0.514	5.082	28.619	112.835	48.363
SG3	0.412	7.253	40.297	137.012	61.929
SG4	0.502	5.353	32.406	123.309	54.088
CW	0.501	4.700	28.055	129.925	51.728

Explanation of the symbols in the paper.

Conclusions

The environmental conditions had a significant impact on thousand kernel weight, vitreousness, PSI, kernel ash content, specific energy of milling and the particle size distribution of flour. The values of specific energy of milling, coefficient of grinding efficiency, rupture force and rupture energy of spelt kernels from the organic farms were significantly lower than of the common wheat ones. The highest spelt flour yield obtained of kernels cultivated on ecological farm with semi-coherent and very dry soil was similar to that of common wheat; the milling yield of the spelt originating from other farms was by 9.5% to 12.7% less than from the wheat one. The greatest differences in PSD

between the tested flours were detected for the values over 40 μm. The content of this fraction was determined in the range of app. 1% to almost 4.5%; the flour from common wheat contained app. 2.8% of this fraction.

References

ABDEL-AAL E.S.M., HUCL P., SOSULSKI F.W., BHIRUD P.R. 1997. *Kernel, milling and backing properties of spring-type spelt and einkorn wheats.* Journal of Cereal Science, 26: 363–370.

Approved methods of the AACC. 2002. American Association of Cereal Chemists. 10th ed. Methods, p. 08–01, 55–30, 55–31.

CACAK-PIETRZAK G., GONDEK E. 2010. *Milling value of spelt wheat and wheat grain.* Acta Agrophysica, 16: 263–273.

DEVAUX M.F., NOVALES B., ABECASSIS J., LE DESCHAULT DE MONREDON F., GUIBERT D. 1998. *Particle size distribution of break, sizing and middling wheat flours by laser diffraction.* Journal of the Science of Food and Agriculture, 78: 237–244.

DZIKI D., CACAK-PIETRZAK G., MIŚ A., JOŃCZYK K., GAWLIK-DZIKI U. 2012. *Influence of wheat kernel physical properties on the pulverizing process.* Journal of Food Science and Technology – Mysore – 51(10). doi: 10.1007/s13197-012-0807-8.

GAINES C.S., FINNEY P.L., ANDREWS L.C. 1997. *Influence of kernel size and shriveling on soft wheat milling and baking quality.* Cereal Chemistry, 74: 700–704.

GLENN G.M., JOHNSTON R.K. 1994. *Water vapor diffusivity in vitreous and mealy wheat endosperm.* Journal of Cereal Science, 20: 275–282.

GREFFEUILLE V., ABECASSIS J., ROUSSET M., OURY F.X., FAYE A., BAR I'HELGOUAC'H C., LULLIEN--PELLERIN V. 2006. *Grain characterization and milling behaviour of near-isogenic lines differing by hardness.* Theoretical and Applied Genetics, 114: 1–12.

GREFFEUILLE V., MABILLE F., ROUSSET M., OURY F.X., ABECASSIS J., LULLIEN-PELLERIN V. 2007a. *Mechanical properties of outer layers from near-isogenic lines of common wheat differing in hardness*. Journal of Cereal Science, 45: 227–235.

GREFFEUILLE V., ABECASSIS J., BAROUH N., VILLENEUVE P., MABILLE F., BAR L'HELGOUAC'H C., LULLIEN-PELLERIN V. 2007b. *Analysis of the milling reduction of bread wheat farina, physical and biochemical characterization.* Journal of Cereal Science, 45: 97–105.

ICC Standard Method No. 104/1, *Determination of ash in cereals and cereal products*.

ICC STANDARD NO. 110/1, *Determination of moisture content of cereals and cereal Products.*

KRAWCZYK P., CEGLINSKA A., KORDIALIK J. 2008. *Comparing the technological value of spelt grains to common wheat grains.* Food. Science. Technology. Quality, 5: 43–51.

MARCONI E., CARCEA M., GRAZIANO M., CUBADDA R. 1999. *Kernel properties and pasta-making quality of five European spelt wheat (Triticum spelta L.) cultivars*. Cereal Chemistry, 76: 25–29.

MARCONI E., CARCEA M., SCHIAVONE M., CUBADDA R. 2002. *Spelt (Triticum spelta L.) pasta quality, Combined effect of flour properties and drying conditions.* Cereal Chemistry, 79: 634–639.

MARKOWSKI M., ŻUK-GOŁASZEWSKA K., KWIATKOWSKI D. 2013. *Influence of variety on selected physical and mechanical properties of wheat.* Industrial Crops and Products, 47: 113–117.

MIŚ A., GEODECKI M. 2000. *Changes in wheat grain hardness during ripening and harvest.* Acta Agrophysica, 37: 119–129.

MIŚ A., GRUNDAS S., KLOCKIEWICZ-KAMIŃSKA E. 2002. *Influence of the nitrogen fertilisation, growing region and wheat cultivar on physical properties of single kernels and their heterogeneity*. Acta Agrophysica, 78: 171–184.

PARK S., CHUNG O.K., SEIB P.A. 2006. *Hard winter wheat and flour properties in relation to breadmaking quality of straight-dough bread, flour particle size and bread crumb grain.* Food Science Technology International, 11: 164–170.

POSNER E.S. 1991. *Wheat and flour ash as a measurement of millability*. Cereal Food World, 36(8): 626–629.

POSNER E.S. 2003a. *Characteristics of milled products*. In: *Encyclopedia of Food Science, Food Technology and Nutrition*. Academic Press, Harcourt Brace Jovanovich Publishers. London, pp. 3997–4005.

POSNER E.S. 2003b. *Principles of milling*. In: *Encyclopedia of Food Science, Food Technology and Nutrition*. Academic Press, Harcourt Brace Jovanovich Publishers. London, pp. 3980–3986.

POSNER E.S. 2009. *The relative technical and economic value of wheat to a mill*. World Grain, 9: 50–54.

PUJOL R., LETANG C., LEMPEREUR A., CHAURAND M., MABILE F., ABECASSIS J. 2000. *Description of a micro-mill with instrumentation handicap measuring grinding characteristics of wheat kernel*. Cereal Chemistry, 77: 421–427.

SINGH S., GUPTA A.K., GUPTA S.K., KAUR N. 2010. *Effect of sowing time on protein quality and starch pasting characteristics in wheat (Triticum aestivum L.) genotypes grown under irrigated and rain-fed conditions*. Food Chemistry, 122: 559–565.

ŚWIECA M., DZIKI D., GAWLIK-DZIKI, U., RÓŻYŁO R., ANDRUSZCZAK S., KRASKA P., KOWALCZYK D., PAŁYS E., BARANIAK B. 2014. *Grinding and nutritional properties of six spelt (Triticum aestivum ssp. spelta L.) cultivars*. Cereal Chemistry, 91: 247–254.

TURNBULL K.M., RAHMAN S. 2002. *Endosperm texture in wheat*. Journal of Cereal Science, 36: 327–337.

VELU V., NAGENDER A., PRABHAKARA RAO P.G., RAO D.G. 2006. *Dry milling characteristic of microwave dried maize grains*. Journal of Food Engineering, 74: 30–36.

WARECHOWSKA M., WARECHOWSKI J., TYBURSKI J. 2013. *A comparison of milling value of spelt wheat and common wheat grain grown in organic farming system*. Polish Journal of Natural Sciences, 28(1): 145–156.

WILLER H., SCHAACK D. 2015. *Organic farming and market development in Europe*. The World of Organic Agriculture. Statistics and Emerging Trends, p. 174–214.

WILSON J.D., BECHTEL D.B., WILSON G.W.T., SEIB P.A. 2008. *Bread quality of spelt wheat and its starch*. Cereal Chemistry, 85: 629–638.

ZHANG Y., HE Z.H., YE G.Y., ZHANG A.M., MAARTEN V.G. 2004. *Effect of environment and genotype on bread-making quality of spring-sown spring wheat cultivars in China*. Euphytica, 139: 75–83.

ZHANG Y., QUAIL K., MUGFORD D.C., ZHONGHU H. 2005. *Milling quality and white salt noodle color of Chinese winter wheat cultivars*. Cereal Chemistry, 82: 633–638.

Technical Sciences, 2016, 19(4), 401–410

Quarterly peer-reviewed scientific journal
ISSN 1505-4675
e-ISSN 2083-4527
TECHNICAL SCIENCES
Homepage: www.uwm.edu.pl/techsci/

THE GENERAL FORMULA FOR CALCULATION OF FUNDAMENTAL FREQUENCY OF AXISYMMETRIC VIBRATIONS OF CIRCULAR PLATES WITH LINEARLY VARIABLE THICKNESS

Jerzy Jaroszewicz[1], *Leszek Radziszewski*[2]

[1] Department of Production Management
Bialystok University of Technology
[2] Departments of Mechanics
Kielce University of Technology

Received 15 October 2016, accepted 13 December 2016, available online 14 December 2016

Key words: circular plates, variable thickness, boundary-value problem, Cauchy's function method, simple estimator of fundamental frequency.

Abstract

This work has derived the general formula, sufficiently precise for engineering calculations of base frequency of axisymmetric free vibrations of uniform, circular diaphragm type plates clamped at the edge with linearly variable thickness. To solve the boundary problem, the Cauchy's function method and characteristic series have been applied. The above formula has been derived on the basis of Dunkerley's formula which is based on the first major term of the characteristic series and results in the simplest, lower bound estimator. The analysis of the formula shows that the base frequency coefficient for diaphragm plates clamped at the edge depends to only a small extent on the Poisson's ratio, and therefore it may be averaged in the case of construction materials. Comparison of the calculations results of the simplest lower bound estimators for the base frequency obtained by using proposed method, with the results known from the literature as precise solutions, including Conway method, confirmed the high accuracy of the proposed method.

Correspondence: Jerzy Jaroszewicz, Katedra Zarządzania Produkcją, Politechnika Białostocka, ul. Ojca Tarasiuka 2, 16-001 Kleosin, e-mail: j.jaroszewicz@pb.edu.pl

Introduction

The direction of research involving more precise approach to the dynamic model entails considerable complexity of the solution. Often, the initial dynamic calculations are successfully accomplished with the use of simple formulas for estimating natural frequency and mode (VASYLENKO, ALEKSIEJCHUK 2004). This work develops a Cauchy's function method and characteristic series to solve boundary problems of vibrations in uniform, circular plates of variable thickness. It is known that only in a few special cases of power and linear variation of thickness a precise solution is applicable, when the equation takes the form of the Euler equation the solutions are in Bessel's function. Thus, Conway H.D in the works of 1958 a) and b) solved cases of change of flexural rigidity by using the formula: $D = D_0\left(\frac{r}{R}\right)^{\frac{m}{3}}$, where D_0, R – constants, r – coordinate, m – coefficient have the following dependences with Poisson's ratio $\nu = \frac{2m-3}{9}$. JAROSZEWICZ and ZORYJ (2005, 2006), with the assistance of co-authors solved that problem for cases of a much larger range of $0 \le m < 6$ and $\nu = \frac{1}{m}$ applying Cauchy's function, characteristic series and Bernstein-Kieropian estimators (JAROSZEWICZ, ZORYJ 2005).

The work by DOMARADZKI, JAROSZEWICZ, ZORYJ (2006) shows that the Poisson's number significantly affects the base frequency parametres only for certain powers m. This work has also demonstrated that for the diaphragm, when $m = 2$ the effect is quite considerable, and so the simplest estimator of the base frequency is as follows: $7.8 \le \chi(\nu) \le 9.3$, the difference relating to the average value is 15.7%. On the other hand, it is also known that in the case of plates of uniform thickness, clamped at the edge ($m = 0$) natural frequency coefficients do not depend on the ν value. Therefore, the examination of influence of and ν on roots of characteristic equation solution for $L[u] = 0$ has a significant consequence in the study of boundary problem of flexural vibrations.

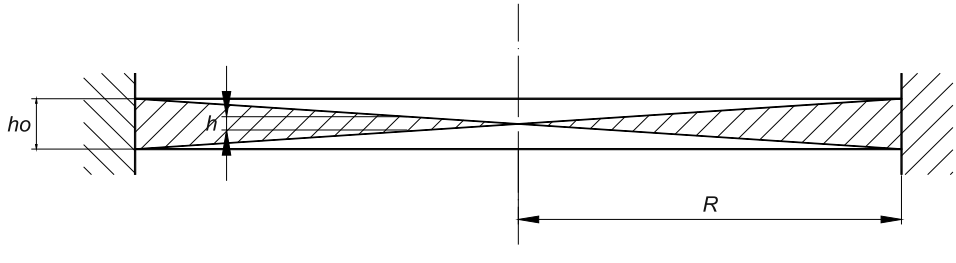

Fig. 1. A model of studied diaphragm

Formulation of the problem

The object of study is a circular plate, rigidly clamped at the edge with radius R, thickness h and flexural rigidity D as definite functions of radial coordinate r (Fig. 1):

$$h = h_0 \cdot \frac{r}{R}, \quad D = D_0\left(\frac{r}{R}\right)^3, \quad D_0 = \frac{Eh_0}{12(1 - \nu^2} \tag{1}$$

In this case $0 < r \leq R$, h_0, D_0 are constants. The following nomenclature was used: – Young's modulus ν – Poisson's ratio.

It should be explained at this point that the tested plate is a thin diaphragm with thickness linearly growing towards the centre of symmetry, where for $r \Rightarrow 0$ this value is close to $(h \to 0)$.

Axisymmmetrical free vibrations of such diaphragm for $m = 3$ are characterized by a following boundary problem (CONWAY 1958a, JAROSZEWICZ, ZORYJ 2005).

$$L_0[u] - pr^{-2m}u = 0, \quad u(R) = 0, \quad u'(R) = 0 \tag{2}$$

where:

$$\mathrm{L}_0[u] \equiv u^{IV} + \frac{8}{r}u^{III} + (11 + 3\nu)\frac{u^{II}}{r^2} + 2(3\nu - 1)\frac{u^I}{r^3}, \; p = \frac{\rho \cdot h}{D} \cdot R^2 \cdot \omega^2 \tag{3}$$

ρh – mass – density of plate, $u = u(r)$ – amplitude of deflection, ω – frequency parameter. Besides of boundary conditions (2) existing requirements concern limiting of deflection and angle of deflection for $r = 0$, which consider limited strength of plate material.

$$|u(0)| < \infty, \quad |u'(0)| < \infty \tag{4}$$

We will further use a no dimensional form $r = \frac{r}{R}$.

Solution of the boundary problem

Linearly independent solutions of equation (5) which correspond to static problem of deflection ($\omega = 0$), and are created by the following four roots (JAROSZEWICZ, ZORYJ 2005, 2006):

$$L[u] = 0 \tag{5}$$

$$\begin{gathered} u_1 = 1, \quad u_2 = r^{\mu_1}, \quad u_3 = r^{\mu_2}, \quad u_4 = r^{-1} \\ \mu_1 = -\frac{1}{2} + \sqrt{\Delta}, \quad \mu_2 = -\frac{1}{2} + \sqrt{\Delta}, \quad \Delta = \frac{1}{4} + q, \quad q = 3(1 - \nu) \end{gathered} \tag{6}$$

The solution of boundary problem (2.2), which is necessary for further consideration, is constructed in the form of the following power series (JAROSZEWICZ, ZORYJ 2005, 2006):

$$S_j = s_{j0} + ps_{j1} + p^2 s_{j2} + ..., j = 1,2 \tag{7}$$

$$s_{jk} = \int_0^r K_0(r,\tau) \cdot \tau^{-2} \cdot s_{j,k-1}(\tau) dt \tag{8}$$

$$s_{10} = 1, \; s_{20} = r^{\mu_1} \tag{9}$$

$K_0(r,\tau)$ – Cauchy's function corresponds to operator $L_0[u]$.

The function $K_0(r,\tau)$, as presented in literature (JAROSZEWICZ, ZORYJ 2005), can be determined by means of a formula:

$$K_0(r,\tau) = \frac{1}{2q\sqrt{\Delta}} (r^{-\mu_1}\tau^{\mu_2+4} - r^{-\mu_2}\tau^{\mu_1+4}) + \frac{1}{q} (r^{-1}\tau^4 - \tau^3) \tag{10}$$

After considering recurrent model of formulas (3.3) the parametre α was introduced in integrals τ^α and S_{j1} ($j = 1,2$) values were calculated on the base of formulas (7, 8, and 9):

$$S_{j1} = \frac{1}{2q\sqrt{\Delta}} \left[(J_1 - J_2) + \frac{1}{q} (J_3 - J_4) \right] \tag{11}$$

$$\begin{gathered} J_1 = r^{\mu_1} \int_0^r \tau^{2+\alpha+\mu_1} d\tau = \frac{r^{2+\alpha}}{3 + \mu_2 + \alpha} \\ J_2 = r^{\mu_2} \int_0^r \tau^{2+\alpha+\mu_1} d\tau = \frac{r^{2+\alpha}}{3 + \mu_1 + \alpha} \end{gathered} \tag{12}$$

$$J_3 = r^{-1}\int_0^r \tau^{2+\alpha} d\tau = \frac{1}{3+\alpha} r^{2+\alpha}, \quad (\alpha \neq -3)$$
$$J_4 = \int_0^r \tau^{(1+\alpha)} d\tau = \frac{1}{3+\alpha} r^{2+\alpha}, \quad (\alpha \neq -2) \tag{12}$$

Flowing limitations ($\alpha \neq -3$) and ($\alpha \neq -2$) result from indeterminacy of expressions (12), received by mean of integration.

Integration (12) is conducted with respect to τ; r denotes variable limit of integration, therefore we receive $K_0(r,\tau)$.

The following formula has been obtained on the base of (11) and with consideration of (12):

$$S_{j1} = \frac{1 \cdot r^{2+\alpha}}{(3\nu + 3 + 5\alpha + \alpha^2)(6 + 5\alpha + \alpha^2)} \tag{13}$$

However, when $j = 1$ it is necessary to assume $\alpha = 0$, because ($s_{10} = u_1 = r^0$), and for $j = 2$ it is $\alpha = \mu_1$, because $s_{20} = u_2 = r^{\mu_1}$ which yields the following:

$$s_{11} = \frac{r^2}{(1+\nu)\cdot 18}, \quad s_{21} = \frac{r^{2+\mu_1}}{(3\nu + A_{21})(3 + A_{21}}, \quad A_{21} = 3 + 5\mu_1 + \mu_1^2 \tag{14}$$

Analogically, when determining s_{12} and s_{22} and also applying (3.8) $\alpha = 2$ and $\alpha = 2 + \mu_1$ and so on, are introduced respectively. As a result the following formulas can be obtained:

$$S_1 = 1 + pr^2 a_{11} + p^2 r^4 a_{12} + ...,$$
$$S_2 = r^{\mu_1} + pr^2 + \mu_{1\alpha_{21}} + p^2 r^4 + \mu_{1\alpha_{22}} + ... \tag{15}$$

And solution limited in measure zero:

$$u = C_1 S_1(r) + C_2 S_2(r) \tag{16}$$

$C_1 S_2$ – arbitrary constants.

In formulas above:

$$a_{11} = (3\nu + 3)^{-1}6^{-1}, \quad a_{21} = [(3\nu + A_{21})(3\nu + A_{21})]^{-1} \tag{17}$$

The characteristic equation and calculation results of simplest estimator of fundamental frequency

Substitution of (13) to boundary conditions (2) resulted in a system of two homogenous algebraic equations in relation to constants C_1 and C_2. By equalling system determinant to zero, the frequency equation, also known as a characteristic equation is derived. The ultimate form of this equation is presented as follows:

$$\begin{vmatrix} S_1 & S_2 \\ S_1' & S_2' \end{vmatrix}_{|r=R} = R^{\mu_1-1}\{\mu_1 + pR^2[\mu_1 a_{11}] - 2a_{11} + (\mu_1 + 2)\, a_{21}\} = 0 \tag{18}$$

$$S_1' = 2pra_{11}, \quad S_2' = \mu_1 r^{\mu_1-1} + (\mu_1 + 2)pr^{\mu_1+1}a_{21}$$

In this way, reduced multiplication R^{μ_1-1} gave an equation which allows calculating the simplest lower estimator of base frequency:

$$\mu_1 - pR^2[(2 - \mu_1)a_{11} - (\mu + 2)a_{21}] = 0 \tag{19}$$

Table 1 summarises forms and calculation results of the simplest estimator of base frequency coefficient for a few selected values of Poisson's number.

Table 1

Derivation of the formula for fundamental frequency of characteristic equation (19)

Material	ν	μ_1	a_1	a_{21}	Equation (17)	γ_A
Glass	0	1.3	0.056	0.0063	$1.3 - 0.0184pR^2 = 0$	8.41
Steel	$^1/_3$	1	0.042	0.0083	$1 - 0.01(6)pR^2 = 0$	7.75
Rubber	$^1/_2$	0.8	0.037	0.0103	$0.8 - 0.0156pR^2 = 0$	7.16

In Table 1 a well known Dunkerley's formula was applied to estimate fundamental frequency:

$$\gamma_A = \frac{1}{\sqrt{a_1}} \tag{20}$$

Where a_1 is the first term of characteristic series (21)

$$1 - a_1\lambda^2 + a_2\lambda^4 - \ldots = 0 \tag{21}$$

Hence values of base frequency (equation 17) with deficiency in respect to appropriate values ν can be determined by applying the following formulas:

$$\mu_1 - pR^2[(2 - \mu_1)a_{11} - (\mu + 2)a_{21}] = 0 \tag{22}$$

On the base of above formulas (22) a general formula for any given values of Poisson's ratio $\nu \in (0;0;5)$ was proposed. Incomplete fundamental frequency of membrane plate clamped at the edge with linearly variable thickness can be calculated by using a simple formula:

$$\omega_1 \approx 2.4 \cdot \frac{h_0}{R^2} \cdot \sqrt{\frac{E}{\rho}} \tag{23}$$

where:

$$\mu_1 = 1, \ (\nu = {}^1/_3)$$

Considering the formulas (16–19) the first approximation (accurate to p, hence to the square of frequency) has been gained, which takes the following form:

$$1 - a_1 pR^a + a_2 p^2 R^{2a} - \ldots = 0 \tag{24}$$

where

$$a_1 = -[A_1(1 - a) + B_1(1 + a)] \tag{25}$$

$$a_2 = [A_1 B_1 A_2(1 - 2a) + B_2(1 + 2a)] \tag{26}$$

Taking into consideration the equation:

$$pR^a = \frac{\rho h_0}{D_0} R^4 \omega^2 \tag{27}$$

Neglecting second terms of series a2 it can be transformed (3.16) to the following form:

$$1 - a_1 \frac{\rho h_0}{D_0} R^4 \omega^2 = 0 \tag{28}$$

Remarks:
For $m = 3$, $\nu = {}^1/_3$ we have obtained $A_1 = (24)^{-1}$, $A_2 = (24 \cdot 360)^{-1}$, $B_1 = (120)^{-1}$, B_2 $(120 \cdot 840)^{-1}$ (JAROSZEWICZ, ZORYJ 2005)

Results of calculations of fundamental natural frequency by mean described in this paper methods

Take into account the series (24) and known Bernstein-Kieropian's estimators with the following form (BERSTEIN, KIEROPIAN 1960) can be applied.

$$(a_1^2 - 2a_2)^{-\frac{1}{4}} < \gamma < \sqrt{2} \cdot (a_1 + \sqrt{a_1^2 - 4a_2})^{-\frac{1}{2}} \tag{29}$$

Coefficients of the series a_1, dependent on can be constructed on the basis of (25). Coefficient $a1$ scrutinized in previous work, where exact formula has been constructed.

$$a_1 = \frac{9^4 \cdot 3 \cdot 10}{[(6 - m) \cdot (6 + m) \cdot (9 + m) \cdot (12 + m)]} \tag{30}$$

Formulas (30), (31) are in accordance with the values quoted in the above remarks.

Obviously first of solution (25) and second derivative of solutions (26) for $a = 0$ $(m = 6)$ are independent of r, in this case coefficients lose sense for $m \to 6$, we have $B_1 \to \infty$, $B_2 \to \infty$, $A_1 \to \infty$ for we have $m \to 4.5$ $(a \to 1)$ and $A_2 \to \infty$ for $m \to 5.25$ $(a \to 0.5)$.

To develop formula (26) for in a similar form formula in following form should be present:

$$a_2 = \frac{3^9 \cdot 5}{2 \cdot (12 + m) \cdot (6 + m) \cdot (18 - m) \cdot (21 - m) \cdot (24 - m) \cdot (6 - m)^2 \cdot (9 + m)^2} \tag{31}$$

Example results of calculation for changed cases $2 < m < 6$ and $\frac{1}{\nu} = m$ obtain on the basis of formulas (21), (29) present on the Table 2, where mean arithmetic value of basic frequency coefficient for $m = 3$, $\nu = {}^1/_3$ is:

$$\gamma_0 = \frac{1}{2}(\gamma_- + \gamma_+) = \frac{1}{2}(8.65.05 + 8.8429) = 8.7467$$

the basic frequency can be found (JAROSZEWICZ et al. 2004)

$$\omega = \gamma \cdot \frac{1}{R^2}\sqrt{\frac{D_0}{\rho h_0}} \equiv \gamma \frac{h_0}{R^2}\sqrt{E[12\rho(1-\nu^2)]^{-1}} \tag{32}$$

Table 2

The fundamental frequency of the plate with nonlinearly variable thickness

No.	Material	ν	Coefficient m	D_0 [Nm]	Masses [kg]	Average of bilateral estimator γ_0	Frequency of the bilateral estimator f[Hz]	Frequency in the FEM analysis f[Hz]	Difference Δ %
1.	titanium	0.36	2.78	9778	6.093	8.697682	322.09 Hz	330.19 Hz	2.45
2.	steel	0.27	3.7	18560	9.834	8.90738	340.23 Hz	347.15 Hz	1.95
3.	zinc	0.25	4.0	10531	8.410	9.356813	286.75 Hz	267.35 Hz	-7.26
4.	concrete	0.17	5.9	1716	1.983	unknown	unknown	211.76 Hz	unknown

Source: JAROSZEWICZ et al. (2008).

It should be noticed that in the case of a constant thickness plate ($m = 0$), the multiplier $\gamma = \gamma_0 = (3.196)^2 = 10.2122$ is independent from ν (VASYLENKO, OLEKSIEJCUK 2004, KOVALENKO 1959). So the ratio of coefficients:

Summary

Deriving of the above mentioned formulas for the Cauchy's functions, as well as fundamental systems of function operator $L_o[u]$ allows to study the convergence problem (velocity of convergence) of solutions of equation (2) in form of power series in respect to parameters of frequencies, depending on values of parameters m and ν.

With the present influence functions of operator $L_o[u]$ corresponding solutions and the use them for any given physically justified values of parameters m and ν ($m \in -\infty, +\infty$); $\nu \in (0;0.5)$) can be consequently determined, when the exact solutions are unknown on the base of general form of Cauchy's function (10). On the basis of quoted solutions, simple engineering formulas for frequencies estimators of circular plates which are characterized by variable parameters distribution can be derived and limits of their application can be identified. The bilateral estimators calculated using four first

elements of the series, allow to credibly observe an influence material constants: Young modulus – E, Poisson ratio – ν density – ρ on the frequencies on axisymmetrical vibrations of circular plates whose thickness or rigidity changes along the radius according to the power function.

Acknowledgement

This work was financially supported by the scientific grant No. W/WZ/1/2015 of Management Faculty of the University of Technology in Bialystok,

This research was partially supported by the grant S/WZ/1/15 of the Polish Ministry of Science and Higher Education.

References

BERNSTEIN S.A., KIEROPIAN K.K. 1960. *Opredelenije častot kolebanij steržnevych system metodom spektralnoi funkcii*. Gosstroiizdat, Moskva, p. 281.

CONWAY H.D. 1958a. *Some special solutions for the flexural vibrations of discs of varying thickness*. Ing. Arch., 26(6): 408–410.

CONWAY H.D. 1958b. *An analogy between the flexural vibrations of a cone and a disc of linearly varying thickness*. Z. Angew. Math. Mech., 37(9–10): 406–407.

DOMORADZKI M., JAROSZEWICZ J., ZORYJ L. 2005. *Anslysis of influence of elastisity constants and material density on base frequency of axi-symmetrical vibrations with variable thickness plates*. Journal of Theoretical and Applied Mechanics, 43(4): 763–775.

JAROSZEWICZ J., MISIUKIEWICZ M., PUCHALSKI W. 2008. *Limitations in application of basic frequency simplest lower estimators in investigation of natural vibrations of circular plates with variable thickness and clamped edges*. Journal of Theoretical and Applied Mechanics, 46(1): 109–212.

JAROSZEWICZ J., ZORYJ L. 2005. *Metody analizy drgań osiowosymetrycznych płyt kołowych z zastosowaniem metody funkcji wpływu Cauche'go*. Rozprawy Naukowe Politechniki Białostockiej, 124: 120.

JAROSZEWICZ J., ZORYJ L. 2006. *The method of partial discretization in free vibration problems of circular plates with variable distribution of parameters*. International Applied Mechanics, 42(3): 364–373.

JAROSZEWICZ J., ZORYJ L., KATUNIN A. 2006. *Influence of additional mass rings on frequencies of axi-symmetrical vibrations of linear variable thickness clamped circular plates*. Journal of Theoretical and Applied Mechanics, 44(4): 867–880.

KOVALENKO A.D. 1959. *Kruglyje plastiny peremenntoj tolshchiny*. Gosudarstvennoje Izdanie Fiziko-Matematicheskoj Literatury, Moskva, p. 294.

HONDKIEWIČ W.S. 1964. *Sobstviennyje kolebanija plastin i obolochek Kiev*. Nukowa Dumka, p. 288.

VASYLENKO N.V. 1992. *Teoriya kolebanij*, Vyshcha Shkola, Kiev, p. 429.

VASYLENKO M.V., ALEKSEJCHUK O.M. 2004. *Teoryja kolyvań i stijkosti ruhu*, Vyshcha Shkola, Kiev, p. 525.

Reviewers of Years – book 2016

Hamid Akbarzadeh
Mehmet Akçay
Vladimir Alvarado
Dariusz Asendrych
Leszek Błaszkiewicz
Michaił Borsuk
Mirosław Bramowicz
Sven Brinkhorst
Tamer Calisir
Soner Çelen
Zekai Celep
Stefan Cenkowski
Martin Chabičovský
Ewa Domian
Paweł Drozda
Jat Du Toit
Paul-Quentin Elias
Nicholas Fantuzzi
Jarosław Fr czek
Vasyl Gafiychuk
Hossein Golbakhshi
Eric Goncalvès Da Silva
Muhamed Hadziabdić
Józef Horabik
Zoran S. Ilić
Ewa Jabłońska-Ryś
Marek Jakubowski
Małgorzata Jasiulewicz
Andrius Jurelionis
Zbigniew Kacprzyk
Agnieszka Kaleta
Apostolos Kantzas
Hakan Kibar
Maroš Korenko
Wolfgang Kresse
Sean Kuo
Kamil Kwiatkowski
Louis Lambruschi
Babak Lashkar-Ara
Katartna Lestyánszka-Škůrková
Algirdas A. Maknickas
Maciej Mikulski
Ubavka B. Mioč
Albina Mościcka
Bartosz Nowak
Matthias Pahn
Krzysztof Pancerz
Velta Parsova
Eimuntas K. Paršeliūnas
Janusz Piechocki
Krzysztof Pokonieczny
Ranena Ponce
Ewa Ropelewska
Kurt Rosentrater
Ramesh P. Sah
Bidyut B. Saha
Paul Salgi
Jürgen Schnell
Riswanti Sigalingging
Wojciech Sobieski
Dinara Sobola
Winston Sweatman
Piotr Srokosz
Zenon Syroka
Tomasz Szolc
Wojciech Tarnowski
Evzen Thöndel
Harry Timmermans
Arris Tijsseling
Francesco Tornabene
Paolo Venturini
Beata Wieczorek
Vidas Žuraulis

Guide for Autors

Introduction

Technical Sciences is a peer-reviewed research Journal published in English by the Publishing House of the University of Warmia and Mazury in Olsztyn (Poland). Journal is published continually since 1998. Until 2010 Journal was published as a yearbook, in 2011 and 2012 it was published semiyearly. From 2013, the Journal is published quarterly in the spring, summer, fall, and winter.

The Journal covers basic and applied researches in the field of engineering and the physical sciences that represent advances in understanding or modeling of the performance of technical and/or biological systems. The Journal covers most branches of engineering science including biosystems engineering, civil engineering, environmental engineering, food engineering, geodesy and cartography, information technology, mechanical engineering, materials science, production engineering etc.

Papers may report the results of experiments, theoretical analyses, design of machines and mechanization systems, processes or processing methods, new materials, new measurements methods or new ideas in information technology.

The submitted manuscripts should have clear science content in methodology, results and discussion. Appropriate scientific and statistically sound experimental designs must be included in methodology and statistics must be employed in analyzing data to discuss the impact of test variables. Moreover there should be clear evidence provided on how the given results advance the area of engineering science. Mere confirmation of existing published data is not acceptable. Manuscripts should present results of completed works.

There are three types of papers: a) research papers (full length articles); b) short communications; c) review papers.

The Journal is published in the printed and electronic version. The electronic version is published on the website ahead of printed version of Technical Sciences.

Technical Sciences does not charge submission or page fees.

Types of paper

The following articles are accepted for publication:

Reviews

Reviews should present a focused aspect on a topic of current interest in the area of biosystems engineering, civil engineering, environmental engineering, food engineering, geodesy and cartography, information technology, mechanical engineering, materials science, production engineering etc. They should include all major findings and bring together reports from a number of sources. These critical reviews should draw out comparisons and conflicts between work, and provide an overview of the 'state of the art'. They should give objective assessments of the topic by citing relevant published work, and not merely present the opinions of individual authors or summarize only work carried out by the authors or by those with whom the authors agree. Undue speculations should also be avoided. Reviews generally should not exceed 6,000 words.

Research Papers

Research Papers are reports of complete, scientifically sound, original research which contributes new knowledge to its field. Papers should not exceed 5,000 words, including figures and tables.

Short Communications

Short Communications are research papers constituting a concise description of a limited investigation. They should be completely documented, both by reference list, and description of the experimental procedures. Short Communications should not occupy more than 2,000 words, including figures and tables.

Letters to the Editor

Letters to the Editor should concern with issues raised by articles recently published in scientific journals or by recent developments in the engineering area.

Contact details for submission

The paper should be sent to the Editorial Office, as a Microsoft Word file, by e-mail: techsci@uwm.edu.pl

Referees

Author/authors should suggest, the names, addresses and e-mail addresses of at least three potential referees. The editor retains the sole right to decide whether or not the suggested reviewers are used.

Submission declaration

After final acceptance of the manuscript, the corresponding author should send to the Editorial Office the author's declaration. Submission of an article implies that the work has not been published previously (except in the form of an abstract or as part of a published lecture or academic thesis or as an electronic preprint), that it is not under consideration for publication elsewhere, that publication is approved by all authors and tacitly or explicitly by the responsible authorities where the work was carried out, and that, if accepted, it will not be published elsewhere in the same form, in English or in any other language.

To prevent cases of ghostwriting and guest authorship, the author/authors of manuscripts is/are obliged to: (i) disclose the input of each author to the text (specifying their affiliations and contributions, i.e. who is the author of the concept, assumptions, methods, protocol, etc. used during the preparation of the text); (ii) disclose information about the funding sources for the article, the contribution of research institutions, associations and other entities.

Language

Authors should prepare the full manuscript i.e. title, abstract and the main text in English (American or British usage is accepted). Polish version of the manuscript is not required.

The file type

Text should be prepared in a word processor and saved in doc or docx file (MS Office).

Article structure

Suggested structure of the manuscript is as follows:

Title
Authors and affiliations
Corresponding author
Abstract
Keywords
Introduction
Material and Methods
Results and Discussion
Conclusions

Acknowledgements (*optional*)
References
Tables
Figures

Subdivision – numbered sections

Text should be organized into clearly defined and numbered sections and subsections (optionally). Sections and subsections should be numbered as 1. 2. 3. then 1.1 1.2 1.3 (then 1.1.1, 1.1.2, ...). The abstract should not be included in numbering section. A brief heading may be given to any subsection. Each heading should appear on its own separate line. A single line should separate paragraphs. Indentation should be used in each paragraph.

Font guidelines are as follows:
- Title: 14 pt. Times New Roman, bold, centered, with caps
- Author names and affiliations:12 pt. Times New Roman, bold, centered, italic, two blank line above
- Abstract: 10 pt. Times New Roman, full justified, one and a half space. Abstract should begin with the word Abstract immediately following the title block with one blank line in between. The word Abstract: 10 pt. Times New Roman, centered, indentation should be used
- Section Headings: Not numbered, 12 pt. Times New Roman, bold, centered; one blank line above
- Section Sub-headings: Numbered, 12 pt. Times New Roman, bold, italic, centered; one blank line above
- Regular text: 12 pt. Times New Roman, one and a half space,full justified, indentation should be used in each paragraph

Title page information

The following information should be placed at the first page:

Title

Concise and informative. If possible, authors should not use abbreviations and formulae.

Authors and affiliations

Author/authors' names should be presented below the title. The authors' affiliation addresses (department or college; university or company; city, state and zip code, country) should be placed below the names. Authors with the same affiliation must be grouped together on the same line with affiliation information following in a single block. Authors should indicate all affiliations with a lower-case superscript letter immediately after the author's name and in front of the appropriate address.

Corresponding author

It should be clearly indicated who will handle correspondence at all stages of refereeing and publication, also post-publication process. The e-mail address should be provided (footer, first page). Contact details must be kept up to date by the corresponding author.

Abstract

The abstract should have up to 100-150 words in length. A concise abstract is required. The abstract should state briefly the aim of the research, the principal results and major conclusions. Abstract must be able to stand alone. Only abbreviations firmly

established in the field may be eligible. Non-standard or uncommon abbreviations should be avoided, but if essential they must be defined at their first mention in the abstract itself.

Keywords

Immediately after the abstract, author/authors should provide a maximum of 6 keywords avoiding general, plural terms and multiple concepts (avoid, for example, 'and', 'of'). Author/authors should be sparing with abbreviations: only abbreviations firmly established in the field may be eligible.

Abbreviations

Author/authors should define abbreviations that are not standard in this field. Abbreviations must be defined at their first mention there. Author/authors should ensure consistency of abbreviations throughout the article.

Units

All units used in the paper should be consistent with the SI system of measurement. If other units are mentioned, author/authors should give their equivalent in SI.

Introduction

Literature sources should be appropriately selected and cited. A literature review should discuss published information in a particular subject area. Introduction should identify, describe and analyze related research that has already been done and summarize the state of art in the topic area. Author/authors should state clearly the objectives of the work and provide an adequate background.

Material and Methods

Author/authors should provide sufficient details to allow the work to be reproduced by other researchers. Methods already published should be indicated by a reference. A theory should extend, not repeat, the background to the article already dealt within the Introduction and lay the foundation for further work. Calculations should represent a practical development from a theoretical basis.

Results and Discussion

Results should be clear and concise. Discussion should explore the significance of the results of the work, not repeat them. A combined Results and Discussion section is often appropriate.

Conclusions

The main conclusions of the study may be presented in a Conclusions section, which may stand alone or form a subsection of a Results and Discussion section.

Acknowledgements

Author/authors should include acknowledgements in a separate section at the end of the manuscript before the references. Author/authors should not include them on the title page, as a footnote to the title or otherwise. Individuals who provided help during the research study should be listed in this section.

Artwork
General points

– Make sure you use uniform lettering and sizing of your original artwork
– Embed the used fonts if the application provides that option

– Aim to use the following fonts in your illustrations: Arial, Courier, Times New Roman, Symbol
– Number equations, tables and figures according to their sequence in the text
– Size the illustrations close to the desired dimensions of the printed version

Formats

If your electronic artwork is created in a Microsoft Office application (Word, PowerPoint, Excel) then please supply 'as is' in the native document format

Regardless of the application used other than Microsoft Office, when your electronic artwork is finalized, please 'Save as' or convert the images to one of the following formats (note the resolution requirements given below):

EPS (or PDF): Vector drawings, embed all used fonts

JPEG: Color or grayscale photographs (halftones), keep to a minimum of 300 dpi

JPEG: Bitmapped (pure black & white pixels) line drawings, keep to a minimum of 1000 dpi or combinations bitmapped line/half-tone (color or grayscale), keep to a minimum of 500 dpi

Please **do not**:
– Supply files that are optimized for screen use (e.g., GIF, BMP, PICT, WPG); these typically have a low number of pixels and limited set of colors
– Supply files that are too low in resolution
– Submit graphics that are disproportionately large for the content

Color artwork

Author/authors should make sure that artwork files are in an acceptable format (JPEG, EPS PDF, or MS Office files) and with the correct resolution. If, together with manuscript, author/authors submit color figures then Technical Sciences will ensure that these figures will appear in color on the web as well as in the printed version at no additional charge.

Tables, figures, and equations

Tables, figures, and equations/formulae should be identified and numbered consecutively in accordance with their appearance in the text.

Equations/mathematical and physical formulae should be presented in the main text, while tables and figures should be presented at the end of file (after References section). Mathematical and physical formulae should be presented in the MS Word formula editor.

All types of figures can be black/white or color. Author/authors should ensure that each figure is numbered and has a caption. A caption should be placed below the figure. Figure must be able to stand alone (explanation of all symbols and abbreviations used in figure is required). Units must be always included. It is noted that figure and table numbering should be independent.

Tables should be numbered consecutively in accordance with their appearance in the text. Table caption should be placed above the table. Footnotes to tables should be placed below the table body and indicated with superscript lowercase letters. Vertical rules should be avoided. Author/authors should ensure that the data presented in tables do not duplicate results described in figures, diagrams, schemes, etc. Table must be able to stand alone (explanation of all symbols and abbreviations used in table is required). Units must be always included. As above, figure and table numbering should be independent.

References

References: All publications cited in the text should be presented in a list of references following the text of the manuscript. The manuscript should be carefully checked to ensure that the spelling of authors' names and dates of publications are exactly the same in the text as in the reference list. Authors should ensure that each reference cited in the text is also present in the reference list (and vice versa).

Citations may be made directly (or parenthetically). All citations in the text should refer to:

1. Single author

The author's name (without initials, with caps, unless there is ambiguity) and the year of publication should appear in the text

2. Two authors

Both authors' names (without initials, with caps) and the year of publication should appear in the text

3. Three or more authors

First author's name followed by et al. and the year of publication should appear in the text

Groups of references should be listed first alphabetically, then chronologically.

Examples:

"... have been reported recently (ALLAN, 1996a, 1996b, 1999; ALLAN and JONES, 1995). KRAMER et al. (2000) have recently shown..."

The list of references should be arranged alphabetically by authors' names, then further sorted chronologically if necessary. More than once reference from the same author(s) in the same year must be identified by the letters "a", "b", "c" etc., placed after the year of publication.

References should be given in the following form:

KUMBHAR B.K., AGARVAL R.S., DAS K. 1981. *Thermal properties of fresh and frozen fish*. International Journal of Refrigeration, 4(3), 143–146.

MACHADO M.F., OLIVEIRA F.A.R., GEKAS V. 1997. *Modelling water uptake and soluble solids losses by puffed breakfast cereal immersed in water or milk*. In Proceedings of the Seventh International Congress on Engineering and Food, Brighton, UK.

NETER J., KUTNER M.H., NACHTSCHEIM C.J., WASSERMAN W. 1966. *Applied linear statistical models* (4th ed., pp. 1289–1293). Irwin, Chicago.

THOMSON F.M. 1984. *Storage of particulate solids*. In M. E. Fayed, L. Otten (Eds.), Handbook of Powder Science and Technology (pp. 365–463). Van Nostrand Reinhold, New York.

Citation of a reference as 'in press' implies that the item has been accepted for publication.

Note that the full names of Journals should appear in reference list.

Submission checklist

The following list will be useful during the final checking of an article prior to the submission. Before sending the manuscript to the Journal for review, author/authors should ensure that the following items are present:

– Text is prepared with a word processor and saved in DOC or DOCX file (MS Office). One author has been designated as the corresponding author with contact details: e-mail address

– Manuscript has been 'spell-checked' and 'grammar-checked'

– References are in the correct format for this Journal

– All references mentioned in the Reference list are cited in the text, and vice versa

– Author/authors does/do not supply files that are too low in resolution

– Author/authors does/do not submit graphics that are disproportionately large for the content